THE UNIVERSITY OF WEST BOHEMIA
FACULTY OF APPLIED SCIENCES

and

THE UNIVERSITY OF SYDNEY
FACULTY OF SCIENCE
SCHOOL OF PHYSICS

Ph.D. Thesis

PLZEŇ, 2006 Ing. Jiří Houška

THE UNIVERSITY OF WEST BOHEMIA
FACULTY OF APPLIED SCIENCES

and

THE UNIVERSITY OF SYDNEY
FACULTY OF SCIENCE
SCHOOL OF PHYSICS

A thesis submitted for the degree of
Doctor of Philosophy
in the field of

Plasma physics and physics of thin films

Ing. (M.Sc.) Jiří Houška

New quaternary amorphous materials Si-B-C-N: reactive magnetron sputtering and an ab-initio study

Supervisors: Prof. RNDr. Jaroslav Vlček, CSc. (UWB)
Prof. Marcela M.M. Bilek (USYD)
Date of rigorous exam: 23rd June 2005
Date of submitting: 4th July 2006

In Plzeň, 2006

I submit for examining and defending a thesis written at the Faculty of Applied Sciences, University of West Bohemia (Czech Republic) and at The School of Physics, Faculty of Science, University of Sydney (Australia).

I wish to thank here both my supervisors, Prof. Jaroslav Vlček and Prof. Marcela Bilek, and Prof. David McKenzie, for their great help during my Ph.D. studies and with writing the thesis.

Measurements of elemental composition of deposited materials were performed by Vratislav Peřina, and measurements of their bonding structure were performed by Jiří Čížek. For advice with and collaboration on depositions of Si-B-C-N materials, I also thank especially Štěpán Potocký, Jiří Kalaš, Stanislav Hřeben, Jiří Čapek and Petr Zeman. Because chapter 3 of the thesis is based on results shared with other Ph.D. students, only part of all collectively obtained results is included there.

For advice with and collaboration on computer simulations of structures of deposited materials, I thank especially Oliver Warschkow and Nicholas Cooper.

To the best of my knowledge, this thesis contains no copy or paraphrase of work published by any other person, except where duly acknowledged in the text.

The work was done in the course of projects of the Ministry of Education of Czech Republic MSM 235200002 and MSM 4977751302, and with use of computational resources provided by Australian Partnership for Advanced Computing (APAC), the Australian Center for Advanced Computing and Communications (AC3) and the Metacentrum Czech Republic.

Finally I would like to thank my family, which supported me essentially during all my studies.

In Plzeň, 4th July 2006 Ing. Jiří Houška

Table of contents

Table of contents

1 Introduction

Si-B-C-N materials are currently attracting a great deal of international interest due to their high hardness and exceptional thermal stability. This combination of properties indicates that these materials may have great potential in applications such as coatings technologies, microelectronics or production of thermally stable fibres for composites. This thesis describes experimental preparation of new hard and highly thermally stable amorphous Si-B-C-N materials, and computer simulations of their structures to aid in the understanding of physical mechanisms governing their synthesis and properties. This chapter includes motivation of the research (description of predecessors of these materials), status of knowledge concerning both experimental preparation of Si-B-C-N materials and the computer simulations, and list of particular aims of the thesis.

1.1 Hard amorphous materials

In 1980's started a boom concerning high-performance advanced ceramics and their mechanical, thermal and electrical applications[1]. Various properties of these new hard materials have been studied by both experimental and theoretical methods. In bulk form they can for example potentially serve as structural parts of automotive engines or turbines up to very high temperatures. In the form of thin films they can for example maximize hardness of the surface or optimize its wear resistance without sacrificing properties (such as toughness) of the bulk material.

The β-C_3N_4 material (with structure derived from β-Si_3N_4) was predicted to have hardness comparable or even higher than diamond[2]. Although all attempts to synthesize the superhard crystalline β-C_3N_4 phase have thus far been unsuccessful, but have resulted in several different kinds of carbon nitride (CN_x) compounds. In spite of the fact that most of the CN_x films prepared by various techniques (see, for example, references 3-6) are amorphous and substoichiometric in nitrogen, these layers can possess interesting and potentially very useful mechanical properties, such as high hardness, very large elastic recovery, good adhesion to substrates and low friction coefficient and wear.

Later, the ternary Si-C-N materials attracted great interest due to their new features compared to those of crystalline Si_3N_4 and SiC mixtures and their potential applications in microelectronics and coating technologies. Various deposition techniques were used to prepare crystalline, amorphous or nanostructured Si-C-N compounds (see, for example, references 7-10). These materials can possess a useful combination of properties, such as high hardness, wide band gap characteristics, a wide optical transparency window, promising field emission characteristics, high-temperature oxidation resistance, chemical inertness and promising wetting behavior.

Recently, it has been reported that addition of proper amount of boron into Si-C-N system leads to a new unique class of Si-B-C-N ceramics, combining an exceptional high-temperature behaviour (oxidation resistance, creep resistance, stability of mechanical properties, etc.) with same or even better other material characteristics than possess binary and ternary materials from the respective subsystems. List of all achievements in this field, together with all references available, is provided in the following separate section 1.2.1.

1.2 Status of knowledge

1.2.1 Experimental preparation of Si-B-C-N materials

Si-B-C-N materials can possess very high hardness due to the formation of a high volume density of short covalent bonds. Moreover, proper amount of boron decreases activity of carbon integrated in B-C-N zones in comparison with "free carbon" and thus dramatically increases their thermal stability in comparison with the Si-C-N materials[11,12]. This is due to the increase of temperatures when start the decomposition reactions $Si_3N_4 + 3C \rightarrow 3SiC + 2N_2$ and $Si_3N_4 \rightarrow 3Si + 2N_2$ (under 1 atmosphere of N_2: 1481 and 1840 °C, respectively) to higher values. Unique combination of these features with the other properties reported previously for binary and ternary materials from this system lead to many potential applications in areas such as:

- coating technologies[13,14].
- microelectronics[14,15.]
- production of thermally stable fibres for composites[16].

In recent years, materials have been already reported that feature at various elemental compositions one or more of:

- very high thermal stability and oxidation resistance[11-13,16-26].
- creep resistance at elevated temperatures[22,27,28].
- low stress[29].
- low thermal expansion coefficient[19,23].
- low thermal conductivity[23].
- homogeneity leading to a smooth surface[14,16,18,22].
- promising electrical properties (significantly lower resistivity than the Si-C-N ceramics)[15].
- transparency and good adherence to substrates.

Most of recently published works on Si-B-C-N materials deal with preparation of Si-B-C-N ceramics by precursor pyrolysis[11,12,15-21,23-28,30-38]. Despite the number of valuable results obtained, this method has disadvantages including degradation of properties due to the large content of hydrogen from the precursors in materials and high process temperatures, let alone industrial applications of materials produced in the form of small porous grains[21]. Fewer works deal with preparation of Si-B-C-N materials in the form of thin films by CVD[13,14,29]. Also this method uses the hydrogen-containing precursors.

To our knowledge, up to now, no effort has been made to form Si–B–C–N films using magnetron sputtering (or any other PVD method), which allows film generation at noticeably reduced substrate temperatures and without hydrogen-containing precursors resulting in an enlarged residual content of hydrogen in films. The only exceptions are our recent papers[39-41]. Some of these results (including results on thermal stability and oxidation resistance) were also included in recent PhD theses – Refs. 42 and 43. Other part of results published in these papers form basis of chapters 3 and 4 of this thesis. In the following list are included all characteristics of our Si-B-C-N materials prepared by reactive magnetron sputtering in the form of thin films. The films were found to have the following main characteristics :

- density around 2.4 g/cm^3.
- amorphicity (HRTEM, SAED).
- optical transparency for some compositions (ellipsometry).
- exclusive bonding of B and preferable bonding of Si and C to N (XPS, IR VASE).
- extremely high oxidation resistance in air, for some compositions up to a 1350 °C substrate limit (TGA).
- hardness up to 47 GPa, modified Young modulus between 170 and 270 GPa and elastic recovery around 75 % (nanoindentation).
- good adhesion to substrates at compressive stress lower than 1.8 GPa (profilometry).
- friction coefficients around 0.4 (tribometry).
- electrical conductivity for some compositions comparable with semiconductors (four points method).

1.2.2 Ab-initio simulations of amorphous materials

In connection with increased computing possibilities in last years, the molecular-dynamics (MD) simulations became a well established tool, which can support an experiment by providing information not accessible experimentally. Many different levels of theory can be used to describe the interatomic interactions, ranging from density-functional theory (DFT), through the tight-binding approaches, to empirical potential methods. An overview of them together with comparison of their results with experiment can be found in Ref. 44.

Because internal network structure and material properties of amorphous solids are intensively dependent on the formation conditions (the cooling rate of the liquid quench and the ordering processes that occur while the material solidifies from the melt), meaningful computer simulations of this type of material must focus on the formation process. In our simulation work, we try to capture this formation process using a *liquid quench* algorithm. This technique attempts to capture the formation conditions of the real materials, which arise from rapid cooling of the localized melt (*thermal spike)* created around sites of energetic ion impact. This method has been successfully applied to various amorphous materials including carbon[45-47], H:C[48], C doped by N[49], (B)(Al)N[50] or H:SiC[51].

Informations accessible in principle using the ab-initio methods (particularly the Car-Parrinello implementation of density functional theory) include:

- structural data such as bond statistics, bond lengths, bond orders, atomic coordinations, roles of various types of atoms or segregation in materials.
- calculations of various temperature-dependent characteristics. The ability to "see" the atomic motion can contribute greatly to the understanding of the mechanisms of many dynamical phenomena.
- values of various physical (and chemical) properties. Because it is only the adiabatic motion of the ground state that is calculated directly, information on electronically excited states (and hence on properties such as the conductivity) can only be obtained after further calculations. The ground-state electron density resulting from DFT MD calculations may be an useful input for them[52]. The calculable properties include
  - density of states, band structure and charge densities,
  - elastic constants and ideal strength,
  - optical conductivity,
  - magnetic properties,
  - vibrational (infrared) frequencies,

– or neutron-diffraction data.

1.3 Aims of the thesis

Our research was originally started as a purely experimental work in the field of preparation and characterization of materials from the Si-B-C-N system by magnetron sputtering (see the aims in the following section 1.3.1). Due to a number of complex relations between experimental conditions, elemental composition and structure and properties of these quaternary materials, a combined approach of experiment and computer simulations has been later used to find and explain them. This necessarily led to further aims listed in the section 1.3.2.

1.3.1 Aims of the experimental part

First part of the thesis is focused on experimental preparation of new hard quaternary amorphous materials Si-B-C-N in the form of thin films. To our knowledge, up to now, no effort has been made to form Si–B–C–N films using magnetron sputtering except our recent papers[39-41]. This technique allows film generation at noticeably reduced substrate temperatures and without hydrogen-containing precursors resulting in an enlarged residual content of hydrogen in films. Let us recall that the magnetron sputtering is one of the most versatile techniques compatible with semiconductor technologies and that its further important advantage is an easy up-scaling. Specific aims of this part of the thesis were to:

(1) master preparation of Si-B-C-N thin films using magnetron sputtering of composite C-Si-B and B_4C-Si targets in N_2 + Ar gas mixtures on rf-biased substrates at low substrate temperatures, and measurements of their mechanical properties (hardness, compressive stress, effective Young's modulus, elastic recovery) and electrical conductivity.
(2) deposit a series of samples by changing sputtered target composition and gas mixture composition, and to show and explain relationships of process parameters, elemental composition, bonding structure and properties of deposited Si-B-C-N films.
(3) show and explain the effect of rf-induced negative substrate bias voltage on the film characteristics (elemental composition, bonding structure, mechanical and electrical properties) for several most promising sputtered target compositions and gas mixture compositions identified.
(4) calculate deposition characteristics (such as a ratio of fluxes of ions and film-forming particles bombarding the growing films, and an energy delivered into deposited films per one film atom), and to use them for explaining the effect of substrate bias voltage.

1.3.2 Aims of the theoretical part

Second part of the thesis is focused on ab-initio simulations of structures of experimentally prepared Si-B-C-N materials (with small content of implanted Ar). In the performed *liquid-quench* simulations, the Kohn-Sham equations for the valence electrons are expanded in a basis of plane wave functions, while core electrons were represented using Goedecker-type pseudopotentials. We simplified the ion bombardment process by assuming that the primary impact creates a localized region of high temperature, commonly referred to as a *thermal spike*. Thermal spikes have a cooling time sufficiently short to be simulated using ab initio molecular dynamics (MD) methods. Specific aims of this part of the thesis were to:

(1) master running of MD simulations using the Car-Parrinello Molecular Dynamics (CPMD) code, and the liquid-quench algorithm which attempts to capture the formation conditions of the real materials arising from rapid cooling of the localized melt (thermal spike) created around sites of energetic ion impact.

(2) perform series of liquid-quench simulations of nitrogen-containing amorphous (Si)-(B)-C-N materials in order to examine formation of N_2 molecules during these simulations, in order to show dependence of this effect on temperature, material density and cooling time of the thermal spike, and to propose an simulation algorithm which accounts for N_2 formation and diffusion out of the structure and still yields a material of desired N-content.

(3) investigate how the presence of Ar atoms in the sample affects the liquid quench and the final structure of the Si-B-C-N materials, and to use the simulation results for explaining related experimental results on deposited samples containing implanted Ar atoms.

(4) calculate various data affecting material properties (such as bonding statistics or electonic structure), to compare them for previously deposited materials of different Si-B-C-N compositions in order to show resources and limits of the simulation method used, and to use the simulation results for explaining related experimental results on deposited samples.

1.4 References

[1] R. Riedel (ed.), Handbook of ceramic hard materials (Wiley Europe, 2000).

[2] A.Y.Liu and M.L. Cohen, Science **245**, 841 (1989).

[3] D. Marton, K.J. Boyd and J.W. Radalais, Int. J. Mod. Phys. B **9**, 3527 (1995).

[4] S. Vepřek, J. Weidmann and F. Glatz, J. Vac. Sci Technol. A **13**, 2914 (1995).

[5] R. Kaltofeln, T. Sebald and G. Weise, Thin Solid Films **290/291**, 112 (1996).

[6] J. Vlček, K. Rusňák, V. Hájek and L. Martinů, J. Appl. Phys. **86**, 3646 (1999).

[7] H. Lutz, M. Bruns, F. Link and H. Baumann, Thin Solid Films **332**, 230 (1998).

[8] A. Badzian, T. Badzian, T. Roy and W. Drawl, Thin Solid Films **354**, 148 (1999).

[9] T. Berlind, N. Hellgren, M. P. Johansson and L. Hultman, Surf. Coat. Technol. **141**, 145 (2001).

[10] J. Vlček, M. Kormunda, J. Čížek, V. Peřina and J. Zemek, Diamond Relat. Mater. **12**, 1287 (2003).

[11] A. Müller, P. Gerstel, M. Weinman, J. Bill and F. Aldinger, J. Eur. Ceram. Soc. **20**, 2655 (2000).

[12] A. Müller, P. Gerstel, M. Weinman, J. Bill and F. Aldinger, J. Eur. Ceram. Soc. **21**, 2171 (2001).

[13] M.A. Rooke and P.M.A. Sherwood, Chem. Mater. **9**, 285 (1997).

[14] D.Hegemann, R. Riedel and C. Oehr, Chem. Vap. Deposition **5**, 61 (1999).

[15] P.A. Ramakrishnan, Y.T. Wang, D. Balzar, L. An, C. Haluschka, R. Riedel and A.M. Hermann, Appl. Phys. Lett. **78**, 3076 (2001).

[16] L.Lu, Y.C. Song and C.X. Feng, J. Mater. Sci. Lett. 17, 599 (1998).

[17] H. Jungermann and M. Jansen, Mat. Res. Innovat 2, **200** (1999).

[18] R. Riedel, A. Kienzle, W. Dressler, L. Ruwisch, J. Bill and F. Aldinger, Nature **386**, 796 (1996).

[19] S.Schmidt, G. Borchardt, S. Weber, H. Scherrer, H. Baumann, A. Müller and J. Bill, J. Non-Cryst. Sol. **298**, 232 (2002).

[20] A. Müller, A. Zern, P. Gerstel, J. Bill and F. Aldinger, J. Eur. Ceram. Soc. **22**, 1631 (2002).

[21] E. Butchereit, K.G. Nickel and A. Müller, J. Am. Ceram. Soc. **84**, 2184 (2001).
[22] B. Baufeld, H. Gu, J. Bill, F. Wakai and F. Aldinger, J. Eur. Ceram. Soc. **19**, 2797 (1999).
[23] H.P. Baldus and M. Jansen, Angew. Chem. Int. Ed. Engl. **36**, 328 (1997).
[24] M. Weinmann, J. Schuhmacher, H. Kummer, S. Prinz, H. Peng, H.J. Seifert, M. Christ, K. Müler, J. Bill and F. Aldinger, Chem. Mater. **12**, 623 (2000).
[25] J. Bill, T.W. Kamphowe, A. Müller, T. Wichmann, A. Zern, A. Jalowiecki, J. Mayer, M. Weinmann, J. Schuhmacher, K. Müler, J. Peng, H.J. Seifert and F. Aldinger, Appl. Organomet. Chem. **15**, 777 (2001).
[26] P. Gerstel, A. Müler, J. Bill and F. Aldinger, Chem. Mater. **15**, 4980 (2003).
[27] R. Riedel, L.M. Ruswisch, L. An, R. Raj, J. Am. Ceram. Soc. **81**, 3341 (1998).
[28] N.V. Ravi Kumar, R. Mager, Y. Cai, A. Zimmermann and F. Aldinger, Scripta Materalia **51**, 65 (2004).
[29] D. Hegemann, C. Oehr and R. Riedel, 14th Internat. Symp. Plasma Chemistry, Symp. Proceedings (Ed.: M. Hrabovsky, M. Konrad, V. Kopecky), Vol. III, Prague (Czech Republic), 1999, p. 1573.
[30] Y.Cai, A. Zimmerman, S. Prinz, A. Zern, F. Phillipp and F. Aldinger, Scripta Materialia **45**, 1301 (2001).
[31] A. Zimmerman, A. Bauer, M. Christ, Y. Cai and F. Aldinger, Acta Materialia **50**, 1187 (2002).
[32] A. Jalowiecki, J. Bill, F. Aldinger and J. Mayer, Composites **27A**, 717 (1996).
[33] N. Janakiraman, M. Weinmann, J. Schuhmacher, K. Müller, J. Bill and F. Aldinger, J. Am. Ceram. Soc. **85**, 1807 (2002).
[34] Y. Cai, S. Prinz, A. Zimermann, A. Zern, W. Sigle, M. Rühle and F. Aldinger, Sripta Materialia **47**, 7 (2002).
[35] A. Zern, J. Mayer, N. Janakiraman, M. Weinman, J. Bill and M. Rühle, J. Eur. Ceram. Soc. **2**, 1621 (2002).
[36] J. Haug, P. Lamparter, M. Weinmann and F. Aldinger, Chem. Mater. **16**, 83 (2004).
[37] N. Janakiraman, A. Zarn, M. Weinmann, F. Aldinger and P. Singh, J. Eur. Ceram. Soc. **25**, 509 (2005).
[38] H. Schmidt, W. Gruber, G. Borchardt, P. Gerstel, A. Müler and N. Bunjes, J. Eur. Ceram. Soc. **25**, 227 (2005).
[39] J. Vlček, S. Potocký, J. Čížek, J. Houška, M. Kormunda, P. Zeman, V. Peřina, J. Zemek, Y. Setsuhara and S. Konuma, J. Vac. Sci. Technol. A **23**, 1513 (2005).
[40] J. Houška, J. Vlček, Š. Potocký and V. Peřina, accepted for publication in Diamond Relat. Mater. (2006).
[41] J. Čížek, J. Vlček, L. Martinů, A. Amassian, Š. Potocký, J. Houška and Z. Soukup, prepared for publication in Thin Solid Films
[42] J. Čížek, Reactive plasma deposition of hard films Si-(B)-C-N and their properties, Ph.D. thesis (in Czech, University of West Bohemia, 2004).
[43] Š. Potocký, Reactive magnetron depositions of new thin film materials Si-B-C-N with unique properties , Ph.D. thesis (in Czech, University of West Bohemia, 2006).
[44] N. Cooper, Molecular Dynamics Simulations of Amorphous Silicon Carbon Alloys, Ph.D. thesis (The University of Sydney, 2004).
[45] N.A. Marks, Phys. Rev. B **56**, 2441 (1997).
[46] N.A. Marks, N.C. Cooper, D.R. McKenzie, D.G. McCulloch, P. Bath and S.P. Russo, Phys. Rev. B **65**, 75411 (2002).
[47] D.G. McCulloch, D.R. McKenzie and C.M. Goringe, Phys. Rev. B **61**, 2349 (2000).
[48] M.M.M. Bilek, D.R. McKenzie, D.G. McCulloch and C.M. Goringe, Phys. Rev. B **62**, 3071 (2000).
[49] A.R. Merchant, D.R. McKenzie and D.G. McCulloch, Phys. Rev. B **65**, 24208 (2001).

[50] D.G. McCulloch, D.R. McKenzie and C.M. Goringe, J. Appl. Phys. **88**, 5028 (2000).
[51] P. Fitzhenry, M.M.M. Bilek, N.A. Marks, N.C. Cooper and D.R. McKenzie, J.Phys.: Condens. Matter. **15**, 165 (2003).
[52] D. K. Remler and P.A. Madden, Mol. Phys. **70**, 921 (1990).

2 Methodology

First part of this chapter describes in detail reactive magnetron sputtering of Si-B-C-N materials, evaluating of process characteristics and measurements of properties of Si-B-C-N materials. Only the properties discussed further in the thesis are included. Second part of this chapter describes density functional theory simulations of structures of amorphous materials using the liquid-quench algorithm, and interpretation of bonding in obtained structures.

2.1 Methods used for synthesis and characterisation

2.1.1 Reactive magnetron sputtering of Si-B-C-N materials

Magnetron sputtering is one of Physical Vapour Deposition (PVD) techniques. It allows depositions of thin films of various materials by sputtering of elementary, alloy, compound or composite targets by positive ions in a plasmatic discharge. Sputtered particles together with particles of the discharge gas condense on opposite substrates and form the growing film. Magnetron placed below the sputtered target keeps free electrons in vicinity of the target, which increases degree of ionisation in the plasma and therefore increases efficiency of the sputtering. Structure and properties of the deposited films can de controlled mainly by composition of sputtered target, composition of the discharge gas mixture, substrate temperature and ions bombarding the growing film due to negative substrate bias.

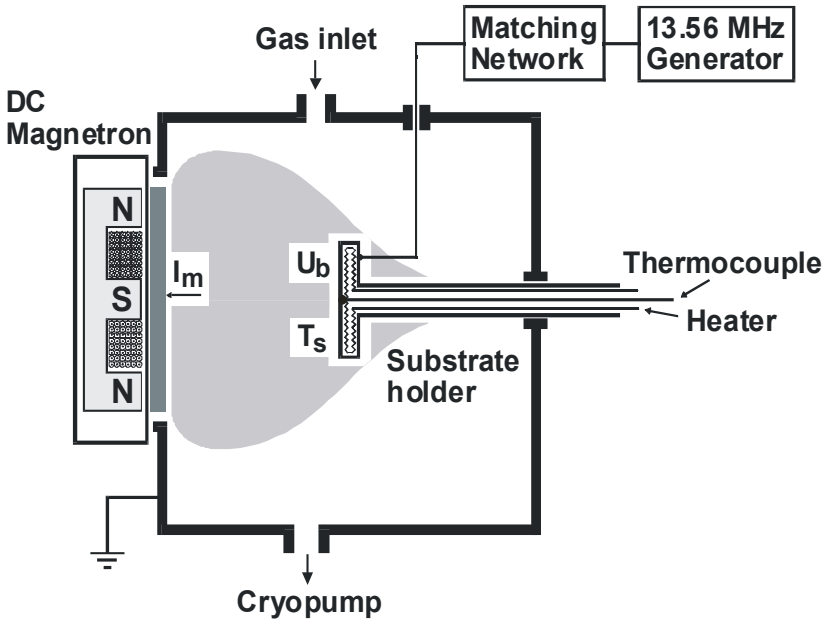

Fig. 2.1: *The Balzers BAS 450 PM Cryo sputtering system used for depositions of Si-B-C-N materials. The discharge current on the magnetron target, I_m, was 1 A, and the negative substrate bias voltage, U_b, induced by the rf generator varied from -38 V to -700 V. The substrate temperature, T_s, was either maintained at 350 °C by an ohmic heater or allowed to equilibrate in the range 180 to 250 °C.*

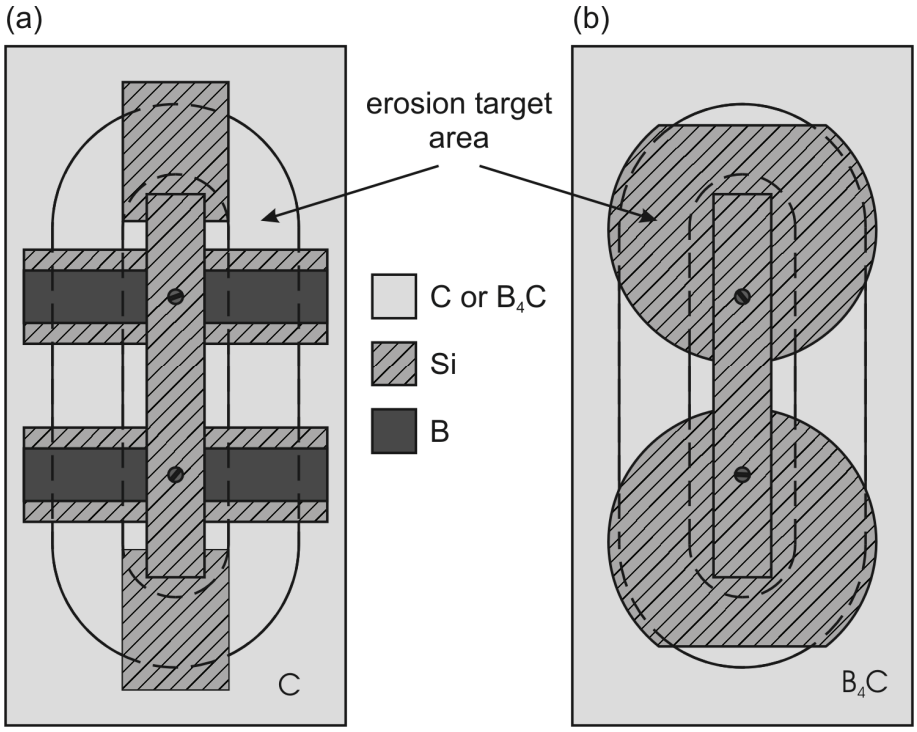

Fig. 2.2: *Geometric configuration of sputtered targets used for depositions of Si-B-C-N films: C-Si-B (a) and B_4C-Si (b).*

Magnetron sputtering is one of the most versatile techniques compatible with semiconductor technologies and its further important advantage is an easy up-scaling Contrary to some other techniques such as Chemical Vapour Deposition (CVD), it allows film generation at noticeably reduced substrate temperatures and without hydrogen-containing precursors resulting in an enlarged residual content of hydrogen in films.

For our experiments, we used a Balzers BAS 450 PM Cryo sputtering system with a planar rectangular unbalanced magnetron and a modified circular substrate holder (125 mm in diameter)[1] – see Fig. 2.1. The Si–B–C–N films were deposited on p-type Si(100) substrates using dc magnetron co-sputtering of silicon, boron and carbon from high-purity composite targets (127×254×6 mm^3). The targets used were C-Si-B: graphite overlapped by p-type Si and B stripes fixed to the target (see Fig. 2.2(a)), and B_4C-Si: boron carbide overlapped by p-type Si stripes (see Fig. 2.2(b)).

The Si fraction in the erosion target area was varied from 5 to 75 % for both targets, and the B fraction in the erosion target area was fixed at 20 % for the C-Si-B target. The total pressure of nitrogen-argon gas mixtures, p, was 0.5 Pa at the argon fraction in the gas mixture ranging from 0 to 75 % and at a constant gas flow approximately 25 sccm. The target-to-substrate distance was 100 mm. The discharge current on the magnetron target, I_m, was held constant at 1 A, and the negative substrate bias voltage, U_b, induced by an rf generator operating at a frequency of 13.56 MHz, was varied from a floating potential of approximately -38 V to -700 V. The substrate temperature, T_s, was adjusted at 350 °C by an ohmic heater or it was in the range from 180 to 250 °C without the heater. For comparison purposes, results on Si-B-C (100 % of Ar in the gas mixture) and B-C-N (0% of Si in the erosion area of the B_4C-Si target) materials are also included in this work.

2.1.2 Evaluating of discharge and deposition characteristics

The energy and total flux of ions bombarding the target and the growing films were evaluated on the basis of the discharge characteristics measured for both the dc magnetron discharge and the rf discharge dominating in the deposition zone[1]. The discharge current on the magnetron target, I_m, and the corresponding cathode-anode voltage of the magnetron, U_{dc}, the time-averaged rf power, R_{rf}, absorbed by the plasma and the corresponding negative substrate bias voltage, U_b, relative to ground potential, were measured using respective units built into the dc and rf power supplies of the Balzers system. Only a slight effect (< 10 %) of the non-ideal matching network on the P_{rf} measurements under the given experimental conditions was proved by calorimetric tests after optimization of the electrical connection between the matching network and the substrate holder. Let us note that the measured P_{dc} and P_{rf} power values must be related to the magnetron erosion track area (A_m = 140 cm^2) and the area of the unshielded substrate holder (A_s = 620 cm^2), respectively, in order to obtain the respective power densities absorbed near the target and substrate. In addition, the value of pressure p = 0.5 Pa was shown to be sufficiently low to ensure a collisionless motion of ions across the dc and rf sheaths under the conditions investigated[1].

Energy transfer and other processes affecting the energy balance in the low-pressure capacitive rf discharges were analyzed using the models given in Ref. 2. Such low-pressure discharges are strongly asymmetric due to a large difference between the area of the substrate holder A_s = 620 cm^2 and the total grounded area (10000 cm^2), leading to a high-voltage sheath near the powered substrate. The power balance equation can be then written as

$$P_{rf} = \Gamma_i A_s (E_i + E_c + E_e) \qquad \text{(Eq. 2.1)},$$

where Γ_i is the total time-average ion flux onto the substrate holder, E_i is the mean kinetic energy transferred by an ion to the powered electrode, E_c is the mean kinetic energy lost by an electron per electron-ion pair created in the gas mixture, and E_e is the mean kinetic energy transferred by an electron to the grounded chamber walls. The Γ_i values can be obtained from the P_{rf} measurements if we take into account that for our high-voltage sheaths the effect of a low plasma potential V_p can be neglected in the term for the mean ion kinetic energy $E_i = e(V_p - U_b)$ and that it can be put $E_c + E_e$ = 50 eV under a realistic assumption of a constant electron temperature T_e = 3 eV in the substrate region[2]. The ion energy per deposited atom, E_{ia}, was determined as

$$E_{ia} = e|U_b|\Gamma_i/\Gamma_p \qquad \text{(Eq. 2.2)},$$

where the flux of film-forming particles onto the substrate, Γ_p, was calculated using a known atomic density of the films per unit area (determined by Rutherford back-scattering spectrometry) and a time of deposition.

2.1.3 Characterization of Si-B-C-N materials

The film thickness (up to 7 μm) and a bending of the substrate after deposition of the film, from which a residual macrostress was determined using the Stoney's formula[3], were measured by profilometry (Dektak 8 Stylus Profiler, Veeco). Atomic force microscopy (Metris 2001A-NC Microscope, Burleigh Instruments) observation showed a very smooth surface morphology of the as-deposited layers with an average roughness Ra ≤ 0.8 nm. X-ray diffraction analysis (Dron IV Diffractometer upgraded by Seifert GmbH) indicated their amorphous structure.

The elemental composition of the Si-B-C-N films (with small contents of Ar, H and O) was determined by Rutherford backscattering spectrometry (RBS) and elastic recoil

detection (ERD) methods[4] using a Van de Graaf generator with a linear electrostatic accelerator. The contents of Ar, B, C, N, O and Si were measured by RBS using 2.390, 2.336 and 1.765 MeV (for carbon) protons as projectiles, scattered under the angle of 170°. The neutron depth profiling (NDP) was used to specify the boron content estimation when it was necessary. The content of H was measured by ERD with an incident beam of 2.75 MeV alpha particles at 75° to the sample surface normal The hydrogen atoms recoiled under the angle of 30° were detected with a surface barrier detector covered by a 10 μm thick mylar stopping foil. The RBS and ERD measurements were evaluated by computer codes GISA[5] and SIMNRA[6], respectively, using cross-section values from SigmaBase[7].

The chemical structure was analyzed by infrared variable angle spectroscopic ellipsometry (IR VASE). The IR VASE spectra were measured between 1.34 and 34 μm (i.e. approx. from 7000 to 220 cm^{-1}) using 3 angles of incidence 65, 70 and 75°, respectively. Similar to VIS VASE, these measurements were taken in reflection; therefore, the influence of substrate absorption, which is a critical factor in standard FTIR spectroscopy, was eliminated. Contrary to FTIR measurements, IR VASE (as ellipsometry in general) did not directly measure the absorption coefficient α, but it was determined from a simulation of the optical behavior in the IR region. The physical model used for IR VASE data consisted of a Si substrate with a native SiO_2 layer, a 'general oscillator' Si-B-C-N layer and a surface roughness layer. In the 'general oscillator' model, interband absorptions were simulated by Gaussian type oscillators; their parameters were found during a fitting procedure. Detected inhomogenenities were not larger than 10%.

Film hardness, effective Young's modulus, $E/(1 - \nu^2)$, where E and ν are the Young's modulus and the Poisson's ratio, respectively, and elastic recovery were determined using a computer-controlled microhardness tester (Fischerscope H-100B) which automatically records the depth of indentation of a Vickers diamond pyramidal tip, while increasing the applied load up to a preset maximum. The plastic hardness was calculated from the indentation depth after unloading, and it was corrected for the indentation size effect. To obtain reliable hardness values of the films (see, for example, Ref. 8), measurements were performed with a maximum load of 30 and 50 mN.

Resistivity of selected Si-B-C-N samples, deposited on non-conductive glass substrates, was measured by the four points technique (with 1.047 mm spacing between tips).

2.2 Methods used for atomistic simulations

2.2.1 Ab-initio simulations

Levels of simplification used in molecular and material simulations include (starting with the most exact ones) quantum chemical methods, density functional theory, environment-dependent interaction potentials-based methods, tight binding methods and empirical potentials-based methods. Detailed overview of them together with comparing of simulation results can be found in Ref. 9. First two of listed methods are *ab initio* – that is, they do not include any empirical fitting parameters. All calculations reported in this work use the density functional theory (DFT)[10,11] which is based on the following theorems and simplifications:

(1) Instead of the (relativistic) Dirac equation the (unrelativistic) Schrödinger equation can be used for light atoms where the relativistic effects are negligible

(2) The many-electron problem can be transposed to many one-electron equations (Schrödinger-type) coupled by an effective potential given by the electron charge density n(**r**). It holds

$$n(\mathbf{r}) \geq 0 \text{ and } \int n(\mathbf{r})d\mathbf{r} = N \qquad \text{(Eq. 2.3, 2.4)}$$

where N is a total number of electrons.

(3) The total energy E[n(**r**)] can be minimized so

$$E[n(\mathbf{r})] \geq E[n_0] = E_0 \qquad \text{(Eq. 2.5).}$$

(4) It holds (Hohenberg and Kohn)

$$E[n(\mathbf{r})] = \int v(\mathbf{r})n(\mathbf{r})\mathbf{dr} + F[n(\mathbf{r})] \qquad \text{(Eq. 2.6)}$$

where v(**r**) is an external potential (due to the ions) and F[n(**r**)] is universal functional valid for any v(**r**):

$$F[n(\mathbf{r})] = 1/2\iint n(\mathbf{r})n(\mathbf{r'})/|\mathbf{r}-\mathbf{r'}|d\mathbf{r}d\mathbf{r'} + T[n(\mathbf{r})] + E_{xc}[n(\mathbf{r})] \qquad \text{(Eq. 2.7).}$$

The first term accounts for the long-range Coulomb interaction and T[n(**r**)] is the kinetic energy of electrons. The exchange and correlation energy E_{xc} accounts for the antisymmetric nature of any true many-electron wavefunction with respect to exchange of spin and space coordinates of any pair of electrons, and for self-interaction of the electron with itself (which would be otherwise included in the calculation).

(5) The system of the one-electron Schrödinger-like equations (Kohn-Sham equations) can be then written as

$$(-1/2\nabla^2 + v(\mathbf{r}) + \int n(\mathbf{r})/|\mathbf{r}-\mathbf{r'}|d\mathbf{r'} + \mu_{xc}[n(\mathbf{r})])\psi_i = \varepsilon_i\psi_i \qquad \text{(Eq. 2.8)}$$

where

$$\mu_{xc}[n(\mathbf{r})] = \partial E_{xc}[n(\mathbf{r})]/\partial n(\mathbf{r}) \qquad \text{(Eq. 2.9).}$$

In general case, the Lagrange parameters ε_i have not any physical meaning (the only aim is to calculate the wavefunction).

(6) Classes of methods treating the exchange and correlation potential μ_{xc} include the local density approximation (LDA) where only dependence on local electron charge density is considered:

$$\mu_{xc}[n(\mathbf{r})] \approx \mu_{xc}^{LDA}[n(\mathbf{r})] \qquad \text{(Eq. 2.10),}$$

the local spin density approximation (LSD) where the spin effects are incorporated:

$$\mu_{xc}[n(\mathbf{r})] \approx \mu_{xc}^{LSD}[n\uparrow(\mathbf{r}), n\downarrow(\mathbf{r})] \qquad \text{(Eq. 2.11),}$$

and the generalised gradient approximation (GGA) which incorporates also the non-local contributions:

$$\mu_{xc}[n(\mathbf{r})] \approx \mu_{xc}^{GGA}[n(\mathbf{r}), \nabla n(\mathbf{r})] \qquad \text{(Eq. 2.12).}$$

The *ab initio* molecular dynamics (MD) method integrates the classical equations of motion for the nuclei and thereby provides insights into the time-evolution of the system. For simulations of our materials we employed the DFT as implemented in the Car-Parrinello Molecular Dynamics (CPMD) software[12]. This particular implementation used has the following features:

(1) Atom cores and the core electrons are represented using pseudopotentials. A pseudopotential is a potential that gives rise to wavefunctions identical in shape with those of true valence wavefunctions outside the core region, but without nodes inside the core region. Such pseudo-wavefunctions can be accurately represented with far fewer plane waves than are required to represent the true valence wavefunction[13]. For our calculations we used the Goedecker-type pseudopotentials[14].

(2) The Kohn-Sham equations for the valence electrons are expanded in a basis of plane wave functions; in our case with an energy cut-off of 60 Ry. This value was found to be sufficient to reproduce measured data for a number of related molecular structures (see below). Exchange and correlation terms were treated in the generalised gradient approximation (GGA) using the BLYP functional[15,16].

(3) The electronic problem is solved in parallel with motion of nuclei (positive ions) by introducing a fictitious classical dynamics for electrons. Instead of optimizing wavefunction after each ionic step, in the same time step the ions are moved according to the self-consistent forces, while the electronic variables are moved according to the electronic gradients and constraints. All MD runs were performed using an as long as possible time step of 0.073 fs (3 atomic units, the calculations were becoming unstable for time steps ≥ 4 atomic units). The fictitious electron mass (required for the classical integration of the electronic degrees of freedom) was set to 200 m_e.

(4) Calculations were performed in a three-dimensionally periodic cubic cell at the gamma-point only - in other words, terms in the wavefunctions with wavelengths longer than the cell size were not considered. This is well possible for disordered systems where we expect the orbitals to be relatively localised[13].

The accuracy of this method as well as the convergence of calculated properties with respect to plane-wave cut-off was confirmed using simulations of 8 representative molecules ($B_3N_3H_6$, silacyclobutane SiC_3H_8, trimethylborane $B(CH_3)_3$, pyrrole NC_4H_5, pyrazine $N_2C_4H_4$, silyl cyanide $SiCNH_3$, $(SiH_3)NCN$ and trimethylamineborane $(CH_3)_3NBH_3$). Calculated energies were within 1 % of the asymptotic value for large plane wave cut-off. Typical differences after geometry optimisations between the experimental and simulated bond lengths and angles were only 1-2 %, with convergence for N and B slightly worse than for Si, C and H. Fig. 2.3 shows geometry optimization results for the $B_3N_3H_6$ molecule.

2.2.2 The liquid-quench algorithm

Amorphous (Si)-(B)-C-N materials were studied by molecular dynamics simulations using a *liquid-quench* algorithm. This algorithm attempts to capture the formation conditions of the real materials, which arise from rapid cooling of the localized melt (thermal spike) created around sites of energetic ion impact.

It is not possible using presently available quantum theoretical methods to simulate the full ion bombardment process. We simplify the process by assuming that the primary impact creates a localized region of high temperature, commonly referred to as a *thermal spike*. Thermal spikes have a cooling time sufficiently short to be simulated using ab initio MD methods as shown in Ref. 17. These cooling times can be estimated using the heat diffusion equation together with literature values for the thermal diffusivity and the thermal spike radius[17]. The thermal spike simulation method has been used successfully to predict the structure of carbon materials formed from ion beams having a range of energies[18]. Our liquid quench simulations were performed in a number of stages:

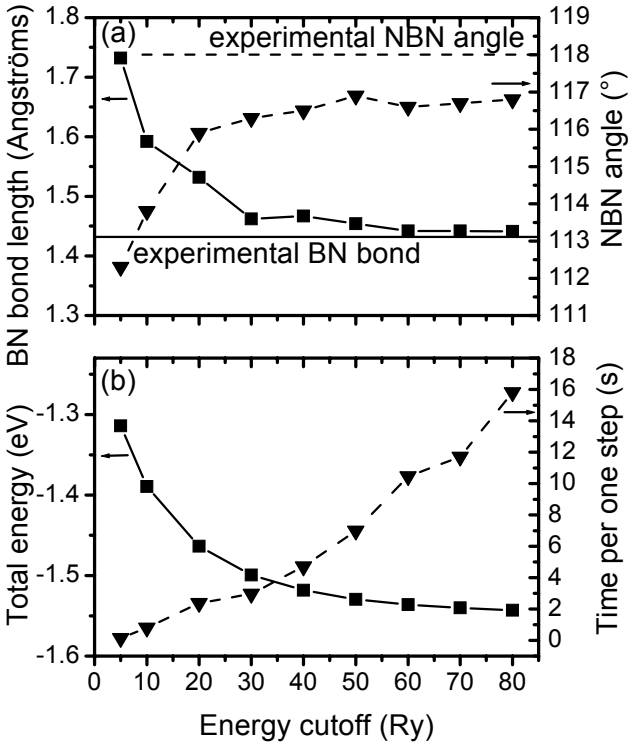

Fig. 2.3: *Results after optimizing of geometry of $B_3N_3H_6$ molecule at various energy cutoffs. Panel (a) shows convergence of selected geometric quantities. Panel (b) shows convergence of total energy and an averaged time needed for one optimization step. Molecule was placed in 12 Å cubic cell with periodic boundary conditions applied.*

(1) *Start-up*: Alternately distributing of atoms of all types over the simulation cell (most typically using a simple tetragonal structure – e.g. four 5×5 planes for 100 atoms) followed by a random shift of atoms (with an amplitude of 1 Å) generated a semi-random initial start-up structure.

(2) *Initial Mixing*: In order to obtain a completely randomized structure with no memory of the initial structure, an MD run of 1 ps length at a temperature of at least 5000 K (Nose-Hoover thermostat) was carried out. The mixing was considered to be sufficient when the square root of the mean squared displacement (MSD) was longer than half of the cell size as described previously[9]. A significantly reduced plane-wave cut-off of 10 Ry was adopted for this stage of the simulation only. High accuracy of the DFT energies is not required for this stage and cut-off reduction increases the efficiency of this stage of the simulation dramatically. Low cut-off was also found useful since it effectively prevents the formation of stable bonds, which would interfere with efficient mixing.

(3) *Exponential Cooling*: After wavefunction optimisation, the material was exponentially cooled to its (rounded) deposition temperature of 650 K. Temperature control was achieved by velocity scaling of ions when actual and target temperature differed by more than 10%. Various cooling times were used in the simulations.

(4) *Equilibration*: After the cooling phase, sample equilibration was accomplished using a 1 ps MD run at 650 K (Nose-Hoover thermostat). The purpose of equilibration is for the system to fully recover thermal equilibrium as indicated by a constant mean squared displacement.

(5) *Production Run:* Following equilibration, various quantities of interest (bonding statistics, Kohn-Sham energies and stresses) were computed as statistical averages over at least 0.5 ps long MD run at 650 K.

(6) *Post-processing*: The stable structure obtained at the end of the liquid quench algorithm is wavefunction optimised at two cut-offs above and below 60 Ry in order to estimate the Pulay correction of the averaged stress[19]. Same structure was used as a basis of calculations of other properties of interest (such as thermal stability or optical conductivity) described in detail in respective chapters.

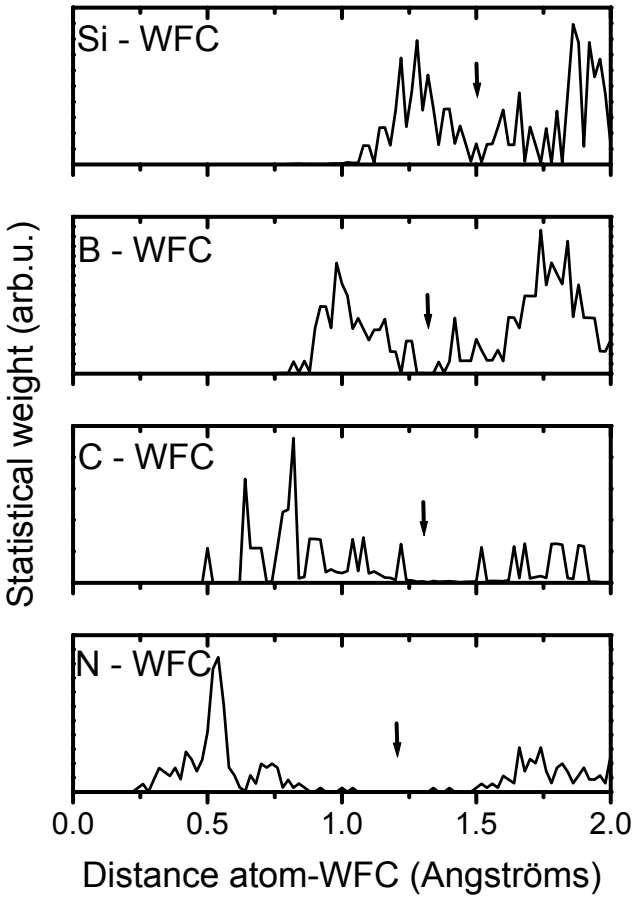

Fig. 2.4: *Pair correlation functions of Si, B, C and N atoms with nearby Wannier function centres for Si-B-C-N sample of composition* $Si_{14}B_{23}C_6N_{55}$. *The arrows denote suitable positions of distance cutoffs.*

2.2.3 Bonding analysis

Our bonding analysis is based on representation of valence electrons by maximally localized Wannier function centres (WFC)[20]. In this concept, the Bloch states are expressed as a sum of orthogonal functions w_n with their total spread - for n-th function

$$\sigma_n = \sqrt{< r^2 >_n - < r >_n^2} \qquad \text{(Eq. 2.13)}$$

- minimized in the space. To simplify the analysis, rather than visualize the spatial structure of maximally localized Wannier functions, only the coordinates of Wannier function centers are calculated as

$$x_n = -\frac{L}{2\pi}\,\mathrm{Im}\ln < w_n \mid e^{-i\frac{2\pi x}{L}} \mid w_n > \qquad \text{(Eq. 2.14)}$$

(and similarly for y_n, z_n), where L is the periodical cell size.

For our structures, we calculate the pair correlation functions of Si, B, C and N atoms with nearby WFCs. The first minimum in these pair functions defines a distance cut-off for each atom type as shown in Fig. 2.4. This gives for each WFC a set of associated atoms located within the cut-off for that atom type. If the set contains only one atom, the WFC is classified as a lone-pair. If the set contains two atoms, the WFC is classified as a bonding electron pair representing a bond between these two atoms. Multiple bonds are characterised by multiple WFCs between the same two atoms. Three centre, two electron bonds are characterised by a WFC associated with three atoms. We ascribe strength 0.5 to the bonds arising from this electron pair between the closest atom to the WFC and the two others. The bond strength between any two atoms is obtained by summing the contributions from all WFCs associated with that pair. This interpretation ensures that the sum of strengths of all bonds is equal to the number of bonding electron pairs in the network. For purposes where matters only an existence or non-existence of a bond (such as calculating of network rings), any pair of atoms linked with bond strength ≥ 0.5 was considered as bonded.

2.3 References

1 J. Vlček, K. Rusňák, V. Hájek and L. Martinů, J. Appl. Phys. **86**, 3646 (1999).
2 M. A. Lieberman and A. J. Lichtenberg, Principles of Plasma Discharges and Materials Processing (Wiley Interscience, New York, 1994).
3 J. Gunnars and U. Wiklund, Mater. Sci. Eng. A **336**, 7 (2002).
4 J. R. Tesmer and M. Nastasi (Eds.), Handbook of Modern Ion Beam Materials Analysis (Material Research Society, Pittsburgh, PA, 1995).
5 J. Saarilahti and E. Rauhala, Nucl. Instrum. Method Phys. Res. B **64**, 734 (1992).
6 M. Mayer, SIMNRA, User's Guide (Forschungscentrum Jülich, Institute for Plasma Physics, Germany, 1998).
7 Available from http://ibaserver.physics.isu.edu/sigmabase/.
8 S. Vepřek, J. Vac. Sci. Technol. A 17, 2401 (1999).
9 N. Cooper, Molecular Dynamics Simulations of Amorphous Silicon Carbon Alloys, Ph.D. thesis (The University of Sydney, 2004).
10 P. Hohenberg and W. Kohn, Phys. Rev. B **136**, 864 (1964).
11 W. Kohn and L. Sham, Phys. Rev. A **140**, 1133 (1965).
12 CPMD, Copyright IBM Corp. 1990-2006, Copyright MPI fűr Festkörperförschung Stuttgart 1997-2001.
13 D. K. Remler and P. A. Madden, Mol. Phys. **70**, 921 (1990).
14 S. Goedecker, M. Teter and J. Hutter, Phys. Rev. B **54**, 1703 (1996).
15 A.D. Becke, Phys. Rev. A **38**, 3098 (1988).
16 C. Lee, W. Yang and R.G. Parr, Phys. Rev. B **37**, 785 (1988).
17 N.A. Marks, Phys. Rev. B, **56**, 2441 (1997).
18 D.G. McCulloch, D.R. McKenzie and C.M. Goringe, Phys. Rev. B **61**, 2349 (2000).
19 S. Froyen and M.L. Cohen, J. Phys. C: Solis State Phys. **19**, 2623 (1986).
20 R. Resta, Phys. Rev. Lett. **80**, 1800 (1998).

3 Influence of target and gas composition on structure and properties of Si-B-C-N films

This chapter is based on part of results published in Refs. 1 and 2, while summary of all achievements is provided in the first chapter (section 1.2.1).

As a result of short chemical bonds with low polarities and high average coordination numbers of elements, compounds within the Si–B–C–N system can form superhard materials (see, for example, Refs. 3 and 4). We systematically investigated reactive dc magnetron sputtering of Si–B–C–N films using a composite C–Si–B target in nitrogen-argon gas mixtures. The main aim of our work was to develop a reproducible process for the formation of hard Si–B–C–N films with a high oxidation resistance at elevated temperatures, low internal stresses and good adhesion to various substrates. In this chapter, we report on the effect of Si fraction in the C–Si–B target and the effect of the N_2–Ar gas mixture composition on the elemental composition, bonding structure and mechanical properties of the films prepared at a range of negative substrate biases and substrate temperatures ($\leq$ 350 °C). Furthermore, we report on the effect of Si content in Si-B-C-N films on compressive stress generated in the films by implanted Ar atoms.

3.1 Experimental conditions

The effect of the C–Si–B target composition on characteristics of the Si–B–C–N films (Figs. 3.3–3.5) is presented for a fixed 20 % boron fraction in the erosion area of the target, a 50 % N_2 + 50 % Ar gas mixture and two different choices of the U_b and T_s values. In case of U_b = -500 V and T_s = 350 °C we were interested in examining the effect of ion bombardment and high substrate temperature simultaneously during film growth. In the second set of experimental conditions no rf-induced substrate bias was applied or ohmic heater used. In this case the substrate was at floating potential, $U_s = U_f$ = -15 to -38 V, with a temperature of T_s = 180–190 °C.

The effect of the N_2–Ar gas mixture composition characteristics of the Si–B–C–N films (Figs. 3.6-3.8) is presented for a fixed composition (60 % Si +20 % B+20 % C) in the erosion target area, with T_s = 350 °C and two different values of U_b = -100 and -500 V.

In order to examine compressive stress as a function of Si and Ar content, a set of 30 samples was prepared by combining six different B_4C-Si target compositions with five different deposition conditions (gas composition, substrate bias and temperature). The six target compositions were $Si_x(B_4C)_{100-x}$ with x=0, 5, 20, 40, 60, 75. The five depositions conditions were: (1) 50% Ar + 50% N_2 gas mixture and substrate temperature of 350 °C with U_b = -100 V; (2) Same with U_b = -500V; (3) 75% Ar + 25% N_2 gas mixture with U_b = -100 V and substrate temperature of 700 °C; (4) same with substrate temperature of below 180-190 °C (no ohmic heating) and (5) discharge gas of 100% Ar with U_b = -100V and substrate temperature of 350 °C. Compressive stresses and elemental compositions were measured for all thirty samples.

3.2 Specification of hardness measurements

Hardness (and the other mechanical properties) of the films was determined using the Fischerscope H-100B microhardness tester (see chapter 2). For each selected maximal load of the diamond tip, the loading-unloading indentation curves were measured for least at 27 points, with loading and unloading times (60 s) sufficiently high to obtain values independent of these times. An example of the averaged loading-unloading curve is given in figure 3.1. A tangent line was made using the top 30% of the averaged unloading curve, and the "corrected depth" $h_{r'}$, defined by the point of intersection of the tangent with the indentation depth axis, was evaluated. The plastic hardness was then calculated as

$$H_{plast} = \frac{L}{26.43 h_{r'}^{2}} \qquad \text{(Eq. 3.1)},$$

where L is the maximal load and 26.43 $h_{r'}^2$ is a contact area of the Vickers diamond tip with a sample at indentation depth $h_{r'}$.

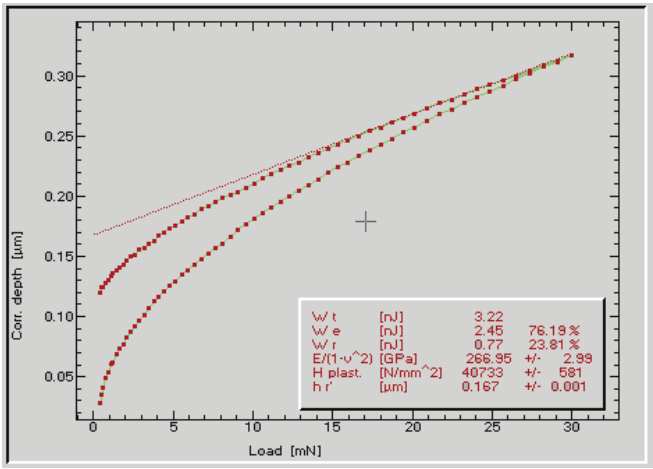

Fig. 3.1: *Avegage over loading-unloading indentation curves measured on a typical Si-B-C-N sample (copied from the screen of the Fischerscope H-100B microhardness tester). The line is a tangent made using top 30% of the unloading part of the curve. The calculated quantities W_t, W_e, W_r, $E/(1-\nu^2)$, H_{plast} and $h_{r'}$ are total, elastic and plastic work of the indentor, modified Young's modulus, plastic hardness and depth defined by the point of intersection of the tangent with the indentation depth axis, respectively.*

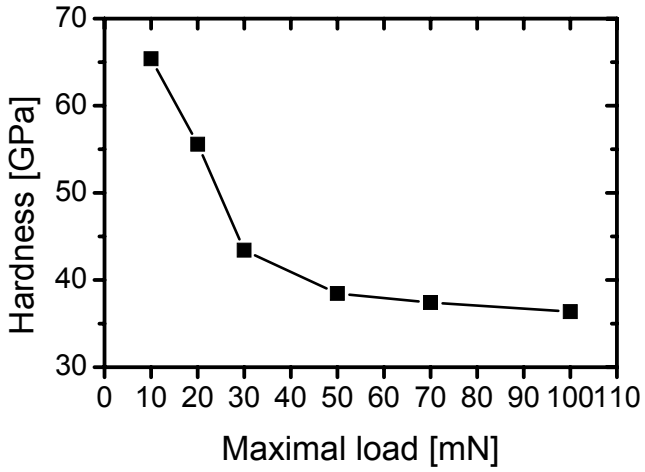

Fig. 3.2: *Dependence of measured plastic hardness on maximal load for a typical Si-B-C-N sample. Sample thickness was 7.2 μm, and the maximal indentation depth was less than 10% of the thickness for all loads shown.*

Note that measured values of hardness depend on the load used because (1) at low loads the hardness value cannot be determined with precision owing to the large elastic recovery, dominating the load-unload curves[5], while (2) at high loads, leading to maximal indentation depths over 5-10 % of the sample thickness, the evaluated hardness may be underestimated due to the effect of the softer substrate[4]. Figure 3.2 shows dependence of hardness on the load used for a Si-B-C-N sample of exceptionally high thickness of 7.2 μm, where the indentation depths were less than 10% of 7.2 μm for all loads up to 100 mN. It can be seen that the measured values are overestimated for loads up to 30 mN. However, at a higher load of 50 mN the indentation depths were already too high (occasionally over 30% of the film thickness) for most of the Si-B-C-N samples studied in chapters 3 and 4 (film thickness starting at 1.0 μm). The hardness values are therefore presented at the both loads of 30 and 50 mN, which best fulfils the conditions mentioned above.

3.3 Results

3.3.1 Effect of the magnetron target composition

In Fig. 3.3(a) it is shown that the increasing silicon fraction in the erosion target area results in a rising incorporation of silicon (from 10 to 29 at. % for U_b = -500 V and T_s = 350 °C, and from 8 to 30 at. % for U_s = U_f = -15 to -38 V and T_s = 180–190 °C) and nitrogen (from 32 to 46 at. % and from 36 to 50 at. %, respectively) into the films, while the carbon content decreases (from 35 to 5 at. % and from 40 to 2 at. %, respectively) with a slowly decreasing boron content (from 12 to 7 at. %) for U_b = -500 V and T_s = 350 °C, and practically constant boron content (from 10 to 8 at. %) for U_s = U_f = -15 to -38 V and T_s = 180–190 °C. The incorporation of Si raises the N content in the layers apparently due to preferred formation of Si–N bonds.[6,7] In addition, the substantially lower values obtained for the C content in the films prepared with high substrate bias and temperature (U_b = -500 V and T_s = 350 °C) can be mainly explained by a strong ion-induced and thermal desorption of loosely bonded C–N species from the surface of growing films[8] (as indicated by decrease of the deposition rates under these conditions - Ref. 1).

Figure 3.3(b) provides information on the content of hydrogen, oxygen and argon in the Si–B–C–N films. The hydrogen content is in the range from 5 to 9 at. % for samples

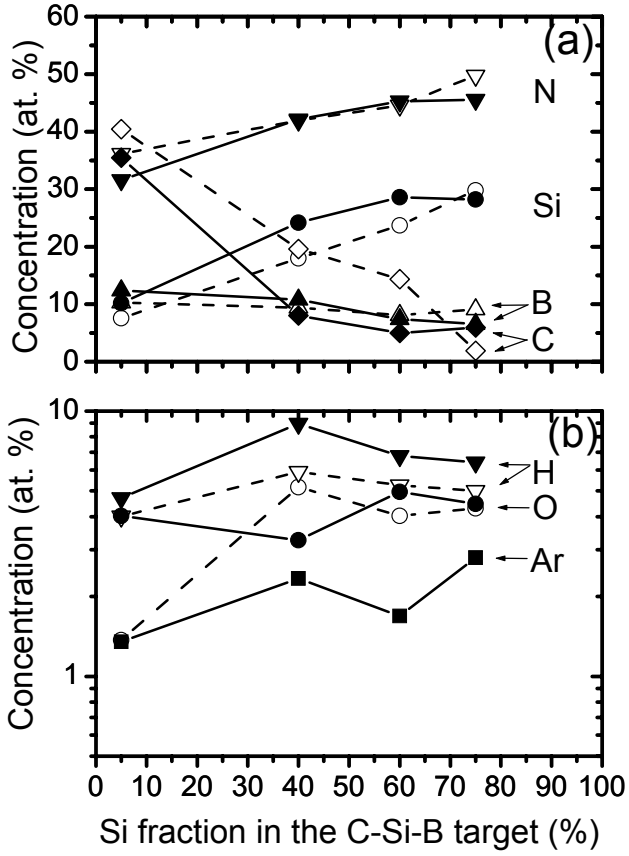

Fig. 3.3: *Elemental composition of films prepared in a 50 % N_2 + 50 % Ar gas mixture at various silicon fractions in the erosion target area for U_b = -500 V and T_s = 350 °C (full symbols), and U_s = U_f = -15 to -38 V and T_s = 180 - 190 °C (empty symbols).*

deposited with high substrate bias compared to 4-6 at. % for low bias conditions. The oxygen content (3–5 at. %) is also greater in the case of high applied bias. This may be due to subplantation of hydrogen and oxygen atoms into the films from the discharge plasma. A maximum value (9 at. %) determined for a residual content of hydrogen in our films is still considerably lower than the usual values (approximately 15 at. %) reported in the literature[6,9] for Si–B–C–N films prepared by plasma-assisted chemical vapor deposition using H-containing precursors at reduced substrate temperatures. An increasing subplantation of argon into the films (up to 3 at. %) with the silicon fraction in the erosion target area [Fig. 3.3(b)] has been correlated with stronger ion bombardment (higher Γ_i/Γ_p ions to film-forming particles flux ratio)[1]. The higher Γ_i/Γ_p flux ratio at higher silicon fraction in the erosion target area is caused by an increasing plasma conductivity due to a higher secondary electronic emission coefficient and sputtering yield of silicon compared with carbon[10].

Information about the chemical structure was obtained from IR VASE measurements. Figure 3.4 shows that for the highest Si, the dominant absorption peak is due to a presence of Si-N bond (960 cm^{-1})[11]. This peak decreases as the silicon fraction decreases and characteristic peaks due to the presence of C-C (1360-1580 cm^{-1})[11], C=C (1600-1630 cm^{-1})[12] , C(sp^3)-N(1300 cm^{-1})[12] and C(sp^2)-N (1600 cm^{-1})[11] bonds increase. In addition, the peak of B(sp^2)-N (1385 cm^{-1})[13] bond was identified. In the region around 1100 cm^{-1} possible contributions to the absorption co-efficient could arise from an asymmetric vibration due to the Si-O (1090-1110 cm^{-1})[14] bond, absorption due to the B-C (1100 cm^{-1})[13,15] bond and/or the B(sp^3)-N (1060-1100 cm^{-1})[13] bond. The freestanding peak in the region of high energies could arise from the presence of C(sp)-N (2200 cm^{-1})[11] and/or Si-H (2100 cm^{-1})[14] bonds. The absorption peak due to the Si-N bond in the low energy region is likely to be broadened due to

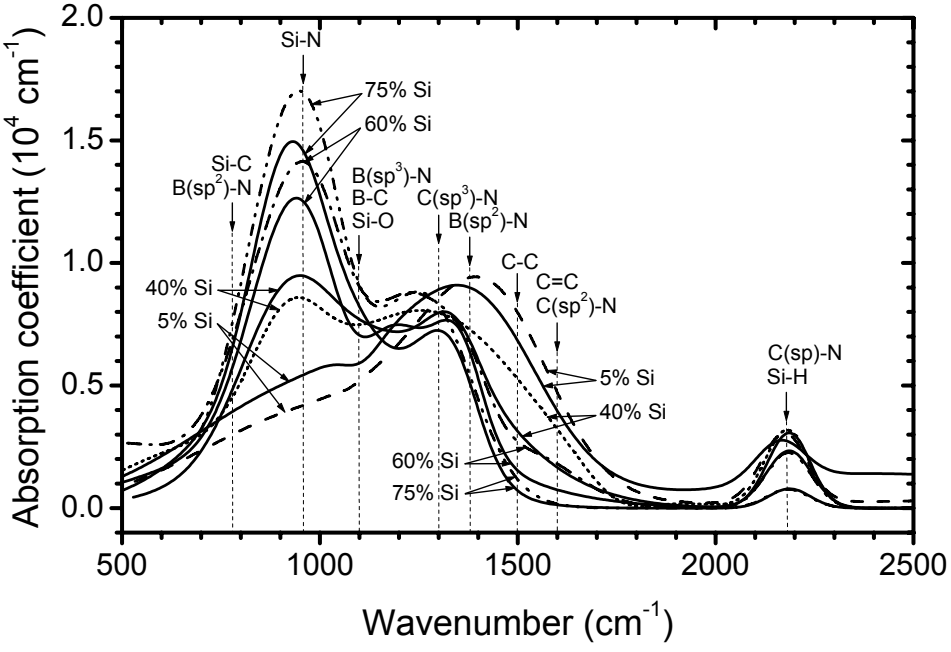

***Fig. 3.4**: The dependence of the absorption coefficient on wavelength in the infrared region, obtained by IR VASE for films prepared in a 50 % N_2 +50 % Ar gas mixture at various silicon fractions in the erosion target area (corresponding to the 5-75% Si labels on the curves) for U_b = -500 V and T_s = 350 °C (solid lines), and $U_s = U_f$ = -15 to -38 V and T_s = 180-190 °C (dashed lines).*

the combination of absorptions from Si-C (780 cm^{-1})[11], B(sp^2)-N (780 cm^{-1})[15] and a number of other bonds which have not been marked on the Figure 3.4, including vibrations of Si-Si bonds in the substrate at 610 cm^{-1}, deformation of B-O-Si bonds at 670 cm^{-1}, bending of B-O-B bonds at 720 cm^{-1}, bending of Si-O-Si bonds at 810 cm^{-1}, stretching of B-O-Si bonds at 930 cm^{-1} and vibrations of a B-B network at 942 cm^{-1} [16,17].

Figure 3.5 presents the results obtained for hardness, effective Young's modulus and elastic recovery of the films. The figure shows that the replacement of carbon by silicon in the films has significantly different effects depending on the substrate bias and temperatures used in the deposition process. The values of hardness (24–27 GPa), effective Young's modulus (170–180 GPa) and elastic recovery (72–73 %) for films made with U_b = -500 V and T_s = 350 °C are not substantially affected by the replacement of carbon by silicon. In contrast, replacement of carbon by silicon is accompanied by a strong increase in hardness (from 17 to 33 GPa with a maximum load of 30 mN), effective Young's modulus (from 135 to 216 GPa) and a slower rise in elastic recovery (from 65 to 73 %) for samples made with $U_s = U_f$ = - 15 to - 38 V and T_s = 180–190 °C.

As can be seen in Fig. 3.5(a), ion bombardment effects and thermal desorption lead to an enhanced hardness of the films with high carbon content. This is believed to be due to the

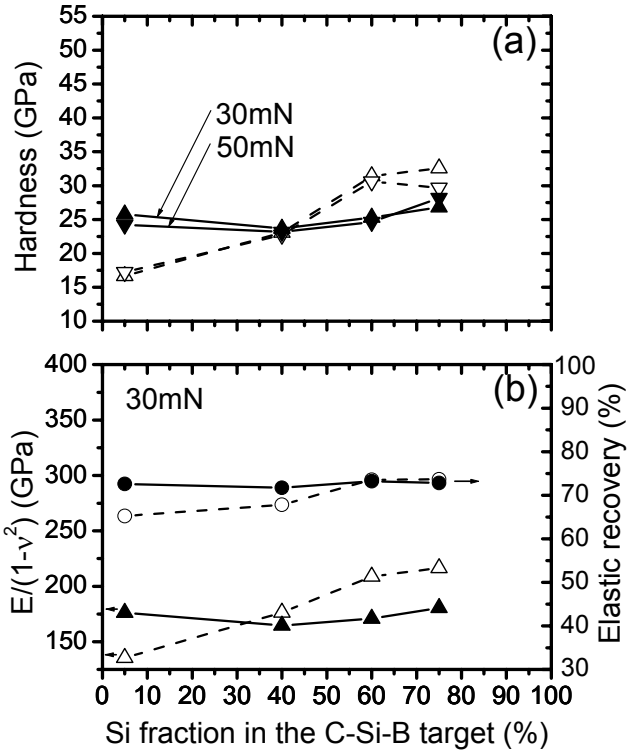

Fig. 3.5: *Hardness measured with the presented maximum load (a), and effective Young's modulus, $E/(1 - \nu^2)$, and elastic recovery measured with a maximum load of 30 mN (b) for films prepared in a 50 % N_2 + 50 % Ar gas mixture at various silicon fractions in the erosion target area for U_b = -500 V and T_s = 350 °C (full symbols), and $U_s = U_f$ = -15 to -38 V and T_s = 180 - 190 °C (empty symbols).*

removal of volatile C–N compounds from the growing film surface[3]. In contrast, for films with high silicon content conditions of energetic ion bombardment and elevated temperature cause a lower hardness. The ion kinetic energy may be too high to form an optimized superhard densified structure of the deposited material with highly coordinated B(sp^3)–N and C(sp^3)–N bonds[3,18,19].

3.3.2 Effect of the gas composition

As can be seen in Fig. 3.6(a), the Si content in the films increases (from 23 to 30 at. % for U_b = -500 V and from 24 to 29 at. % for U_b = -100 V) with increasing argon fraction in the gas mixture due to the enhanced physical sputtering of silicon from the composite target. A chemical affinity for nitrogen of silicon in the deposited material leads to an only a weak decrease (from 53 to 44 at. % for U_b = -500 V and from 51 to 44 at. % for U_b = -100 V) in the N content in the films in spite of the substantial decrease (4 times) in the N_2 partial pressure in the discharge gas. The content of boron in the films is practically constant (7–8 at. %) for U_b = -500 V and slowly decreases (from 11 to 6 at. %) for U_b = -100 V, while that of carbon is in the range from 5 to 9 at. % and 5 to 13 at. %, respectively. Much stronger ion-induced effects at U_b = -500 V result in a systematically lower (typically by 2 at. %) incorporation of both these elements into the films except for boron at a 75 % Ar fraction in the gas mixture when a dynamic balance determining the film composition was noticeably changed [see the enlarged C content and Fig. 3.6(b)].

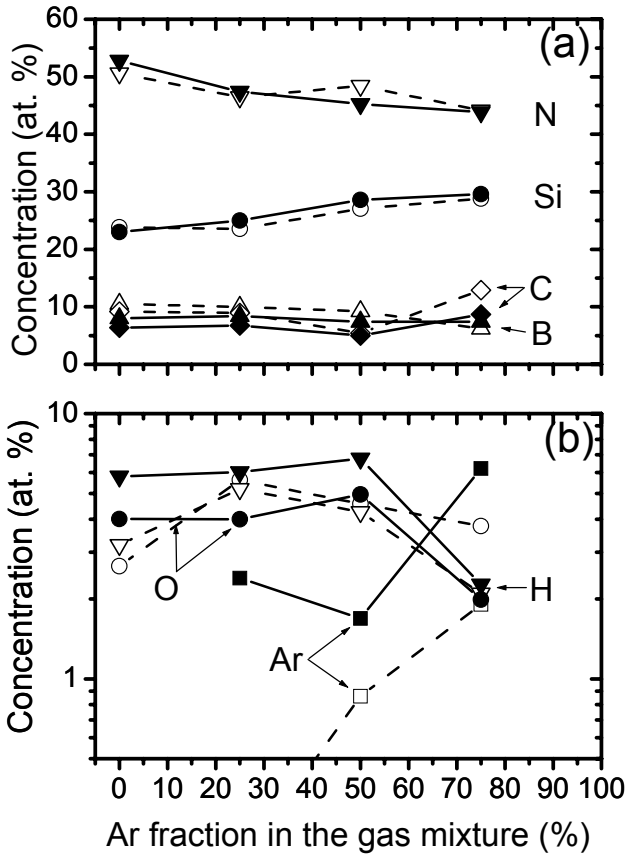

Fig. 3.6: *Elemental composition of films prepared at various argon fractions in the gas mixture, a fixed 60 % Si + 20 % B + 20 % C erosion target area and T_s = 350 °C for U_b = -500 V (full symbols) and U_b = -100 V (empty symbols).*

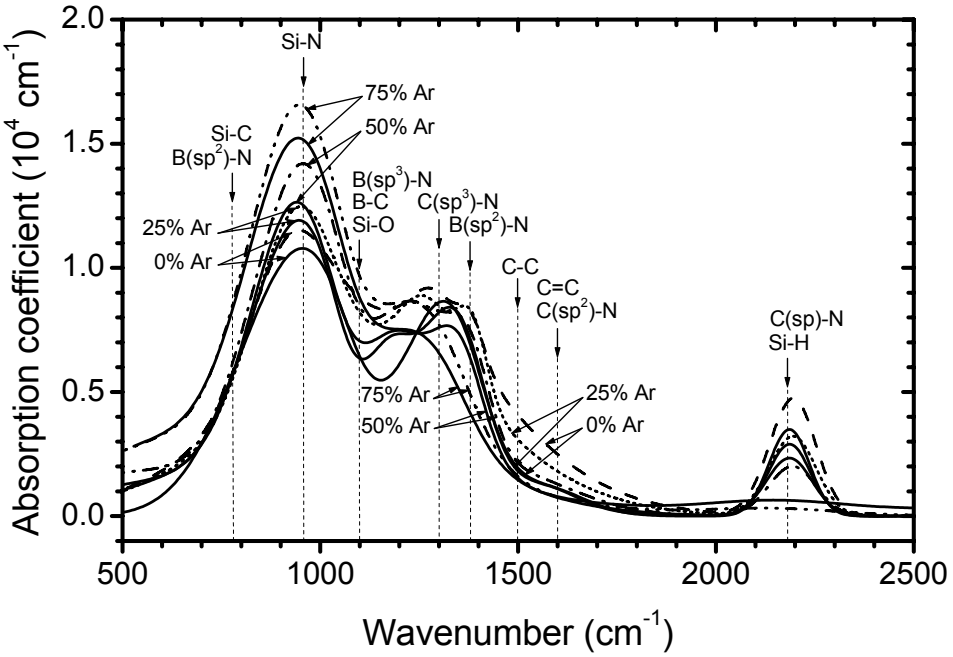

Fig. 3.7: *The dependence of the absorption coefficient on wavelength in the infrared region, obtained by IR VASE for films prepared at various argon ractions in the gas mixture (corresponding to the 0-75 % Ar labels on the curves), a fixed 60 % Si + 20 % B + 20 % C erosion target area and T_s = 350 °C for U = -500 V (solid lines) and U = -100 V (dashed lines).*

Fig. 3.6(b) shows the incorporation of argon and residual gas elements in the films. It appears that an intensified bombardment of the growing films by Ar^+ ions leads to subplantation of argon atoms into the films (up to 6 at. % for U_b = -500 V and 2 at. % for U_b = -100 V). As a result of the stronger bombardment by argon ions which leads to much higher deposition rates, the volume concentrations of hydrogen and oxygen in the films decrease to only 2 at. % for both the U_b values and at the 75 % Ar fraction in the discharge gas.

Figure 3.7 shows the influence of the N_2-Ar gas composition on the chemical bonding in the Si-B-C-N films as measured by IR VASE. There is a strong increase in the Si-N absorption as a natural consequence of increasing Si content in films (see Fig. 3.6). The affinity of Si for N leads to an increase in the number of Si-N bonds in spite of a reduction in the N content in the gas. The decreased N content reduces the number of C(sp^2)-N, B(sp^2)-N and C(sp)-N bonds, which may be responsible for hardness increase [see Fig. 3.8(a)]. In the case of 75 % Ar in the gas mixture it appears only absorption peak due to a presence of Si-N bond and its tail in the range of 1100-1300 cm^{-1}. Although exact positions of local maxima in the spectra may be affected by the shoulder of the dominant Si-N peak, in these compositions the tail most likely corresponds to bonds with C(sp^3) and B(sp^3). Absorption due to presence of bonds of C with C and N in the range of 1500-1600 cm^{-1} is much stronger in case of deposition with low Ar concentration in the gas mixture for U_b = -100 V as compared to U_b = -500 V. We believe that this is caused by lower desorption of volatile C-N compounds from the growing film surface[8] at lower biases (see twice higher C concentration in films in Fig. 3.6).

There is a stronger absorption peak corresponding to the B(sp^2)-N bond at 1385 cm^{-1} for U_b = -100 V than for Ub = -500 V in the case of both 0 and 25 % Ar concentration in the gas mixture. This shows that B has a similar behavior to C in that it is preferentially removed from the growing film under high bias conditions (see higher B and C concentrations in films for lower bias voltage in Fig. 3.6).

In the case of 75 % Ar in the gas mixture there is a difference in the level B and C incorporation into films due to the increased Si content (see surprising increase of C content in films for both U_b = -100 V and Ub =-500 V). The silicon preferentially bonds to the carbon because of the stronger Si-C bond compared to the Si-B bond[16].

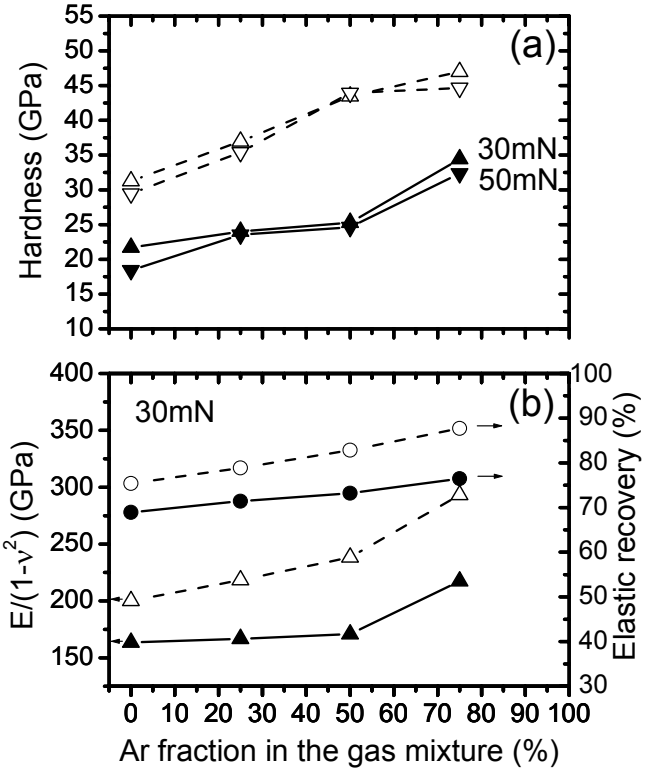

Fig. 3.8: *Hardness measured with the presented maximum load (a), and effective Young's modulus, $E/(1 - \nu^2)$, and elastic recovery measured with a maximum load of 30 mN (b) for films prepared at various argon fractions in the gas mixture, a fixed 60 % Si + 20 % B + 20 % C erosion target area and T_s = 350 °C for U_b = -500 V (full symbols) and U_b = -100 V (empty symbols).*

Figure 3.8 shows that an increasing argon fraction in the gas mixture leads to a progressive rise in hardness, effective Young's modulus and elastic recovery of the films for both the U_b values considered. However, the values obtained for these quantities at U_b = -100 V are systematically higher (hardness up to 47 GPa, the effective Young's modulus up to 290 GPa and the elastic recovery up to 88 % measured with a maximum load of 30 mN).

Taking into account the respective increase in the fraction of Ar^+ ions in the total ion flux onto growing films at a fixed U_b value, the rising film hardness (and hence the effective Young's modulus) can be explained by ion-induced knock-on subplantation of film-forming particles and by direct subplantation of argon into the films [see Fig. 3.6(b)], which results in densification of the deposited materials[20,21]. In previous work on sputter-deposited C–N[8,22] and Si–C–N[23] films indicated that increased hardness was correlated with enhanced ion-induced desorption of loosely bonded C–N species from the surface of growing films and with a decreased residual concentration of hydrogen [see Fig. 3.6(b)]. In the case of our amorphous Si–B–C–N materials the formation of hard, densified (density around 2.4 g cm^{-3}) films correlated with the use of the negative substrate bias voltage U_b = -100 V with the corresponding low values of the Γ_i/Γ_p flux ratio were found to be almost optimum for formation of hard densified amorphous Si–B–C–N materials (density around 2.4 g cm^{-3}) with strong local covalent bonds under the experimental conditions investigated[18] Detailed discussion of the effect of substrate bias on film characteristics is given in the chapter 4.

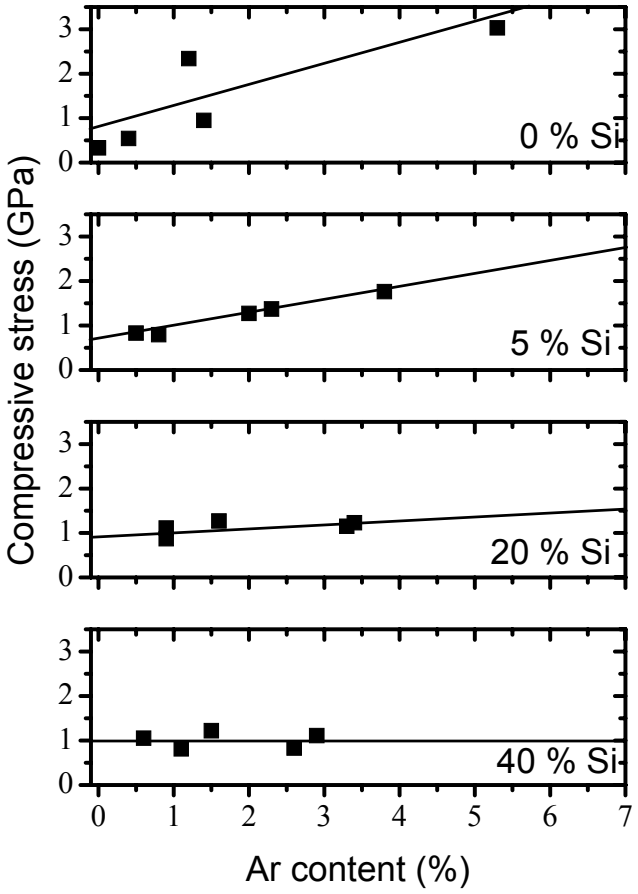

***Fig. 3.9**: Experimental compressive stresses in Si-B-C-N films as a function Ar and Si content. The figure shows that the linear dependence of stress and Ar content decreases with an increase in the Si content. Samples are prepared as described in the text. Not shown are the results for samples with 60 and 75 % Si content in the B_4C target, which, like the 40 % samples, did not exhibit any correlation of stress and Ar content.*

3.3.3 Effect of Si- and Ar-content on compressive stress

Figure 3.9 shows the compressive stress measured in the Si-B-C-N samples as a function of Si and Ar content. We note that the elemental analysis confirmed that the percentage of Si in the films increases with the ratio of Si in the sputtered target (see Fig. 3.3). The results show that for samples with low Si content, there exists a linear dependence between the amount of implanted Ar and the compressive stress in the films. For the samples with higher Si content, the correlation between Ar content and compressive stress is less clear. In case of the 20% Si targets there appears to be a weak correlation while there is no observable dependence for the 40, 60 and 75% Si targets. Collectively, the data shows that an increase in Si content results in a decrease in the dependence of compressive stress on Ar content. These results suggest that implanted Ar is a source of compressive stress in Si-B-C-N films with low Si content, while in high Si content samples, stress generation through implanted Ar appears to be inhibited. The phenomena shown are discussed in detail by means of computer simulations in chapter 7.

It is postulated that the low values (close to 1 GPa) of compressive stress in the films deposited with high silicon content and low Γ_i/Γ_p values[18] are due to the ability of silicon to form very easy distorted bonds with minimal energy penalty and the relatively low levels of ion bombardment during growth in agreement with Ref. 9. In addition, practically no correlation between the compressive stress and film hardness was observed except for the films prepared in a 25 % N_2 + 75 % Ar gas mixture, for which a slightly higher compressive stress rising from 1.2 GPa (U_b = -500 V) to 1.6 GPa (U_b = -100 V) was obtained in a qualitative agreement with theoretical predictions[18,20,24].

3.4 Conclusions

Reactive dc magnetron co-sputtering using a composite C–Si–B target in a nitrogen-argon gas mixture at substrate temperatures of 180–350 °C has proved to be a suitable technique for the deposition of new quaternary Si–B–C–N materials with outstanding physical properties. In particular, the Si–B–C–N films deposited in this way exhibit high hardness (up to 47 GPa) and elastic recovery (up to 88 %) at a low compressive stress (1.0–1.6 GPa).

Our results suggest that not only the composition of the C–Si–B target and the N_2–Ar gas mixture, but also substrate bias-related ion bombardment characteristics (particularly ion kinetic energy and ion-to-film-forming particles flux ratio) are important deposition parameters making it possible to control elemental composition, chemical bonding and the properties of the films formed over a wide range. These phenomena are discussed further in chapter 4 where the effect of bias is explored in detail.

Most significant chemical bonds in materials were found to be bonds of Si, B and C with N [Si-N, B(sp^{2-3})-N and C(sp^{1-3})-N] in all compositions studied, and C-C and C=C bonds mainly at high carbon content, at a presence of Si-C, Si-O and Si-H bonds.

We have shown a correlation of stress in Si-B-C-N films prepared by sputtering in nitrogen-argon mixture with the content of argon in the film. The strength of the correlation decreases steadily with increasing silicon content. This suggests the ability of silicon to relieve compressive stress, generated by implanted argon, in the Si-B-C-N films.

3.5 References

[1] J. Vlček, S. Potocký, J. Čížek, J. Houška, M. Kormunda, P. Zeman, V. Peřina, J. Zemek, Y. Setsuhara and S. Konuma, J. Vac. Sci. Technol. A **23**, 1513 (2005)

[2] J. Čížek, J. Vlček, L. Martinů, A. Amassian, Š. Potocký, J. Houška and Z. Soukup, prepared for publication in Thin Solid Films.

[3] S. Ulrich, T. Theel, J. Schwan and H. Ehrhardt, Surf. Coat. Technol. **97**, 45 (1997).

[4] S. Vepřek, J. Vac. Sci. Technol. A **17**, 2401 (1999).

[5] J. Musil, H. Zeman, F. Kunc and J. Vlček, Mater. Sci. Eng. A **340**, 281 (2003).

[6] D. Hegemann, R. Riedel and C. Oehr, Chem. Vap. Deposition **5**, 61 (1999).

[7] J. Vlček, M. Kormunda, J. Čížek, Z. Soukup, V. Peřina and J. Zemek, Diamond Relat. Mater. **12**, 1287 (2003).

[8] J. Vlček, K. Rusňák, V. Hájek and L. Martinů, J. Appl. Phys. **86**, 3646 (1999).

[9] D. Hegemann, C. Oehr and R. Riedel, 14th Internat. Symp. Plasma Chemistry, Symp. Proceedings (Ed.: M. Hrabovský, M. Konrád and V. Kopecký), Vol. III, Prague (Czech Republic), 1999, p. 1573.

[10] M. Konuma, Film Deposition by Plasma Techniques (Springer, Berlin, 1992).

[11] Y. Gao, J. Wei, D. H. Zhang, Z. Q. Mo, P. Hing and X. Shi, Thin Solid Films **377**, 562 (2000).

[12] M. Jelínek, J. Zemek, M. Trchová, V. Vorlíček, J. Lančok, R. Tomov and M. Šimečková, Thin Solid Films **366**, 69 (2000).

[13] Z. Zhou, I. Bello, M. Lei, K. Li, C. Lee and S. Lee, Surf. Coat. Technol. **128**, 334 (2000)

[14] A. Wrobel, A. Walkiewicz-Pietrzykowska, J. Klemberg-Sapieha, Y. Hatanaka, T. Aouki and Y. Nakanishi, J. Appl. Polym. Sci. **86**, 1445 (2002).

[15] A. Lousa, J. Esteve, S. Muhl and E. Martínez, Diamond Relat. Mater. **9**, 502 (2000).

[16] G.-R. Yang, Y.-P. Zhao and B. Y. Tong, J. Vac. Sci. Technol. A **16**, 2267 (1998).

[17] S.-D. Hwang and K. Yang, P. A. D. et al., Appl. Phys. Lett. **70**, 1028 (1997).

[18] J. Houška, J. Vlček, Š. Potocký and V. Peřina, accepted for publication in Diamond Relat. Mater. (2006).

[19] Y. Panayiotatos, S. Logothetidis, M. Handrea and W. Kautek, Diamond Relat. Mater. **12**, 1151 (2003).

[20] C. A. Davis, Thin Solid Films **226**, 30 (1993).

[21] J. Robertson, Diamond Relat. Mater. **3**, 361 (1994).

[22] V. Hájek, K. Rusňák, J. Vlček, L. Martinů and S. C. Gujrathi, J. Vac. Sci. Technol. A **17**, 899 (1999).

[23] J. Vlček, M. Kormunda, J. Čížek, V. Peřina and J. Zemek, Surf. Coat. Technol. **160**, 74 (2002).

[24] M. M. M. Bilek, D. R. McKenzie and W. Moeller, Surf. Coat. Technol. **186**, 21 (2004).

4 Influence of substrate bias voltage on structure and properties of Si-B-C-N films prepared by reactive magnetron sputtering

This chapter is based on results published in Ref. 1. It reports on the effect of the rf induced negative substrate bias voltage, U_b, on characteristics of the Si-B-C-N films (elemental composition, surface bonding structure, and mechanical and electrical properties) at several sputtered target and gas mixture compositions (selected on the basis of results included in the previous chapter).

In this chapter we systematically study the influence of an rf induced negative substrate bias on the reactive dc magnetron deposition of Si-B-C-N films using a co-sputtering of silicon, boron and carbon from a single composite target in nitrogen-argon gas mixtures. The influence of the C-Si-B target composition and the discharge gas mixture on the structure and mechanical properties of the films were investigated in the previous chapter. The films were found to be amorphous with a very smooth surface ($R_a \leq 0.8$ nm) and good adhesion to substrates with a low compressive stress (1.0 - 1.6 GPa). They exhibited high hardness (up to 47 GPa) and high elastic recovery (up to 88 %). They also found to have extremely high oxidation resistance in air at elevated temperatures (up to 1350 °C – the limit imposed by the substrate). Here we report on the effect of the negative substrate bias voltage on the discharge and deposition characteristics, and on elemental composition, surface bonding structure, and mechanical and electrical properties of the films prepared using C-Si-B and B_4C-Si composite targets at various substrate temperatures (≤ 350 °C). In addition, the low values of the internal stresses generated in the films will be presented and discussed.

4.1 Experimental conditions

The effect of the negative substrate bias voltage on the discharge and deposition characteristics, and on characteristics of the Si-B-C-N films is presented for films deposited using two different composite sputtering targets (C-Si-B sputter target with fixed 20% C + 60% Si + 20% B erosion area and B_4C-Si target with a fixed 40% B_4C + 60% Si erosion area). The two different composite targets with the same 60% Si fraction in the erosion area were used at a fixed 25% N_2 + 75% Ar gas mixture and T_s = 350 °C to investigate the influence of the changed target composition leading to noticeably different boron and carbon contents in films (Figs. 4.2, 4.4 and 4.7).

Two different substrate temperatures, T_s = 180-250 °C and T_s = 350 °C, were used to investigate the role played by thermally activated processes during film growth in a 50% N_2 + 50% Ar gas mixture (Figs. 4.1, 4.3, 4.5 and 4.6). Note that the relatively large (50-75%) fractions of silicon in the C-Si-B target erosion area and relatively high concentrations of argon in the N_2-Ar gas mixture, were found to be optimum for the production of hard and highly elastic Si-B-C-N films with very high oxidation resistance (see Refs. 2 and 3 and chapter 3).

Evolution of the compressive stress generated in films under various experimental conditions is shown in Figs. 4.6-4.9. Fig. 4.10 provides information on a possibility to control electrical conductivity of the Si-B-C-N films with a high carbon content by means of the negative substrate bias voltage.

4.2 Results

4.2.1 Discharge and deposition characteristics

Figures 4.1 and 4.2 show the influence of substrate bias on discharge and deposition characteristics in the case of sputtering of Si-B-C-N materials (for details on their evaluation see chapter 2, section 2.1.2). The discharge characteristics are observed for (1) the dc discharge near the sputtered target (absorbed power P_{dc} and sputtering current I_m), and (2) the rf discharge jnear the substrate holder (absorbed time-average power P_{rf} and substrate bias voltage U_b).

Figs. 4.1(a) and 4.2(a) show that at higher $|U_b|$ values, resulting in an increased P_{rf} power, the P_{dc} power decreases (as a consequence of the decreased U_{dc} voltage applied to keep a constant value of I_m = 1 A) due to a mutual coupling between both discharges. The corresponding P_{dc} and P_{rf} values are systematically higher for a 25% N_2 + 75% Ar gas mixture (Fig. 4.2(a)). The main reason for this is an increased plasma impedance leading to a higher P_{dc} power[2,4]. The higher (75%) fraction of argon in the discharge gas, together with the related increased P_{dc} value, resulted in a progressive rise in the deposition rate of the films due to more effective physical sputtering of both composite targets with a 60% silicon fraction in the

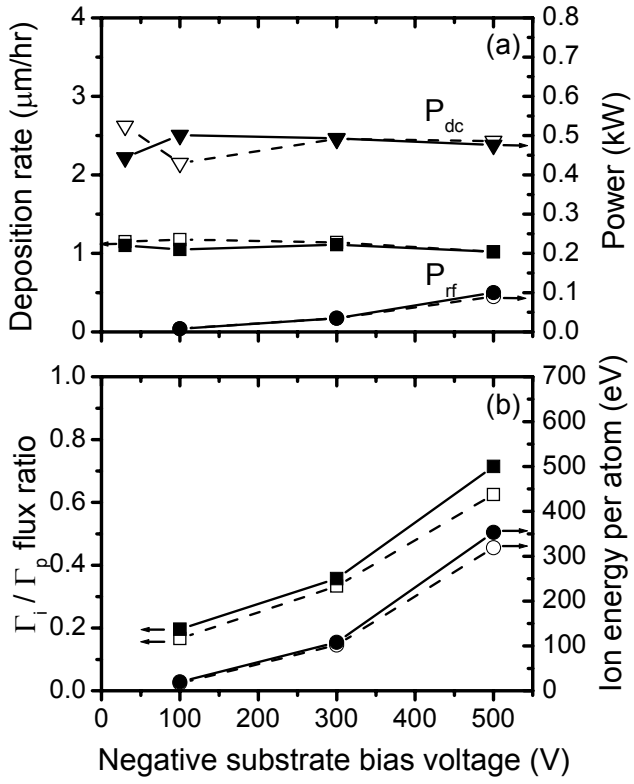

***Fig. 4.1**: Discharge and deposition characteristics of films prepared using a C-Si-B (20:60:20 %) target at various negative substrate bias voltages in a 50% N_2 + 50% Ar gas mixture for T_s = 350 °C (full symbols) or T_s = 180-250°C (empty symbols). Panel (a) shows deposition rate and powers, P_{dc} and P_{rf}, absorbed in the discharge. Panel (b) shows ions to film-forming particles flux ratio, Γ_i/Γ_p, and energy delivered by ions into growing films per one film atom.*

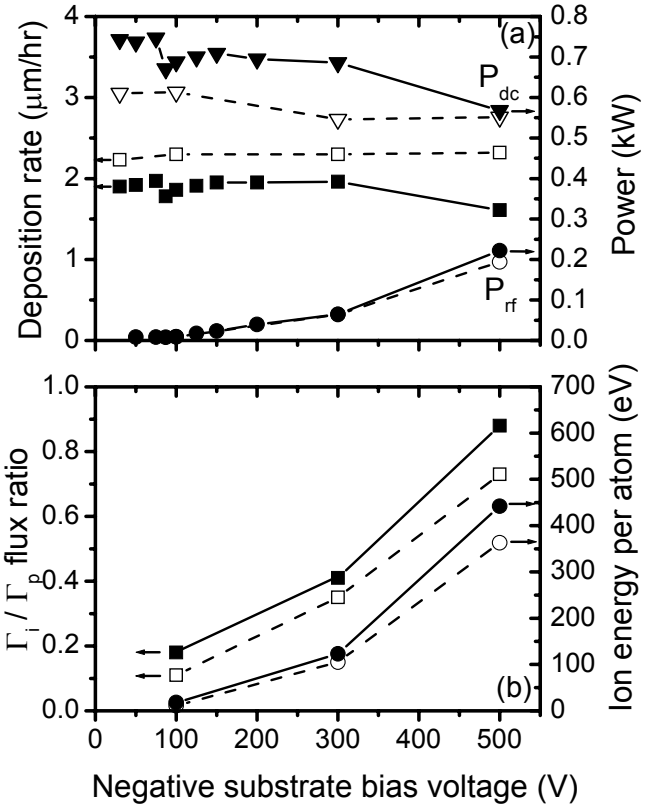

***Fig. 4.2**: Discharge and deposition characteristics of films prepared using a C-Si-B (20:60:20 %) target (full symbols) or B_4C-Si (40:60 %) target (empty symbols) at various negative substrate bias voltages in a 25% N_2 + 75% Ar gas mixture for T_s = 350 °C.*

erosion area. In the case of the B_4C-Si target the measured deposition rates are even systematically higher in spite of lower P_{dc} powers. This is mainly caused by a higher total sputtering yield and secondary electronic emission coefficient of the sputtered material[5]. As is seen in Fig. 4.1(a), a higher substrate temperature T_s = 350 °C leads to a small decrease of the deposition rate at lower $|U_b|$ values. This can be explained by a thermal desorption of loosely bonded species from the growing film surface.

If it is assumed that (1) the deposition rate is proportional to the flux of film-forming particles onto the substrate, Γ_p, at relatively small changes in atomic density of the films, and (2) the P_{rf} power is proportional to the respective total time-average ion flux, Γ_i, then it is possible to explain the effect of the negative substrate bias voltage on the Γ_i/Γ_p flux ratio and the ion energy per deposited atom, E_{ia}, presented in Figs. 4.1(b) and 4.2(b). It is shown that the low values of these quantities ($\Gamma_i/\Gamma_p \leq 0.2$ and $E_{ia} \leq 20$ eV) at $|U_b| \leq 100$ V rapidly increase for $|U_b| > 100$ V. This rise is very important for evolution of the film characteristics which will be discussed later (see, for example, stress relaxation in films, homogenization of the formed material and changes in its bonding structure, leading to a lower film hardness, or an increased Ar content and decreased H content in the films affecting their electrical conductivity).

The values of $\Gamma_i/\Gamma_p \leq 0.9$, applied in this work, are very low compared with Ref. 6 which reporting on the use of intense ion bombardment with the Γ_i/Γ_p flux ratio up to 66 in magnetron sputtering of superhard materials (such as cubic boron nitride, tetrahedral amorphous carbon, boron carbide and cubic silicon carbide) with a high compressive stress (occasionally higher than 10 GPa). Because the ions are formed mainly in the dc magnetron discharge with a power P_{dc} (because $P_{dc} >> P_{rf}$ at low $|U_b|$ and $P_{dc} > P_{rf}$ at high $|U_b|$ - see Figs. 4.1(a) and 4.2(a)) being practically independent of the area of the unshielded substrate holder, A_s, the low Γ_i/Γ_p values can be explained by the corresponding low ion fluxes Γ_i due to the large value of $A_s = 620$ cm^2.

4.2.2 Elemental composition and surface bonding structure

Figs. 4.3 and 4.4 present the effect of the negative substrate bias voltage on the elemental composition of Si-B-C-N films with low contents of argon, hydrogen and oxygen. Overall the influence of U_b on the elemental composition of films is relatively weak. Notable exceptions are the film prepared in a 50% N_2 + 50% Ar gas mixture at $U_s = U_f = -38$ V and T_s = 180-190 °C when ion-induced and thermal desorption of loosely bonded C-N species from the surface of growing films are significantly reduced (Fig. 4.3), and the film with an enlarged 13 at.% carbon content[2] prepared using a C-Si-B target in a 25% N_2 + 75% Ar gas mixture at $U_b = -100$ V and $T_s = 350$ °C (Fig. 4.4). The level of implanted Ar (see Fig. 4.4(b)) in the films does seem to depend on the substrate bias. Increasing substrate bias promotes the direct

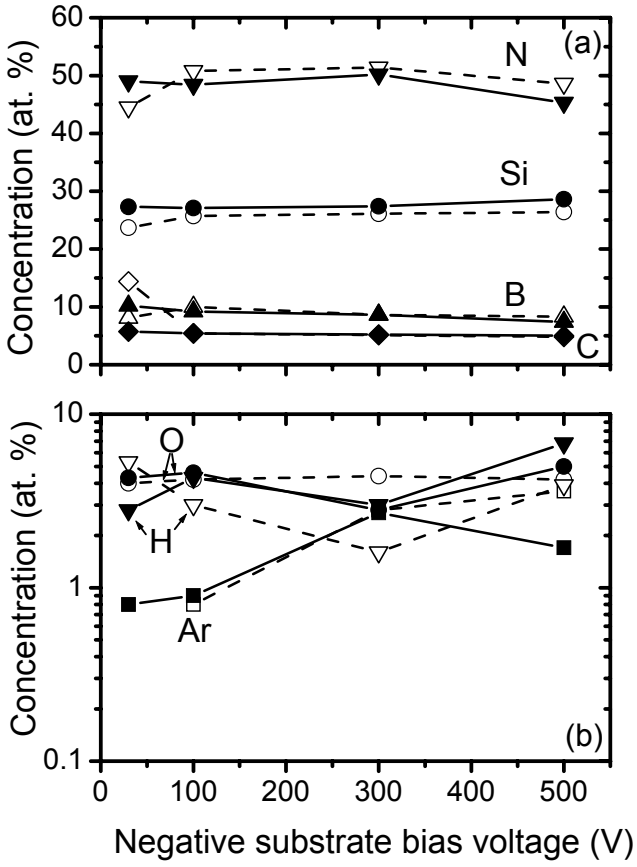

***Fig. 4.3**: Elemental composition of films prepared using a C-Si-B (20:60:20 %) target at various negative substrate bias voltages in a 50% N_2 + 50% Ar gas mixture for T_s = 350 °C (full symbols) or T_s = 180 - 250 °C (empty symbols).*

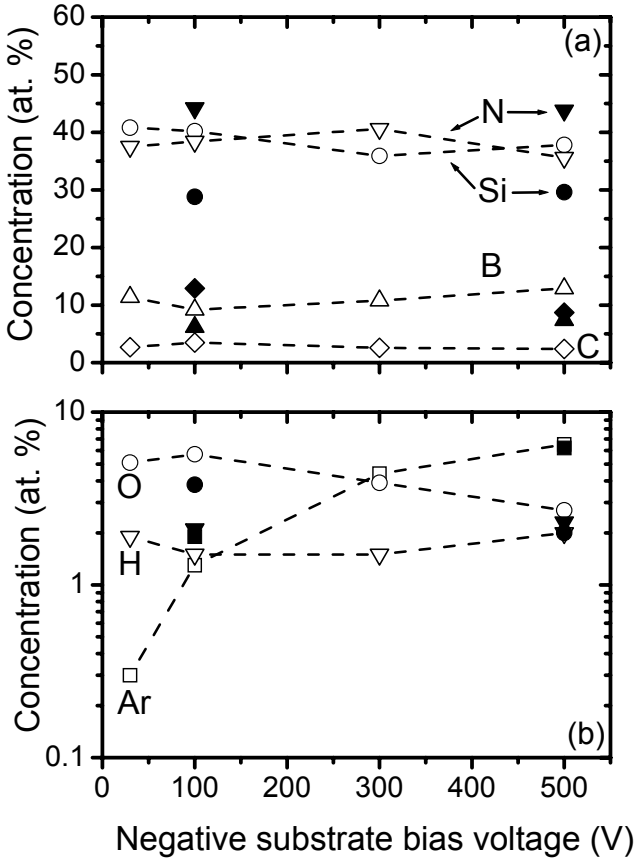

***Fig. 4.4**: Elemental composition of films prepared using a C-Si-B (20:60:20 %) target (full symbols) or B_4C-Si (40:60 %) target (empty symbols) at various negative substrate bias voltages in a 25% N_2 + 75% Ar gas mixture for T_s = 350 °C.*

implantation of Ar atoms (up to 7 at.% at the 75% Ar fraction in the discharge gas) into the films[4].

As is shown in Fig. 4.4, the use of a B_4C-Si target with a fixed 40% B_4C + 60% Si erosion area resulted in appreciable changes in the elemental composition of the Si-B-C-N films compared to the C-Si-B target with a 20% C + 60% Si + 20% B erosion area. The corresponding increase in the boron content in the films (by 3 at.% at U_b = -100 V and 6 at.% at U_b = -500 V) and decrease of the carbon content (by 9 and 6 at.%, respectively) were connected with a rise in the silicon content (by 11 and 8 at.%, respectively) and decrease of the nitrogen content (by 6 and 8 at.%, respectively) at a slightly increased oxygen content and almost the same contents of hydrogen (around 2 at.%) and argon (up to 7 at.%).

The infrared spectra of Fig. 4.5 show that the negative substrate bias voltage does not cause, except possibly for the boron bonding states, significant changes in the infrared absorption of the films (for peak identifications see chapter 3). Silicon is preferentially bonded to nitrogen and to carbon except for Si-O bonds formed at the surface due to oxidation in air. It has been found that the Si-C bonds were not reliably detectable by XPS in magnetron-sputtered hard amorphous Si-C-N films[4,5]. Their presence in the Si-B-C-N films could be explained by a partial occupation of nitrogen bonding states by boron, which forces

Si and C to a mutual bonding. The N-Si bond is the dominant N-containing bond with a lower occurrence of N-B and N-C bonds, while the C-C bond and C-N bond are the dominant bonds for carbon atoms, with minor proportions of C-B and C-Si.

Boron is preferentially bonded to nitrogen[7-10] with a lower occurrence of the B-C bonds. Relatively highest abundance of the B(sp^3)-N bonds can be observed in Fig. 4.5 for the films prepared at U_b = -100 V and T_s = 350 °C. This phenomenon, confirmed also by XPS[1] measurements, is in agreement with Ref. 11, reporting on existence of a window of ion energies for which B(sp^3)-N bonds dominate in sputtered amorphous BN films.

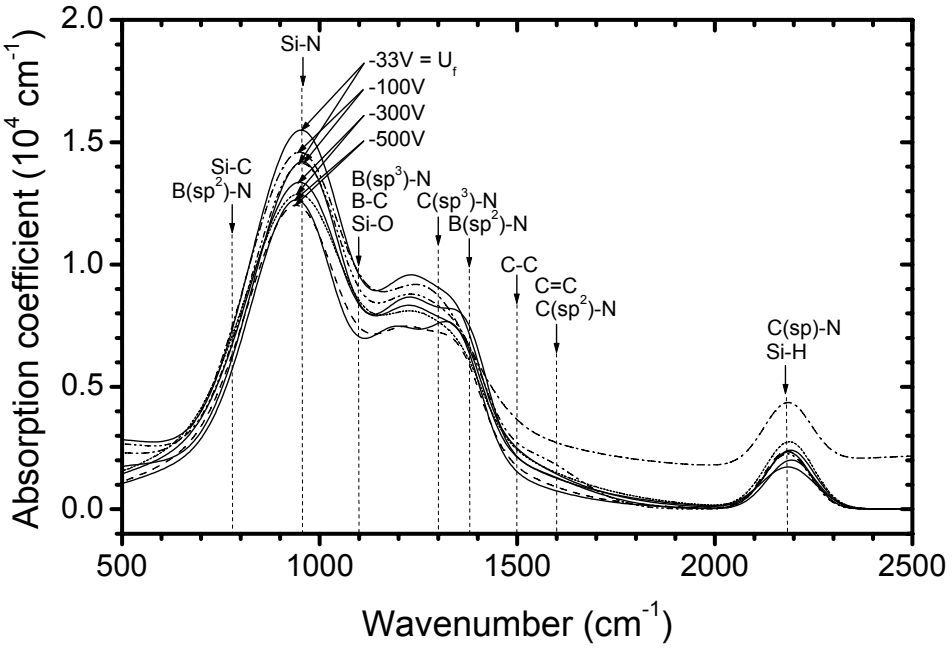

***Fig. 4.5**: The dependence of the absorption coefficient on wavelength in the infrared region, obtained by IR VASE for films prepared using a C-Si-B (20:60:20 %) target at various negative substrate bias voltages in a 50% N_2 + 50% Ar gas mixture for T_s = 350 °C (solid lines) or T_s = 180-250 °C (dashed lines).*

4.2.3 Mechanical properties

Figs. 4.6 and 4.7 present the effect of the negative substrate bias voltage on the mechanical properties of Si-B-C-N films. A negative substrate bias voltage of U_b = -100 V with the corresponding low values of $\Gamma_i/\Gamma_p \leq 0.2$ and $E_{ia} \leq 20$ eV (see Figs. 4.1(b) and 4.2(b)) was found to be almost optimum for formation of hard densified amorphous Si-B-C-N materials (density around 2.4 g/cm^3) with strong local covalent bonds. Fig. 4.6 shows that the values of all examined mechanical quantities (hardness, modified Young's modulus $E/(1-\nu^2)$ and elastic recovery) are substantially higher (44 GPa, 240 GPa and 82%, respectively) at U_b = -100 V for the increased substrate temperature T_s = 350 °C, probably due to a higher fraction of B(sp^3)-N and C(sp^3)-N bonds in the films[10]. Note that the level of intrinsic compressive stress is not strongly varying, hence the variations in the other properties are not the result of variations in the stress level. As is seen in Fig. 4.6(a), there is practically no

correlation between film hardness and low values (close to 1 GPa) of compressive stress in the films prepared in a 50% N_2 + 50% Ar gas mixture. However, an intensified bombardment of growing films by argon ions in a 25% N_2 + 75% Ar gas mixture resulted in U_b dependent values of the compressive stress with a maximum value of 1.8 GPa achieved at U_b = -125 V for the films prepared using the C-Si-B target (Fig. 4.7(a)). The values obtained for all the aforementioned mechanical quantities were systematically higher than those obtained with the corresponding B_4C-Si target.

Besides promoting the formation of the B(sp^3)-N and C(sp^3)-N bonds, another possible explanation of the observed effect of U_b in increasing film hardness, has been suggested by results of molecular-dynamics simulations[13]. Because the results are described in detail in chapters 7 and 8, here we only note that using a liquid-quench algorithm, which allows to simulate rapid (low $|U_b|$) and slow (high $|U_b|$) cooling of the localized melt formed around sites of energetic ion impact, two types of segregation leading to a higher extrinsic hardness of the Si-B-C-N films prepared at U_b = -100 V were predicted.

Hardness enhancements due to segregation of phases have been reported previously for binary mixtures of various amorphous and nanocrystalline phases[14]. The MD simulations

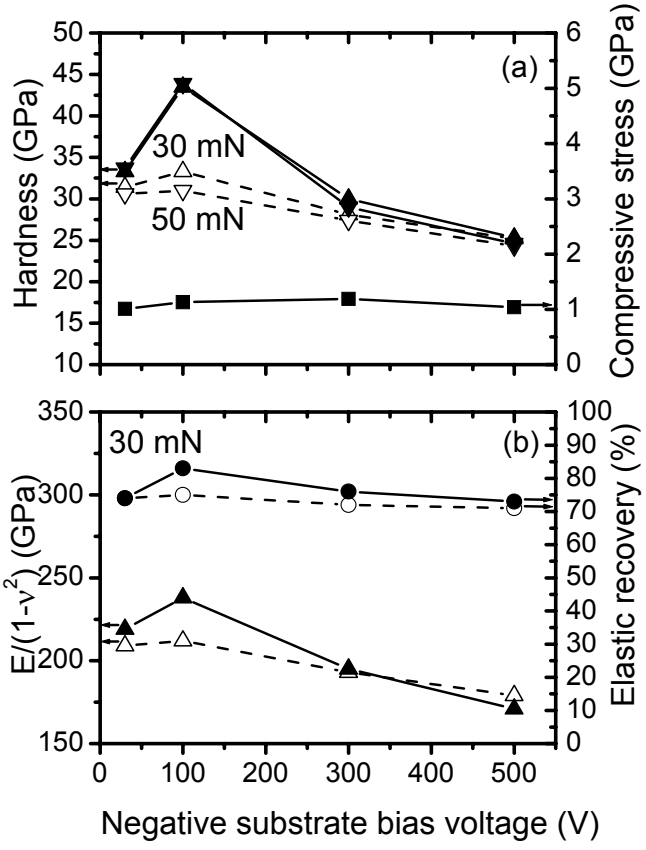

***Fig. 4.6**: Hardness measured with the presented maximum load and intrinsic compressive stress (a), and effective Young's modulus, $E/(1 - \nu^2)$, and elastic recovery measured with a maximum load of 30 mN (b) for films prepared using a C-Si-B (20:60:20 %) target at various negative substrate bias voltages in a 50% N_2 + 50% Ar gas mixture for T_s = 350 °C (full symbols) or T_s = 180 - 250 °C (empty symbols).*

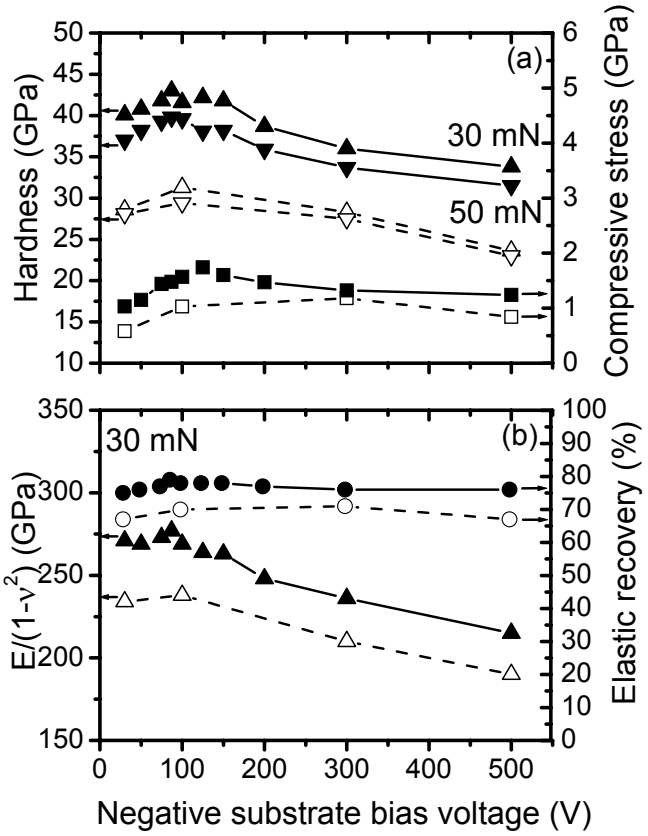

***Fig. 4.7**: Hardness measured with the presented maximum load and intrinsic compressive stress (a), and effective Young's modulus, $E/(1 - \nu^2)$, and elastic recovery measured with a maximum load of 30 mN (b) for films prepared using a C-Si-B (20:60:20 %) target (full symbols) or B_4C-Si (40:60 %) target (empty symbols) at various negative substrate bias voltages in a 25% N_2 + 75% Ar gas mixture for T_s = 350 °C.*

showed that small segregated regions, which occur as a result of random clustering in a melt were able to survive rapid cooling stage and become locked into the structure. The thermodynamically preferred structure, which has been found to be homogeneous, forms with slow cooling (high $|U_b|$). Another type of phase segregation observed is the formation of silicon-enriched zones around implanted argon atoms. While at high Ar content (around 6 at.%) for U_b = -500 V most of the network atoms are close to at least one Ar atom, which in fact leads to an almost homogeneous Si-B-C-N material, the occurrence of both Si-rich (close-to-Ar) and Si-poor (far-from-Ar) zones can be observed at a lower (1-2 at. %, see Figs. 4.3(b) and 4.4(b)) Ar content for U_b = -100 V. The energy advantage gained by surrounding Ar atoms with longer and more flexible Si-containing bonds was proposed to be a driving force for this segregation. This will be discussed in more detail in Chapters 7 (segregation around Ar) and 8.2 (its possible effect on hardness).

4.2.4 Compressive stress in the films

For films deposited above room temperature a component of the stress measured at room temperature is so called extrinsic stress, due to differences in thermal expansion coefficients of the film and the substrate. For our Si-B-C-N films we estimate this component to be

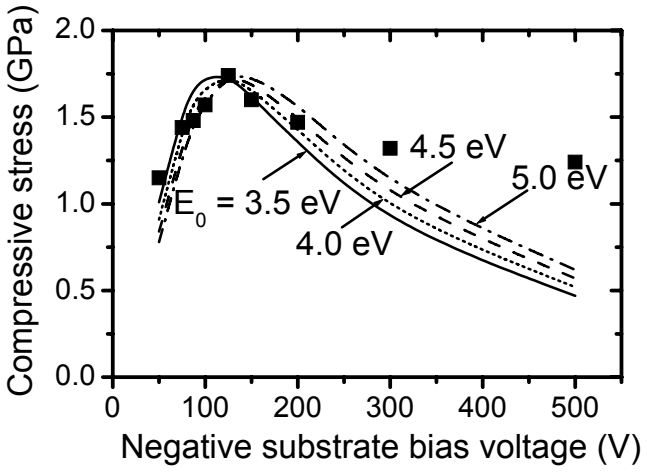

***Fig. 4.8**: Measured compressive stress of films prepared using a C-Si-B (20:60:20 %) target at various negative substrate bias voltages in a 25% N_2 + 75% Ar gas mixture for T_s = 350 °C (full squares), together with theoretical predictions based on the Davis's formula at various activation energies E_0.*

$$|\sigma_{CTE}| = |E(\alpha_f - \alpha_s)(T_s - T_r)| < 0.1 \text{ GPa} \qquad \text{(Eq. 4.1).}$$

using typical values of the coefficients of thermal expansion (CTE) in the relevant temperature range, $\alpha_f \approx 1.8\times10^{-6}$ K^{-1} (see Ref. 15) for the Si-B-C-N and $\alpha_s \approx 2.8\times10^{-6}$ K^{-1} for the silicon substrate and assuming that the films Young's modulus E < 300 GPa. This suggests that a major part of the measured film stress is caused by deposition conditions, particularly by ion bombardment of growing films.

The dependence of the compressive stress on the substrate bias voltage, U_b, was most pronounced for the films prepared using the C-Si-B target in a 25% N_2 + 75% Ar gas mixture (see Fig. 4.7(a)). We used a simple theoretical model developed by Davis[16] to compare with the results in Fig 4.8. The model captures the formation of the compressive stress $\sigma(E_i)$ by ion bombardment, considering a steady state in which the stress formation by knock-on implantation of film atoms due to bombarding ions is balanced by the ion-energy induced migration of the implanted atoms. The Davis model is given by the equation[16]

$$\sigma(E_i) = \frac{E}{1-\nu}\frac{c\sqrt{E_i}}{\Gamma_p/\Gamma_i + 0.016p(E_i/E_0)^{5/3}} \qquad \text{(Eq. 4.2),}$$

where E and ν are the Young's modulus and the Poisson's ratio of the material, respectively, c is a constant, E_0 is the activation energy for the relaxation process and p is a material parameter of the order of 1. We recall that this model was successfully used[6] for the mentioned superhard materials with a high compressive stress, produced by magnetron sputtering in a pure argon discharge, where the Ar^+ ion fluxes responsible for the stress formation in the films were relatively high in comparison with the deposition fluxes of film-forming particles (Γ_i/Γ_p up to 66).

In our calculations of $\sigma(E_i)$, presented in Fig. 4.8, the E/(1-ν) ratio has been replaced by the corresponding measured values of $E/(1-\nu^2)$, see Fig. 4.7(b), under a realistic assumption that 1+ν is approximately constant. The known values of Γ_i/Γ_p , see Fig. 4.2(b),

were used at the activation energy range from 3.5 to 5 eV and p = 1. As is seen in Fig. 4.8, the model of Davis describes the stress formation in the films only qualitatively in our case, when the Γ_i/Γ_p flux ratio is relatively low (≤ 0.9) and the ions of film-forming particles (such as N_2^+, N^+ and Si^+) form a significant part of the total ion flux onto the substrate, Γ_i, see Ref. 2. The phenomenon that the Davis model (which is empirical and therefore doesn't incorporate the physics of stress relief by ion energy) tends not to fit the falloff of stress seen as the ion energy is increased after the peak is discussed more closely in recent Ref. 12.

In addition to the low Γ_i/Γ_p values, a high Si content in materials produced using the C-Si-B and B_4C-Si targets with a 60% Si fraction in the erosion area (Figs. 4.3(a) and 4.4(a)) is another reason for low values ($\leq$ 1.8 GPa) of their compressive stress (Figs. 4.6(a) and 4.7(a)). This beneficial role of silicon in reducing the compressive stress has been already suggested at the end of chapter 3, and in Fig. 4.9 it is shown together with respective values of hardness for the Si-B-C-N films prepared in a 25% N_2 + 75% Ar gas mixture at U_b = -100 V and T_s = 350 °C using a B_4C-Si target with the Si fraction in the erosion area varied from 5 to 75%. As can be seen in Fig. 4.9(a), the increasing Si fraction in the target erosion area led to a rising incorporation of silicon (from 8 to 46 at.%) into the films. As a result, the film hardness rapidly increased to a saturated value of 32 GPa, while the corresponding compressive stress in the films successively decreased from 1.7 to 0.9 GPa (Fig. 4.9(b)).

The ability of silicon to reduce that part of the compressive stress which is generated by implanted Ar atoms has been explained in Ref. 13 - see chapter 7 for detailed discussion. Using liquid-quench molecular dynamics simulations, the aforementioned segregation of Si

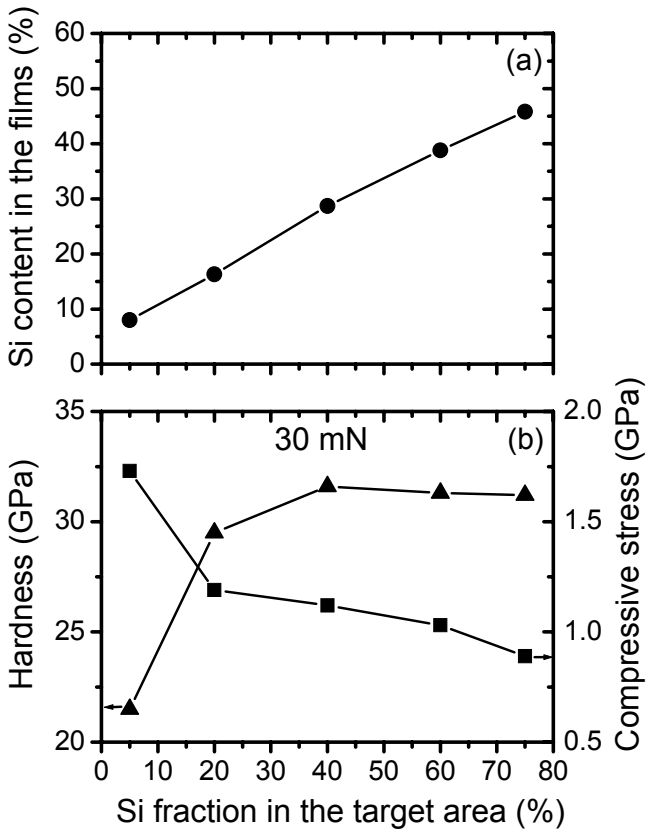

***Fig. 4.9**: Hardness and compressive stress correlated with the Si content in films prepared in a 25% N_2 + 75% Ar gas mixture at various Si fractions in the erosion area of the B_4C-Si target for U_b = -100 V and T_s = 350 °C.*

atoms around Ar-containing "cavities" during solidification of the material and increased preference of other atoms to bond with Si in vicinity of these cavities have been shown. The comparative flexibility of the long Si-containing bonds enables these bonds to deform to accommodate the argon atoms into the structure with a minimum generation of stress.

4.2.5 Electrical conductivity

Fig. 4.10 presents the results obtained for electrical resistivity of films prepared in two different N_2-Ar gas mixtures using a modified C-Si-B target with a high C fraction (75%) and low Si fraction (5%) in its erosion area. This modification allowed us to form semiconductive Si-B-C-N materials. Neglecting low contents of Ar, H and O in the films, their typical elemental composition can be characterized as $Si_{10}B_{12}C_{40}N_{38}$. As can be seen in Fig. 4.10, the electrical resistivity of the films prepared in a 50% N_2 + 50% Ar gas mixture rapidly decreases (almost 100 times in the range from $U_s = U_f$ to U_b = -700 V) with a rise in the $|U_b|$ values. This can be explained (1) by a decreasing occurrence of weakly bonded hydrogen atoms (inhibiting interconnections between other film atoms and thus decreasing the electrical conductivity of films[17]) in the film volume due to the ion bombardment, or (2) by turning of sp^3-rich structure into a sp^2-rich one (which is generally known to be more conductive). In this particular case, the first explanation is more probable because (1) the increase in conductivity starts immediately above floating voltage (i.e. not above some U_b threshold), and (2) at high carbon content the hardness (which is there likely to correlate with the sp^3/sp^2 ratio) is higher at higher $|U_b|$ of 500 V (see chapter 3, section 3.3.1).

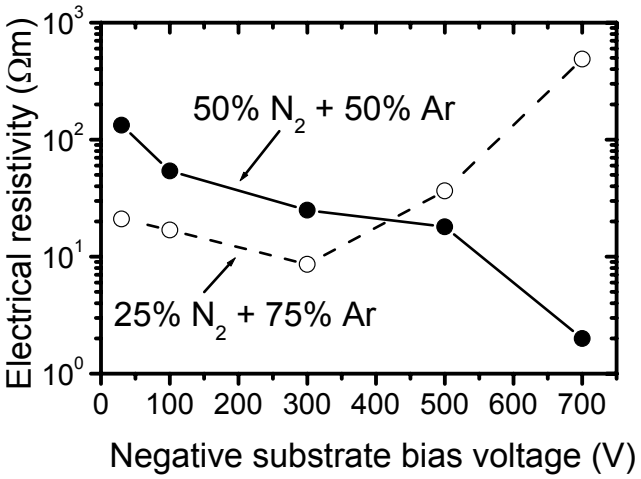

***Fig. 4.10**: Electrical resistivity of films prepared using a C-Si-B (75:5:20 %) target at various negative substrate bias voltages in a 50% N_2 + 50% Ar (full symbols) or 25% N_2 + 75% Ar (empty symbols) gas mixture for T_s = 350 °C.*

However, a different trend was observed for the films prepared in a 25% N_2 + 75% Ar gas mixture, for which electrical resistivity increased at $|U_b| > 300$ V. We believe that this behaviour is caused by a stronger Ar^+ ion bombardment leading to a higher content of implanted argon atoms in the films. As a result, a dense 3D structure of Si-B-C-N materials is replaced by a structure consisting of 2D-like zones around large (radius >2 Å) cavities including implanted Ar atoms[13]. This structural change of the Si-B-C-N network leads to a decrease in the electrical conductivity of films prepared at high $|U_b|$ values in N_2-Ar gas

mixtures with high Ar fractions, when an already low volume concentration of hydrogen in the films cannot be further reduced while the content of implanted argon steadily increases.

4.3 Conclusions

Novel quaternary Si-B-C-N films were fabricated using dc magnetron co-sputtering of silicon, boron and carbon from a single C-Si-B (20:60:20 % and 75:5:20 %) or B_4C-Si (40:60 %) target in nitrogen-argon (50:50 % and 25:75 %) gas mixtures at various rf induced negative substrate bias voltages (from floating potential to U_b = -700 V) and substrate temperatures T_s in the range 180-350 °C. The films, typically 2-5 μm thick, were found to be amorphous with a density around 2.4 g/cm^3 and good adhesion to substrates with a low compressive stress (0.6-1.8 GPa). It was shown that the negative substrate bias voltage U_b = -100 V with the corresponding low values of the ion-to-film-forming particles flux-ratio $\Gamma_i/\Gamma_p \leq 0.2$ and the ion energy per deposited atom $E_{ia} \leq 20$ eV are about optimum at T_s = 350 °C for the formation of hard (hardness up to 44 GPa) and highly elastic (elastic recovery up to 82 %) Si-B-C-N films with a high (27-40 at.%) silicon content, exhibiting extremely high oxidation resistance in air at elevated temperatures (up to the 1350 °C substrate limit), see our recent works[2,3]. A beneficial role of silicon in reducing the compressive stress in the films was observed. The electrical conductivity of the semiconductive Si-B-C-N films with a high (approximately 40 at.%) carbon content was controlled over a wide range (almost two orders of magnitude) by the nitrogen-argon gas mixture composition and the U_b values.

4.4 References

1 J. Houška, J. Vlček, Š. Potocký and V. Peřina, accepted for publication in Diamond Relat. Mater. (2006).

2 J. Vlček, Š. Potocký, J. Čížek, J. Houška, M. Kormunda, P. Zeman, V. Peřina, J. Zemek, Y. Setsuhara and S. Konuma, J. Vac. Sci. Technol. A **23**, 1513 (2005).

3 Š. Potocký, Ph.D. thesis, University of West Bohemia, Plzeň, Czech Republic, 2006.

4 J. Vlček, M. Kormunda, J. Čížek, V. Peřina and J. Zemek, Surf. Coat. Technol. **160**, 74 (2002).

5 J. Vlček, M. Kormunda, J. Čížek, V. Peřina and J. Zemek, Diamond Relat. Mater. **12**, 1287 (2003).

6 S. Ulrich, T. Theel, J. Schwan and H. Ehrhardt, Surf. Coat. Technol. **97**, 45 (1997).

7 H. Jüngermann , M. Jansen, Mat. Res. Innovat. **2**, 200 (1999).

8 Y.Cai , S. Prinz, A. Zimmermann, A. Zern, W. Sigle, M. Rühle and F. Aldinger, Scripta Materialia **47**, 7(2002).

9 A.Zern, J. Mayer, N. Janakiraman, M. Weinmann, J. Bill and M. Rühle, J. Eur. Ceram. Soc. **22**, 1951 (2002).

10 M.K. Lei, Q. Li, Z.F. Zhou, I. Bello, C.S. Lee and S.T. Lee, Thin Solid Films **389**, 194 (2001).

11 Y. Panayiotatos, S. Logothetidis, M. Handrea and W. Kautek, Diamond Relat. Mater. **12**, 1151 (2002).

12 M.M.M. Bilek and D.R. McKenzie, Surf. Coat. Technol. **200**, 4345 (2006).

13 J. Houška, O. Warschkow, M.M.M. Bilek, D.R. McKenzie, J. Vlček and Š. Potocký, J. Phys.: Condens. Matter **18**, 2337 (2006).

14 J. Musil, Surf. Coat. Technol. **125**, 322 (2000).

15 T.L. Dhami, O.P. Bahl and B.R. Awasthy, Carbon **33**, 479 (1995).

16 C.A. Davis, Thin Solid Films, **226**, 30 (1993).

17 V. Hájek, K. Rusňák, J. Vlček, L. Martinů and S.C. Gujrathi, J. Vac. Sci. Technol. A **17**, 899 (1999).

5 Formation of N_2 molecules in rapidly quenched amorphous materials

This chapter is based on results published in Ref. 1. It includes ab-initio molecular dynamics simulations of the preparation of CN_x, B-C-N and Si-B-C-N materials formed by energetic ion assisted deposition techniques. We focus on the formation of N_2 molecules during liquid quench simulations and investigate how density, temperature and quench rate affect the number of N_2 molecules formed in the network. We find that higher material density and shorter cooling times lead to reduced N_2 formation and thus higher nitrogen incorporation into the structure. These results suggest a modification of common physical vapour deposition (PVD) techniques to enhance N content in materials such as CN_x.

5.1 Introduction

The crystalline β-C_3N_4 phase, in which the carbon is tetrahedrally coordinated, promises high hardness. Thus, we would expect that amorphous CN_x materials with high N content (~ 57%) should incorporate tetrahedrally coordinated carbon and show similar properties. However, there appear to be clear limits to how much nitrogen can be incorporated in CN_x or other amorphous N-containing materials such as Si-B-C-N. In particular, CN_x samples prepared to date are limited in N content to below approximately 35% with mostly sp^2-bonded carbon. For materials prepared by plasma sputtering, these limits may be due to a thermodynamic preference to pair N atoms into free N_2 molecules instead of incorporating them into the amorphous network

In this chapter we report *ab initio* molecular dynamics liquid quench simulations of N-rich amorphous CN_x and Si-B-C-N materials, in which we observe the formation of N_2 molecules under typical deposition conditions. We closely examine the formation of N_2 molecules in liquid quench simulations and propose a novel algorithm that suitably removes N_2 molecules in the course of a simulation. Using this algorithm, we identify the main factors that minimize the amount of N_2 formed and therefore maximize the N-content in deposited materials. This suggests experimental conditions that could potentially lead to novel materials with enhanced N content.

Simulations here focus on one Si-B-C-N material with composition $Si_{14}B_{23}C_6N_{57}$ and one B-C-N material with composition $B_{41}C_8N_{51}$. Other elements detected in these samples in small quantities (Ar < 3 at.%, H < 4 at.%) were neglected. The Si-B-C-N sample was chosen because of its relatively high nitrogen content, which facilitates the study of N_2 formation processes during liquid-quench simulations. The B-C-N sample was chosen because it was prepared under similar conditions to the Si-B-C-N sample except for the absence of Si in the sputter target.

5.2 Results

5.2.1 N_2-formation during liquid quench simulation

Liquid quench simulations were performed for the Si-B-C-N and B-C-N compositions described above. These were carried out using a simulation cell containing 100 atoms with the cell volume set to match the experimental atomic density. The exponential cooling time from 5000 to 650 K was 100 fs; this is shorter than the 500 fs used for SiC simulations in Ref. 2 in

accordance with the higher thermal diffusivities for various amorphous Si-C-N and B-C-N materials reported in Ref. 3.

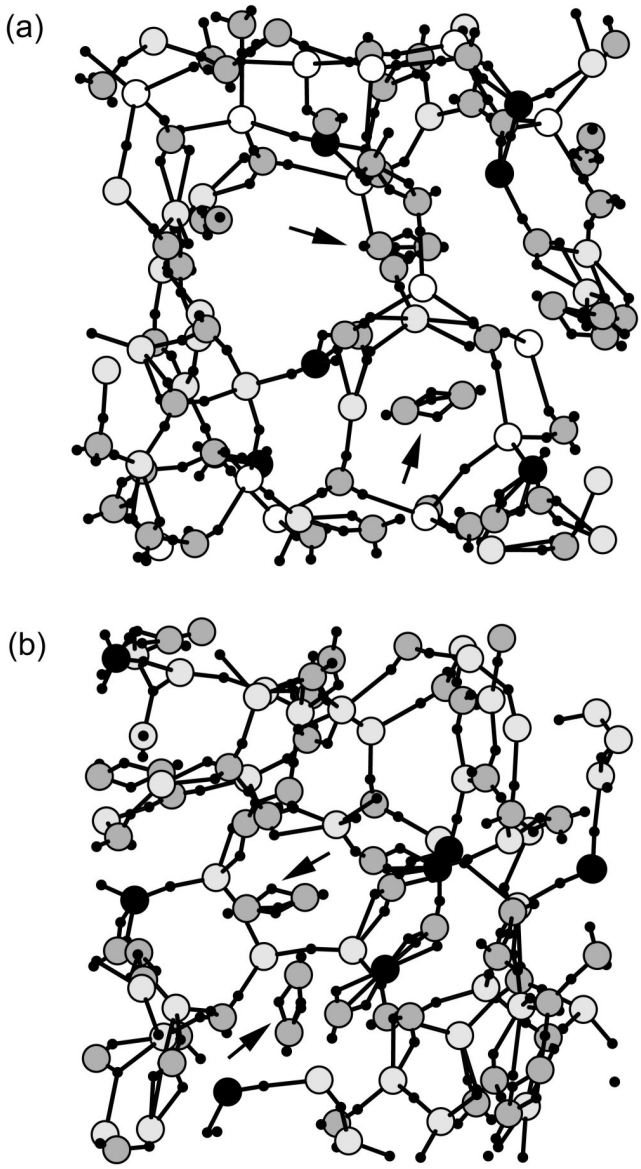

Fig. 5.1: *Snapshots from the liquid-quench simulation of a Si-B-C-N material of composition $Si_{14}B_{23}C_6N_{57}$ (panel a) and a B-C-N material of composition $B_{41}C_8N_{51}$ (panel b). Five N_2 molecules formed during the liquid-quench phase of the simulation in the Si-B-C-N sample and four in the B-C-N sample are present. Large black circles are C, dark grey are N, light grey are B, white circles correspond to Si, the small black dots represent Wannier function centres (WFCs).*

Typical Si-B-C-N and B-C-N structures that are obtained at the end of the exponential cooling and subsequent equilibration run are shown in Figs. 5.1(a) and (b). Clearly seen in Fig. 5.1(a) are five N_2 molecules that are not covalently bonded to the amorphous network. Inspection of the molecular dynamics trajectories reveals that these molecules were formed during the cooling and equilibration and remained trapped in the cell. Similarly, at the end of

the simulation for the B-C-N material four N_2 molecules were found. N_2 formation during liquid quenching was also reported for BN material in Ref. 4, but without any detailed analysis.

We expect that every N_2 molecule formed during the synthesis escapes from the deposited material since the thermal spike in which the molecules are formed is always close to the material surface. Repeated thermal spikes at the same location would also facilitate N_2 out-diffusion. The absence of N_2 molecules was experimentally confirmed by thermogravimetric analysis[5], which revealed no mass loss (indicative of N_2 outgassing) up to 1300 °C.

In order to explore the effect of atomic density on the number of N_2 molecules formed, identical liquid-quench simulations for these two materials were carried out with atomic densities increased by 10, 20 and 30 % relative to the experimental density. Figure 5.2 shows that an increase in the simulation density leads to a reduction in the number of N_2 molecules formed. This indicates that high-density networks have the potential to incorporate more nitrogen. The calculated stresses for both the Si-B-C-N and B-C-N compositions are compressive and substantially larger for B-C-N. While our simulation method consistently overestimates stress values and does not account for any long time scale post-deposition stress relief processes, some observations can be made regarding relative stresses. Our findings are in qualitative agreement with the experimentally measured stresses of -1.15 and -2.34 GPa for the Si-B-C-N and B-C-N samples, respectively. For both the samples, the compressive stress increases significantly with increasing density beyond a second point of the dependence, while the reduction in slope of the compressive stress between the first and second points to the decrease in the molecular N_2 content.

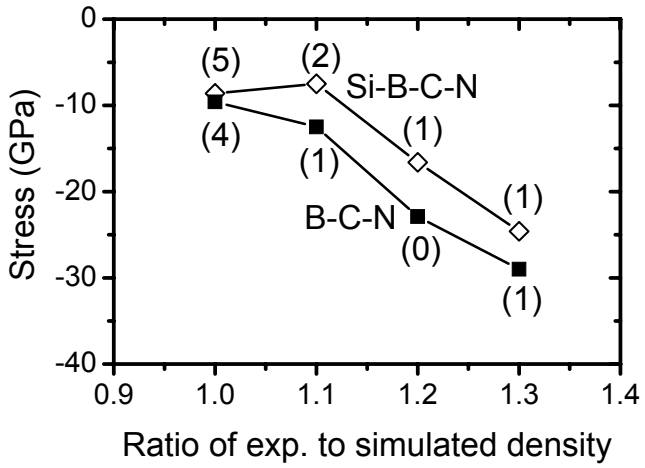

Fig. 5.2: *The effect of simulation density on calculated compressive stress and on the number of N_2 molecules formed. Numbers in parentheses indicate the numbers of N_2 molecules formed during the simulation.*

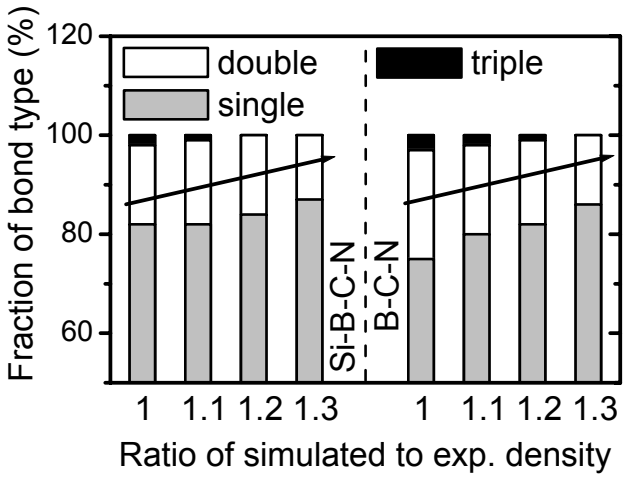

Fig. 5.3: *The predicted effect of the density of deposited Si-B-C-N materials on the occurrence of single, double and triple bonds of all kinds in the network. Triple bonds associated with N_2 molecules are not included.*

Figure 5.3 shows the average percentages of single, double and triple bonds as a function of the density of the simulated sample. The data shows that an increase in density leads to an increase in the ratio of single to double bonds. Increased density results in increased coordination numbers and hence a tendency towards reduced bond order. In the case of nitrogen, this is reflected in a reduction in triple bonds present in N_2 molecules in preference for single and double bonds linking nitrogen into the network.

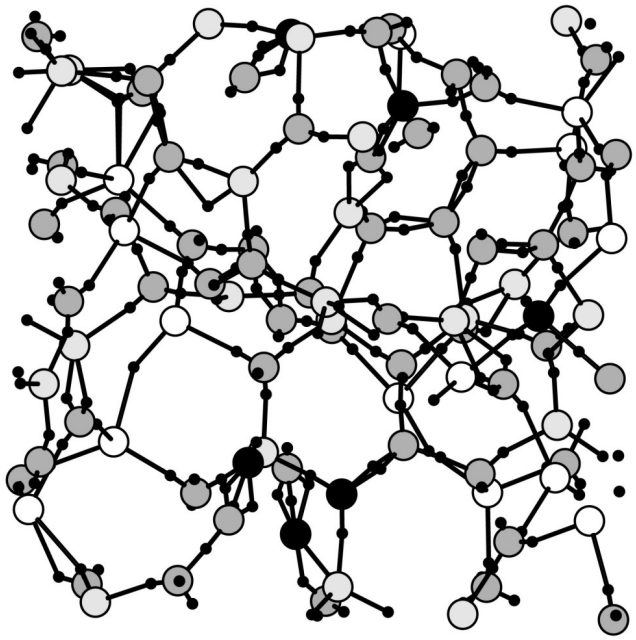

Fig. 5.4: *A snapshot from the liquid-quench simulation of a Si-B-C-N material of composition $Si_{14}B_{23}C_6N_{57}$. Thirty-two extra nitrogen atoms were added at the start of the simulation and seventeen N_2 molecules were removed during the liquid quench. The final elemental composition is therefore $Si_{14}B_{23}C_6N_{55}$. The large black circles are C, dark grey are N, light grey are B, white correspond to Si and the small black dots represent Wannier function centres.*

5.2.2 Liquid quench simulations with N_2 removal

The fact that our initial simulations lead to the formation of N_2 molecules in the network that are not confirmed in experiment, prompted us to revise our simulation strategy. Exponential cooling and equilibration MD runs were stopped at regular intervals in order to remove any N_2 molecules from the simulation cell. After each N_2-removal, the simulation volume was adjusted so that the atomic density was maintained. A wave function optimisation was performed before the MD simulation was resumed. This modified liquid quench algorithm leads to final structures that do not contain any N_2 molecules and are therefore likely to be better representations of the experimental materials. In order to obtain a final structure with desired N-content, these simulations need to be started with nitrogen atoms in excess of the experimental N-content in the expectation that N_2 molecules will be formed and removed during the simulation. As mentioned previously, it is likely that N_2 molecules form and diffuse out of the structure during synthesis. Three such simulations on Si-B-C-N were performed containing 0, 16 and 32 extra nitrogen atoms in addition to the 100 atoms of experimental elemental composition ($Si_{14}B_{23}C_6N_{57}$). After approximately 1 ps of equilibration, this new algorithm leads to stable structures and N_2 molecule formation stops. The final structures (e.g. Fig. 5.4) do not contain any N-N triple bonds (e.g. azide – N_3) that could potentially lead to N_2 molecules after longer simulation times.

Fig. 5.5 shows that simulations with a sufficiently high number of extra nitrogen atoms at the start of the simulation lead to final structures with the desired experimental composition. With an exponential cooling time of 100 ps, a nitrogen-excess of 0, 16 and 32 N atoms resulted in final nitrogen contents of 51, 55 and 56 at.%, to be compared with 57 at.% in the experimental sample. However, The method requires some tuning to achieve a particular N concentration in the simulated structure because not only the starting nitrogen content but also the cooling time influences on the number of N_2 molecules formed and thus the final nitrogen content.

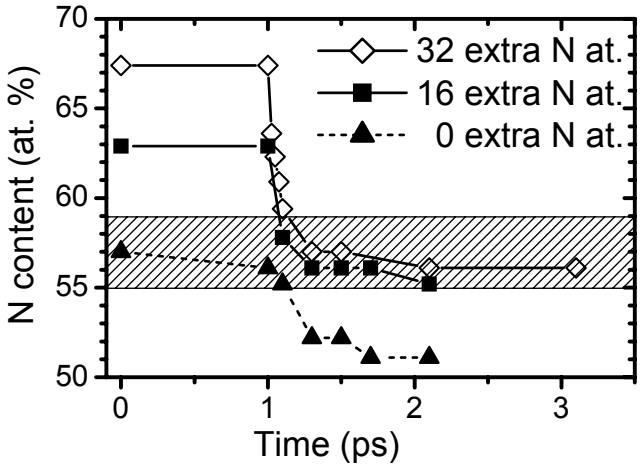

Fig. 5.5: *The total nitrogen content as a function of simulation time during liquid-quench simulations of the Si-B-C-N material ($Si_{14}B_{23}C_6N_{57}$) with removal of N_2 molecules after formation. Three simulations, which started with a nitrogen excess of 0, 16 and 32 atoms beyond the 100 atoms of experimental composition, resulted in structures with different final N-content. The shaded area marks the experimental N-content (with ±2 % error). The exponential cooling time was 100 fs.*

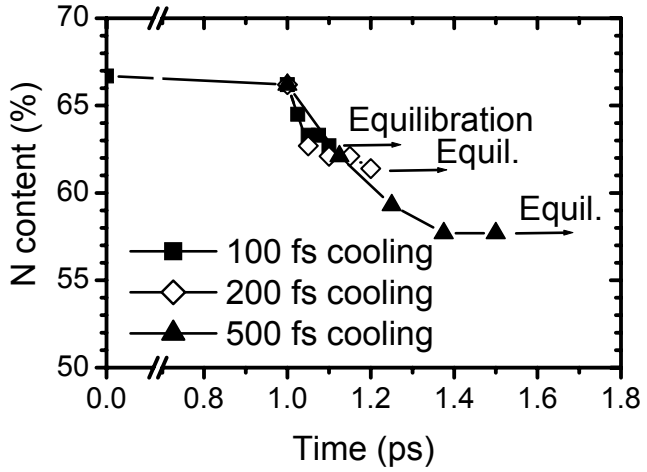

Fig. 5.6: *The nitrogen content as a function of simulation time for liquid-quench simulations of composition $C_{44}N_{88}$ with removal of N_2 molecules, showing the effect of cooling time (100, 200 and 500 fs).*

The fact that the final N-content depends strongly on the cooling time is illustrated in Figure 5.6. This figure shows our results for a CN_x material (composition $C_{44}N_{88}$, mass-density 3g/cm^3) for which liquid-quench simulations with different exponential cooling times (100, 200 and 500 fs) lead to different nitrogen contents. Longer exponential cooling times lead to the formation of more N_2 molecules during cooling and hence lower N-content in the final structure, 63, 61 and 58 at.% for cooling times of 100, 200 and 500 fs, respectively. This indicates a possibility of enhancing the nitrogen content in materials such as CN_x prepared by physical vapour deposition (PVD) methods by increasing the cooling rate. This could be achieved, for example, by decreasing the substrate surface temperature during the deposition.

5.2.3 The temperature window for N_2 formation.

The formation of N2 molecules requires sufficient energy to break bonds containing N atoms that are part of the network and to enable the diffusing N atoms to find one another before forming another bond. We have observed in our simulations that at temperatures below 650 K no further N_2 formation takes place. The thermal energy is there insufficient for the extraction of N atoms out of the network. At sufficiently high temperatures N atoms remain non-bonded because the thermal energy is too high for any N_2 molecules to remain undissociated . In earlier work[6,7], it was found that significant thermal N_2 dissociation required temperatures of 8000 K or more. Together, these two observations suggest that there exists a temperature window for the formation of N_2 molecules in PVD processes. Here we are particularly interested in the lower boundary of this temperature window.

In order to determine the temperature window within which N_2 formation is likely, we performed a series of constant temperature MD simulations with temperatures between 1000 and 7000 K. These simulations were started using a single molten structure of composition $C_{44}N_{86}$, which was generated using the initial mixing run (see the description of the liquid-quench algorithm in section 2.2.2) N_2 molecules which formed during the mixing were removed from the structure. The structure was then wavefunction optimized and initial velocities appropriate for the constant temperature simulation were allocated. As in the previous liquid quench simulations, N_2 molecules were removed from the simulation cell at

regular intervals. With this type of simulation we were able to examine the rate of N_2 formation as a function of temperature and thereby characterise the temperature window.

Figure 5.7 shows the number of N_2 molecules formed (and removed) after 200, 400 and 800 fs simulation times as a function of temperature. The figure clearly shows that the maximum rate of N_2 formation occurs between 4000 and 5000 K, with a maximum of 19 N_2 molecules formed after 800 fs at 5000 K. Note that a number of N atoms start out in close proximity and are prone to form N_2 molecules immediately. This phenomenon led to eight N_2 molecules forming at 1000 K where diffusion does not play a significant role. These N_2 molecules are not of relevance to the temperature window, since they do not involve diffusion processes or the release of N atoms from the network. Above 1000 K, the rate of N_2 formation steadily increases until a maximum at 5000 K is reached. Above 5000 K, the rate progressively decreases because two N atoms encountering each other are increasingly likely to carry too much thermal energy to form a stable N_2 molecule. Our constant temperature simulations show that the temperature window with effective N_2 formation occurs between 3000 and 6000 K.

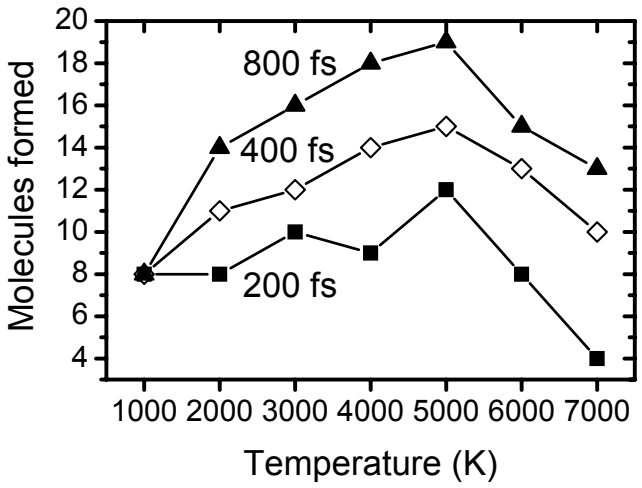

Fig. 5.7: *The number of N_2 molecules formed in the $C_{44}N_{86}$ sample during 800 fs long MD runs at various temperatures. In the lower temperature part of the figure, the first eight N_2 molecules arise from 16 N atoms that start out in close proximity to one another. At 1000 K, these eight N_2 molecules are the only ones formed. Between 1000 and 5000 K additional N_2 molecules form through diffusion. Above 5000 K, the formation of N_2 molecules is prevented by the high thermal energy of diffusing N atoms.*

5.2.4 Discussion

The simulations presented in this chapter are relevant to the PVD preparation of nitrogen containing materials such as CN_x, B-C-N and Si-B-C-N. In PVD processes, ion bombardment leads to local melting (thermal spike) at the site of impact. The rate of cooling and solidification depends on the thermal diffusivity of the target material. Our results, showing a temperature window, suggest that loss of nitrogen from the network occurs above approximately 3000 K through the formation of N_2-molecules. This suggests further that nitrogen uptake into deposited CN_x amorphous networks can be improved by reducing the time spent in this active temperature window. This could be accomplished by:

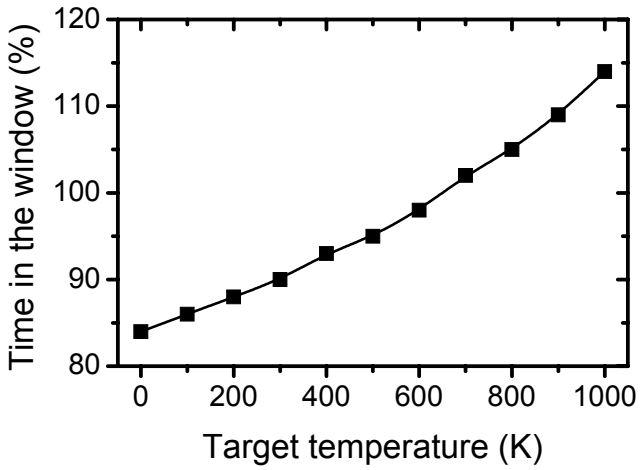

***Fig. 5.8**: Relative time spent in the 3000-6000 K temperature window as a function of the temperature to which the sample is cooled (target temperature). 100% refers to a target temperature of 650 K. A reduction in target temperature to 100 K for example leads to a 14 % reduction in the time during which active N_2 formation could occur. The calculations apply to a point halfway between the center and the boundary of a hemispherical thermal spike.*

(1) more effective cooling of the substrate during the deposition in order to increase the cooling rate.

(2) the use of a lower energy of bombarding ions which leads to more rapid cooling. Reducing ion energies too much, however, results in lower density materials and a reduced nitrogen uptake, as shown in Fig. 5.2.

Improved deposition processes, that incorporate these principles, may lead to materials with enhanced N-content. In order to quantify the effect of different target (substrate) temperatures on the time spent in the active temperature window, we used the expression for cooling of a hemispherical thermal spike of radius r_0 as developed in Ref. 8 for tetrahedral amorphous carbon. This expression assumes a constant thermal diffusivity of the material and allows us to estimate the temperature as a function of time for thermal spikes formed in materials held at various target temperatures. Hence, we can estimate the time, which the material spends in the active temperature window for N_2 formation (3000-6000 K). Figure 5.8 shows the result for a point halfway between the centre and the boundary of a thermal spike as a function of target temperature. A reduction in target temperature from 650 K to 100 K leads to a 14 % decrease in the time spent in the active window for N_2 formation.

5.3 Conclusions

In MD liquid quench simulations of Si-B-C-N, B-C-N and CN_x amorphous materials we have observed the formation of free N_2 molecules. We have identified a temperature window in which stable N_2 molecules are formed. Our results show that the final N-content in networks of given Si/B/C ratios depends both on the time spent in the active temperature window and on the density of the material. Higher coordination numbers occur in more dense materials and allow incorporation of more N into the network. An increase in the cooling rate is identified as a means of decreasing the time spent in the temperature window for N_2 formation and thus increasing the N-content of a given network. Cooling the sample during preparation is found to have limited potential for increasing the cooling rate; however, using lower energies of impact during growth may achieve higher N-content by forming smaller and hence more rapidly quenched thermal spikes. High N-contents are also expected for Si/B/C compositions with high thermal diffusivity.

5.4 References

1 J. Houška, M.M.M. Bilek, O. Warschkow, D.R. McKenzie and J. Vlček, Phys. Rev. B **72**, Art. No. 054204 (2005).

2 P. Fitzhenry, M.M.M. Bilek, N.A. Marks, N.C. Cooper and D.R. McKenzie, J. Phys.: Condens. Matter. **15**, 165 (2003).

3 S. Chattopadhyay, S.C. Chien, L.C. Chen, K.H. Chen and H.Y. Lee, Diamond Relat. Mater. **11**, 708 (2002).

4 D.G. McCulloch, D.R. McKenzie and C.M. Goringe, J. Appl. Phys. **87**, 5028 (2000).

5 J. Vlček, S. Potocký, J. Čížek, J. Houška, M. Kormunda, P. Zeman, V. Peřina, J. Zemek, Y. Setsuhara and S. Konuma, J. Vac. Sci. Technol. A **23**, 1513 (2005).

6 S. Mazevet, J. D. Johnson, J. D. Kress, L.A. Collins and P. Blottiau, Phys. Rev. B **65**, 014204 (2001).

7 M. Ross, J. Chem. Phys. **86**, 7110 (1987).

8 N.A. Marks, Phys. Rev. B, **56**, 2441 (1997).

6 A new method for obtaining desired compositions in liquid-quench simulations of nitrogen-containing materials

This chapter is based on results included in Ref. 1. A modified liquid-quench algorithm with a flexible cooling time which can lead to desired compositions of N-containing materials without any N_2 molecules in their final structure is described here. It solves the problem presented in the previous chapter 5 (formation of N_2 molecules in the simulation cell during classical liquid-quench simulations). The new algorithm presented here was used to obtain the simulation results presented in the following chapters 7 and 8.

6.1 Introduction

As we have shown in the previous chapter 5, molecular dynamics (MD) simulation of N-containing materials such as CN_x or Si-B-C-N may lead to the formation of N_2 molecules in the simulation cell. These molecules are likely to diffuse out of the real material during deposition, whereas they are normally prevented from doing so in the simulation and remain trapped in the cell. We have shown that a certain nitrogen excess in the starting cell can when used with an appropriate cooling rate lead to a structure with approximately the desired N content if all of the N_2 molecules are removed after forming. However, the determination of an appropriate cooling time can be very computationally expensive. Moreover, it is desirable not to fix the cooling time because variations in cooling time are often used in the liquid-quench protocol for simulating ion bombardment at different energies. The energy of the ion impact determines the size of the molten region and hence its cooling rate.

In this chapter, we present a modified liquid-quench algorithm with a flexible cooling time which can lead to predetermined compositions of N-containing materials without N_2 molecules in their final structure. We justify the algorithm by studying the bond-forming and bond-breaking processes in CN_x, BN_x and SiN_x materials at various temperatures and comparing with experimental data where possible.

We studied the bond-forming and bond-breaking processes in the sample $C_{44}N_{86}$ of density 3g/cm^3 by performing 0.5 ps long constant-temperature MD runs at various temperatures up to 7000 K. To determine equilibrium properties of the structure, 0.5 ps long constant-temperature MD runs were performed for samples $B_{44}N_{86}$ and $Si_{44}N_{86}$ of the same atomic density at 5000 K only. Prior to the constant-temperature MD runs, each sample has been mixed by melting in order to remove memory of the initial configuration.

6.2 Specific methodology

Because we did not calculate positions of Wannier function centres (WFCs) during these simulations, the bonding analysis in this chapter is based on the use of bonding distance cutoffs. Two network atoms were considered to be bonded if their distance was ≤2.0 Å for C-C, ≤1.9 Å for C-N, ≤2.1 Å for B-B, ≤2.1 Å for B-N, ≤2.8 Å for Si-Si, ≤2.2 Å for Si-N and ≤1.8 Å for N-N pairs. A N_2 molecule was considered to be formed if in two consecutive snapshots of the structure the distance of two N atoms was ≤1.3 Å and these atoms were bonded only to each other. The triple bond between these two N atoms was then considered to be broken or converted to single or double bond when distance between these atoms increased to ≥1.6 Å. Temporary bonding of the N_2 molecule to the network wasn't considered as a breaking of the molecule. This choice of these maximal bond lengths leads to maximal calculated lifetimes of network bonds, and a ratio of around 1.25 for the maximal to average

(as identified by WFCs) bond lengths (single for network bonds, triple for N_2 molecules) for all bonds.

6.3 Results

6.3.1 The modified liquid-quench algorithm

When a MD simulation of N-containing material is commenced, a number of N_2 molecules form immediately due to the random presence of some N pairs in close proximity in the starting configuration (see the previous chapter 5). This is followed by formation of additional molecules as a result of diffusion and bond-breaking processes. An example of a simulated CN_x sample including free N_2 molecules is shown in Fig. 6.1, with Wannier function centres representing pairs of valence electrons.

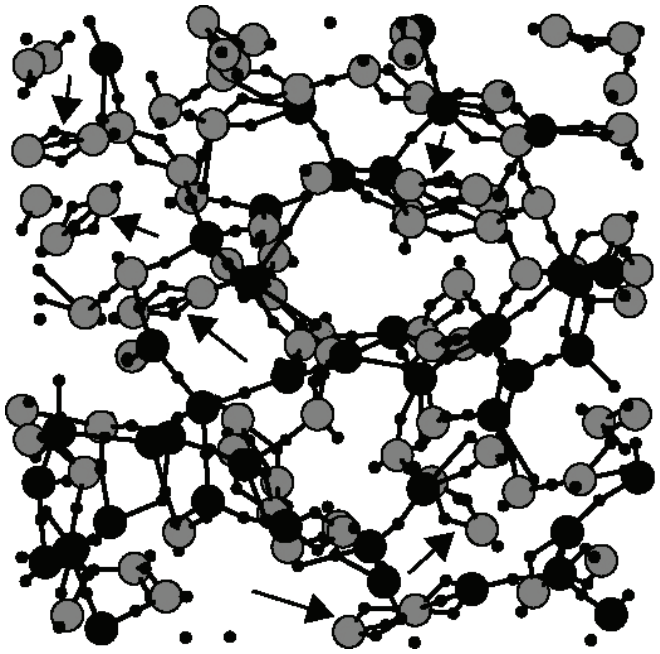

***Figure 6.1**. Snapshot from the liquid-quench simulation of a CN_x material of composition $C_{44}N_{86}$. Six of the triple-bonded N-N pairs (free N_2 molecules or their precursors) formed during the simulation are denoted by arrows. Large dark circles are C, large light circles are N and the small black dots represent Wannier function centers.*

In order to compensate for N atom loss and still achieve a desired N-content in the quenched material, the liquid quench simulation was commenced with a substantial N-excess. In the previous chapter, we identified a temperature window for N_2 formation in alloys of this type between 3000 and 6000 K. Below 3000 K, N-N pairs which previously formed a triple bond can leave the network and form a free molecule, but no new triple N-N bonds form. In the light of this information we modified some stages of the liquid quench algorithm. The new algorithm is described below with examples taken from Ref. 9 for simulations of previously deposited amorphous materials. At the end of each stage, any new N_2 molecules formed are removed, the cell dimension is scaled in order to keep the atomic density constant and the wavefunction is optimized.

(1) *Starting Structure*: An initial structure is generated by distributing 100 atoms of the experimental composition with up to 32 additional N atoms distributed semi-randomly over the simulation cell of a dimension chosen to give the desired atomic density. The optimal N-excess for various samples increases with decreasing atomic density, that is, with increasing rate of N_2 formation.

(2) *Initial Mixing*: In order to obtain a completely randomized structure with no memory of the initial structure, a 1 ps MD run at a temperature above melting point (5000 K - Nose-Hoover [NH] thermostat) is carried out. A plane-wave cut-off of 10 Ry is sufficient for this stage of the simulation where high accuracy of the DFT energies is not required. The low cut-off increases the efficiency of the simulation, and was also found useful as it effectively prevents the formation of stable bonds which would interfere with efficient mixing.

(3) *N_2 Removal Run*: The previously used exponential cooling applied to temperatures above 3000 K (that is, inside the temperature window for N_2 formation) is now replaced by a constant temperature MD run of flexible length. The target temperature chosen for this run is above the temperature at which stable network bonds start to form, so we can use its length to control the amount of N_2 formation without affecting the final structure. During this run, the structure is inspected at regular intervals (every 50 fs) using Wannier function analysis. The run is stopped when the number of N atoms involved in either free N_2 molecules or in other triple bonded N-N pairs is equal to the starting N excess. This criterion is based on our experience which has shown that triple` bonded pairs of network N atoms are early precursors of N_2 molecules.

(4) *Exponential Cooling*: The resulting material (having the desired composition with additional triple-bonded N-N pairs) is exponentially cooled down from (only) 3000 K to the target (i.e. substrate) temperature. Temperature control is achieved by rescaling the velocity of ions when the actual and target temperatures differ by more than 10%. By adjusting the cooling time in this phase of the simulation, it is still possible to simulate the effect of varying ion bombardment energies. In our simulations, most of the remaining N-N triple bonds were converted to N_2 molecules during the exponential cooling.

(5) *Equilibration*: The rest of the liquid-quench algorithm is unchanged. After the cooling phase, sample equilibration is accomplished using a 1 ps MD run at deposition temperature (NH thermostat). The purpose of equilibration is for the system to fully recover thermal equilibrium as indicated by a constant mean squared displacement.

(6) *Production Run:* Following equilibration, various quantities of interest (such as bonding statistics or stress) can be computed as statistical averages over a MD run of a minimal length of 0.5 ps at deposition temperature.

6.3.2 Temperature of the N_2 removal run

The N_2 removal run has to be accomplished at sufficiently high temperature, above the melting point at which no stable network bonds form so that the high mobility of atoms allows diffusion and bond-breaking processes, leading to formation of N_2 molecules. However, the temperature must be also sufficiently low to ensure stability of the N_2 molecules formed. This prompted us to find a temperature window fulfilling these conditions by studying bond-forming and bond-breaking processes in a sample of CN_x material of starting composition $C_{44}N_{86}$ and density 3g/cm^3. Constant-temperature MD rums were performed at various temperatures and the results are summarized in Fig. 6.2.

Fig. 6.2(a) shows lifetimes of network bonds and N_2 molecules formed during 500 fs MD runs in the CN_x sample as a function of temperature. The results show that the N_2

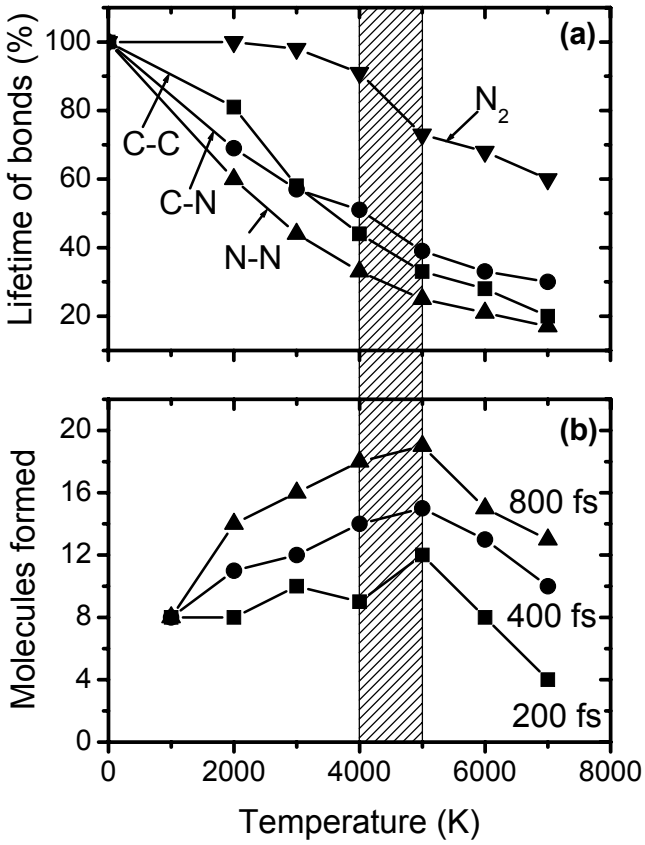

Figure 6.2. *Panel (a) shows lifetimes of network bonds and N_2 molecules in sample $C_{44}N_{86}$ during 500 fs MD runs at various temperatures. Lifetimes are shown as percentages of maximum possible lifetimes (the time from the formation of the bond/molecule until the end of the simulation). Panel (b) shows the rate of formation of free N_2 molecules in the same sample $C_{44}N_{86}$ during 800 fs MD runs at various temperatures (ie. the numbers of N_2 molecules formed in the CN_x sample after 200, 400 and 800 fs are plotted). The cross-hatched area indicates the recommended temperature range for the N_2 removal run (4000 - 5000 K).*

molecules formed are stable at significantly higher temperatures than the network bonds. This is due to the high bond energy of the triple N-N bonds. The difference of lifetimes is largest in the range 4000 - 5000 K. The network bonds are not stable in this range (the material is molten), while the lifetime of N_2 molecules is comparable with the length of the MD run from the time of their formation (shown as 100 %). We note that the simulations shown here were performed with relatively high material density. This justifies the general use of our algorithm at all densities, because for lower density materials the lifetimes of N_2 molecules are even higher.

Fig 6.2(b) shows the number of N_2 molecules formed in the CN_x sample after 200, 400 and 800 fs simulation times as a function of temperature. This result is repeated from chapter 5 for the reader's convenience. The figure clearly shows that the maximum rate of N_2 formation occurs between 3000 and 6000 K, with a maximum of 19 N_2 molecules formed after 800 fs at 5000 K. Note that a number of N atoms started out statistically in close proximity and these atoms tend to form N_2 molecules immediately. This leads to eight N_2 molecules at 1000 K where diffusion does not play a significant role. These N_2 molecules are not of relevance to the temperature window, since they do not involve diffusion processes or

the release of N atoms from the network. Above 1000 K, the rate of N_2 formation steadily increases until a maximum at 5000 K is reached. Above 5000 K, the rate progressively decreases because two N atoms encountering each other are increasingly likely to carry too much thermal energy to form a stable N_2 molecule. In these simulations all N_2 molecules formed were considered to be stable, so it is possible that the real rate of the N_2 formation decreases even more at high temperatures.

Collectively, the results presented suggest that the N_2 removal run should be accomplished at temperature(s) between 4000 and 5000 K. In this range, the effective formation of relatively stable N_2 molecules has been observed, while the rest of the material is molten. Because the material is in a molten state, the final structure is not affected by replacing the exponential cooling above 3000 K by the constant temperature N_2 removal run or by length of this run.

In order to confirm the suitability of our protocol for materials other than CN_x, 500 fs constant temperature MD runs were performed at 5000 K for samples of SiN_x and BN_x. These samples had the same atomic density and equivalent composition ($Si_{44}N_{86}$ and $B_{44}N_{86}$, respectively) as the previous CN_x sample. Fig 6.3 shows for these materials similar lifetimes of N-containing bonds (including N_2 molecules), while lifetimes of the B-B and Si-Si bonds are even shorter than the lifetime of C-C bonds.

Moreover, it is revealed in Fig. 6.3 that formation of N_2 molecules in the SiN_x material is much less intensive than in the BN_x and CN_x materials at the same temperature and atomic density. Only one N_2 molecule was formed during the 500 fs MD run in the $Si_{44}N_{86}$ sample in comparison with 13 and 17 molecules formed in the $B_{44}N_{86}$ and $C_{44}N_{86}$ samples, respectively. This illustrates the experimentally observed effect of Si to improve the retention of N in structures of N-containing materials prepared with varied Si-content[2-4].

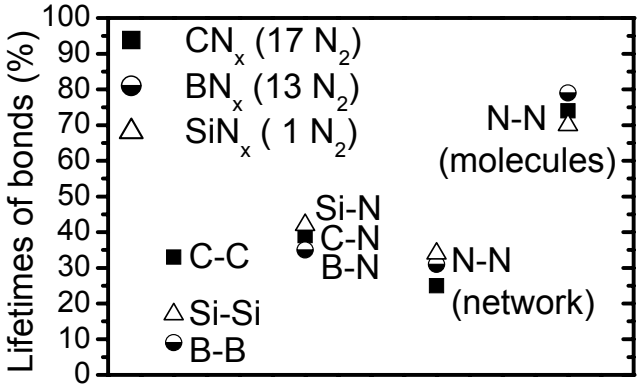

Figure 6.3. *Lifetimes of network bonds and N_2 molecules in samples of $C_{44}N_{86}$, $B_{44}N_{86}$ and $Si_{44}N_{86}$ during 500 fs MD runs at 5000K. Lifetimes are shown as percentages of maximum possible lifetimes (the time from the formation of the bond/molecule until the end of the simulation). Numbers of N_2 molecules formed are given in the legend.*

The lifetimes of Si/B/C-containing bonds at the same temperature and atomic density correlate perfectly with proportions of these bonds observed in experimentally prepared Si-B-C-N materials[5]. It was shown in Ref. 5 by X-ray photoelectron spectroscopy that Si, B and C preferentially bond to N. The analysis also detected some C-C (and Si-C) bonds, but evidence of Si-Si and B-B bonds was not seen (note short lifetimes of these bonds in Fig. 6.3).

6.4 Conclusions

In MD liquid quench simulations of N-containing amorphous materials we have observed the formation of free N_2 molecules. In order to compensate for the loss of N atoms and still achieve a desired N-content in the quenched material, the liquid quench simulations of these materials were commenced with sufficient N-excess. We developed a modified liquid-quench algorithm in which the N_2 molecules are removed from simulation cell after forming. In this protocol, the high-temperature part of simulation where the material is molten and the N_2 molecules form is flexible in its time duration. We have shown that this *N_2 removal run* has to be accomplished between 4000 and 5000 K where the effective formation of relatively stable N_2 molecules has been observed, while in the rest of the material no stable network bonds form. The results also suggest that for given temperature and atomic density the rate of N_2-formation in Si/B/C-containing materials decreases with increasing Si-content. This explains the ability of Si to enhance the final N-content in experimentally prepared materials.

6.5 References

1 J. Houška et al., prepared for submitting to Molecular Simulation.

2 L.C. Chen, K.H. Chen, S.L. Wei et al., Thin Solid Films **355**, 112 (1999).

3 T. Berlind, N. Hellgren, M.P. Johansson, L. Hultman, Surf. Coat. Technol. **141**, 145 (2001).

4 J. Vlček, M. Kormunda, J. Čížek, Z. Soukup, V. Peřina, J. Zemek, Diamond Relat. Mater. **12**, 1287 (2003).

5 J. Vlček, S. Potocký, J. Čížek, J. Houška, M. Kormunda, P. Zeman, V. Peřina, J. Zemek, Y. Setsuhara and S. Konuma, J. Vac. Sci. Technol. A **23**, 1513 (2005).

7 The effect of argon on the structure of amorphous Si-B-C-N materials

This chapter is based on results published in Ref. 1. Using liquid quench simulations, we investigate here how the presence of Ar atoms in the sample affects the liquid quench and the final structure of the S-B-C-N materials. In the absence of Ar, we find that the final structures are homogeneous. The presence of Ar however leads to the formation of silicon-enriched regions in the vicinity of implanted Ar atoms. This result provides new insight into the role of implanted Ar in formation of structures in amorphous S-B-C-N materials. It also explains the ability of Si to relieve stress generated by these implanted Ar atoms.

7.1 Introduction

Since sputtering is typically performed in an Ar-containing atmosphere, materials prepared with this method are found to contain small amounts of implanted Ar atoms. These atoms arise from the impact of energetic Ar atoms or ions from the discharge or their reflection from the sputtering target[2]. Implantation of Ar has been correlated with the presence of compressive stress in the films[3,4]. It has previously been noted in the chapter 3 that the implantation of Ar atoms into amorphous S-B-C-N materials (prepared by magnetron sputtering in various N_2+Ar mixtures) leads to variations in a number of material properties; for example an increase in compressive stress. Experimental results shown in chapter 3 (figure 3.7) suggest that compressive stress created by implanted Ar atoms is more effectively relieved in S-B-C-N films with high Si-content. In the literature, little has been reported concerning the mechanism by which Ar incorporation affects structural and mechanical properties of these materials. First-principles simulations are performed in this chapter to understand these observations at an atomistic level. We discuss the structural effects of Ar on the network and how high Si content may help relieve that part of the compressive stress, which is caused by implanted Ar.

Our simulations in this chapter focus on samples of composition $Si_{32}B_{10}C_6N_{52}$ (deposited previously with various U_b between 0 and -500 V) and $Si_{32}B_{10}C_6N_{52}Ar_6$ (U_b = -500 V). Experimentally, the stronger Ar bombardment (discharge mixture Ar/N_2 = 3:1 instead of 1:1) was found to increase both the content of implanted Ar and the atomic density of the $Si_{32}B_{10}C_6N_{52}Ar_6$ sample.

The modified liquid-quench algorithm proposed in previous chapter 6, which accounts for formation of N_2 molecules during quenching, was been used for the simulations discussed in this chapter. A cooling time of 500 fs was used to simulate materials deposited with U_b = -500V, while shorter cooling times were used to simulate the effect of lower $|U_b|$. Although all deposited samples were found to contain small amounts of hydrogen, this was not included in the simulations.

7.2 Results

7.2.1 Simulations of material without implanted Ar

We first discuss our simulations of a sample of composition $Si_{32}B_{10}C_6N_{52}$ where our initial objective is to demonstrate that this composition prefers a homogeneous distribution of atoms in the network; i.e. this material does not segregate into locally distinct regions or phases. Because our simulations are run in relatively small unit cells, a demonstration of homogeneity in a network is not straightforward. This is because we have to distinguish between genuine and coincidental phase segregation; the latter refers to the situation that the initial distribution of atoms contains random inhomogeneities.

Full liquid-quench simulations of the $Si_{32}B_{10}C_6N_{52}$ structure were performed using exponential cooling times of 100 fs and 500 fs to simulate the effect of bias voltages U_b of -100 and -500 V, respectively). A typical snapshot of the structure obtained from these simulations is shown in figure 7.1. In the upper part of the figure, we can see a region of SiN_x containing no B and C atoms.

In order to quantify segregation we introduce two criteria. Since we have more than 50% N in our compositions, likely binary phases are SiN_x or BN_x or CN_x. Our first criterion to measure the presence of such phases is the percentage of N atoms bonded only to one of Si, B or C. The number of bonds between atoms of the same kind is a second criterion, which detects the existence of elemental phases (such as pure Si or C networks).

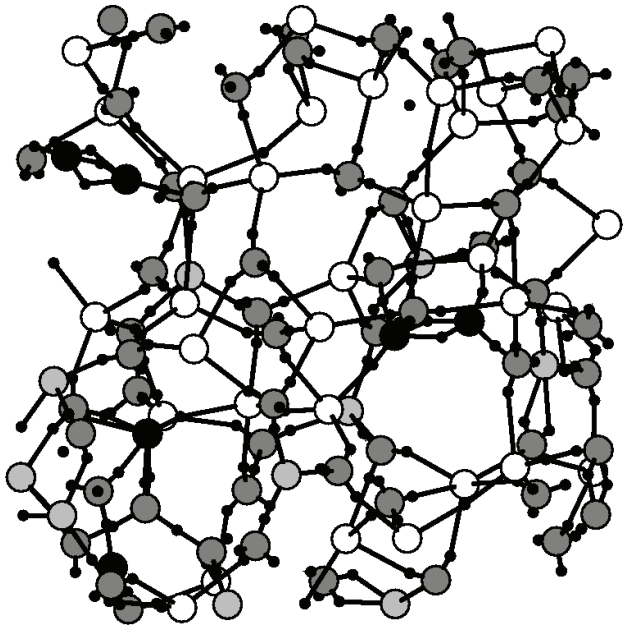

Fig. 7.1*: Snapshot from the end of the liquid quench simulation of a S-B-C-N material of composition $Si_{32}B_{10}C_6N_{52}$ with no Ar atoms in the structure. Large black circles are C, medium grey are N, light grey are B, white circles correspond to Si, the small black dots represent Wannier function centres (WFCs).*

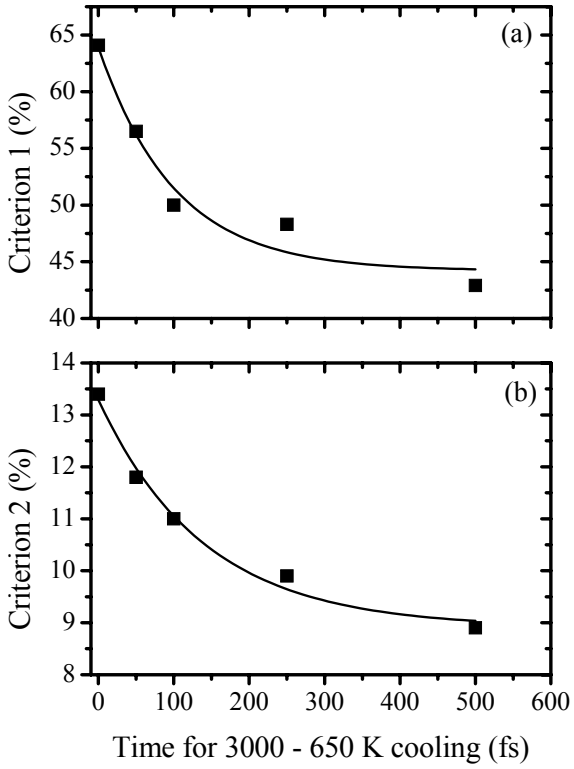

***Fig. 7.2**: Dependence of segregation in quenched structures of composition $Si_{32}B_{10}C_6N_{52}$ on the time taken to quench from 3000K to 650K. Segregation was measured using two criteria: Criterion 1 shown in (a) is the percentage of nitrogen atoms bonded to only one atom type (B, C, or Si) other than nitrogen. Criterion 2 shown in (b) is the percentage of chemical bonds between atoms of the same type. For both criteria, higher values are indicative of a less homogeneous structure. The 0 fs data point measures segregation in the molten structure prior to cooling. Subsequent data points characterize the structures just after cooling to 650K.*

Figure 7.2 shows these criteria applied to structures prior to cooling and after cooling runs of 50, 100, 250 and 500 fs. The data shows a continuous reduction of both segregation criteria; thus, there is a general increase in structural homogeneity with increased cooling time. We conclude that the initial SiN_x phase detected in the structure in figure 7.1 is the result of random clustering in the melt.

This result suggests that the $Si_{32}B_{10}C_6N_{52}$ composition has a thermodynamic preference for a maximally homogeneous structure. Long cooling times occur for impacts of high energy (high $|U_b|$ such as 500 V), for which we expect materials of homogeneous structure. In materials deposited with small $|U_b|$ such as 100 V some segregated regions such as SiN_x may survive.

7.2.2 Simulations of material with implanted argon

We now examine the effect of implanted argon on the S-B-C-N network. For this purpose 6 additional argon atoms were added into the network to form the composition $Si_{32}B_{10}C_6N_{52}Ar_6$ and simulations were performed with a cooling time of 500 fs. A typical simulated structure is shown in figure 7.3. The argon atoms are not bonded into the network (note how the WFCs associated with Ar are non-bonding). Five of the six argon atoms lie close together. The non-bonding character of the Ar creates "cavities" around them.

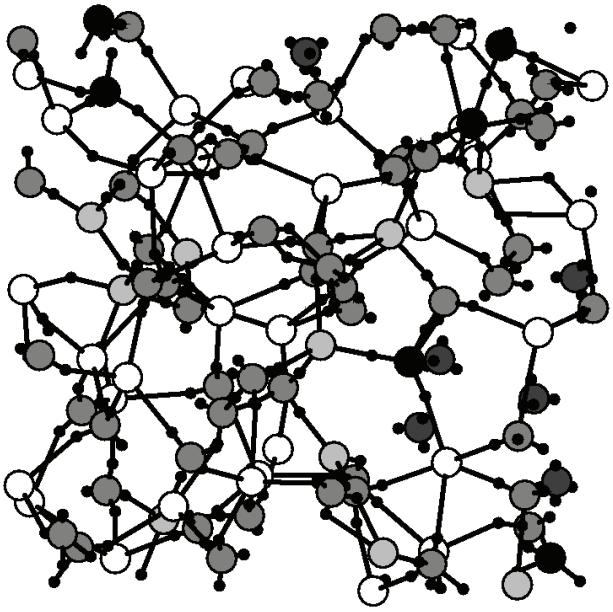

Fig. 7.3: *Snapshot from the end of a simulation of a structure of composition $Si_{32}B_{10}C_6N_{52}Ar_6$. Large black circles are C, medium grey are N, light grey are B, white are Si and dark grey (isolated) circles correspond to Ar. The small black dots represent Wannier function centres (WFCs).*

In order to determine the effect of implanted Ar atoms on structural homogeneity, we show in figure 7.4 the distributions of the distances of Si, B, C and N atoms to the nearest Ar atom. The distribution Si-Ar is more heavily weighted to short distances than are the distributions for the other atom types, suggesting the formation of a Si-rich phase around implanted Ar atoms. The average composition of the part of the sample surrounding the implanted Ar atoms (within a radius of $\leq$3.6 Å) is $Si_{36}B_9C_6N_{49}$, while the average composition of the rest of the sample is $Si_{24}B_{13}C_6N_{57}$. This difference can be considered significant because of the preference for a homogeneous structure in the sample without Ar, discussed in the previous section.

An explanation of this phenomenon may be that the longer and more flexible Si bonds (in comparison to B, C and especially N bonds) allow the Ar induced cavities to be accommodated into the structure with minimal energy penalty including generated stress. Covalent radii of Si, B, C and N are 1.11, 0.82, 0.77 and 0.75 Å. In our structure the calculated average bond lengths (including bonds of all orders with all species) were 1.80 for Si-containing bonds and 1.51 for all other bonds. The argon atoms sit in cavities with distances of at least 2.2 Å (lower bound of first peaks on figure 7.4) separating them from other atoms in the network. The longer bonds associated with silicon allow silicon rich regions to contain natural cavities which are larger than in silicon-poor regions. Such cavities

allow the incorporation of argon with minimum energy penalty. The flexibility of the long silicon containing bonds enables these bonds to deform to accommodate the argon atoms with minimal generation of stress. This explains the experimental observation (chapter 3) that compressive stress generated by implanted Ar is lowest in samples with highest silicon content.

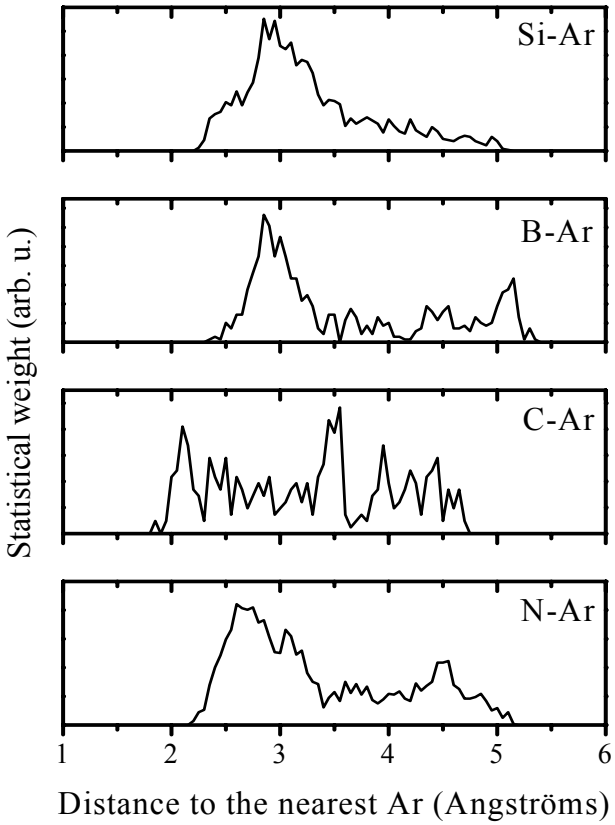

***Fig. 7.4**: Distributions of distances of Si,B,C and N atoms to the nearest Ar atom in the sample $Si_{32}B_{10}C_6N_{52}Ar_6$. Data are summarized over all atoms of the respective kind and over 69 snapshots made during the 0.5 ps production run at the end of the liquid-quench simulation. In the Si-Ar distribution a high proportion of the distances are in the lower part of the range.*

Deeper insight into the role of Ar in determining the structure of S-B-C-N materials can be gained by calculating selected statistics. Structural statistics comparing the $Si_{32}B_{10}C_6N_{52}$ and $Si_{32}B_{10}C_6N_{52}Ar_6$ samples, generated using cooling times of 500 fs (corresponding to the experimental U_b = -500 V), are shown in table 7.1. Table 7.1 reveals several important features of the effects of argon inclusion into the material.

quantity	S-B-C-N	S-B-C-N-Ar
Si content	32%	32% (36%)
Si-containing bonds	75%	73% (96%)
fraction of all B or C containing bonds which also include Si	9%	24% (66%)
Criterion 1 for segregation	43%	52%
Criterion 2 for segregation	9%	8%
average length - all bonds (Å)	1.70	1.72
average length - single BN (Å)	1.51	1.55
average length - single CN (Å)	1.41	1.46
number of rings	9.0	18.6
average ring size	5.8	6.0

***Table 7.1**: Selected averaged statistics for simulated materials $Si_{32}B_{10}C_6N_{52}$ and $Si_{32}B_{10}C_6N_{52}Ar_6$. The Si content percentages, given in brackets, are for the sub-set of atoms and bonds in the "vicinity" of Ar. Vicinity is defined for atoms as those which are closer than 3.6 Å to an Ar atom and bonds which have an Ar atom closer than 2.5 Å (perpendicular distance).*

- Silicon tends to accumulate in the vicinity of the Ar atoms. To show this, we use a statistic applying to the group of bonds surrounding argon atoms. These are defined as those bonds, which have a perpendicular distance of less than 2.5 Å to an argon atom. Silicon is present in 96% of these bonds whereas it is only present in 73 % and 75 % of all bonds in the argon-containing and argon-free sample, respectively.
- The presence of argon induces a major shift in the bonding preferences of all atom types. To show this we use the statistic shown in row 3 of table 7.1: fraction of all B or C containing bonds, which also include Si. B, C and Si tend to form bonds with N in the absence of argon, B exclusively whereas C and Si preferentially. This effect has also been noted in our experimental observations (Chapters 3 and 4). In the simulated Ar-containing sample the tendency for B and C to bond with Si is greatly increased. In the Ar-free sample, only 9 % of all bonds containing B or C contain Si, whereas in the Ar-containing sample 24 % of all bonds containing B or C contain Si. In the group of bonds surrounding Ar atoms, the effect is even more pronounced with 66 % of bonds containing B or C containing Si. These changes in bonding preference with the introduction of Ar are reflected in the increase in Criterion 1 as shown in row 4 of table 7.1.
- Although the Ar-containing sample is denser (smaller volume per atom), it is remarkable that the averaged bond length is larger (row 6) than that for the Ar-free sample. This is not only due to the higher total percentage of longer Si-containing bonds, but also due to the longer bonds of certain types (single BN, single CN) prevailing in the part of the sample far from the Ar atoms (rows 7 and 8). This keeps approximately the same atomic density in this part of the sample where the Si-content (and therefore the number of long Si-containing bonds) is reduced.
- Adding Ar to the sample also has a major impact on the topology of the network as revealed by the ring statistics. In the last 2 rows of table 7.1, we see that the number of rings is doubled after addition of Ar. This documents the transition from the 3D structure to the dense 2D envelopes around the Ar-containing cavities. The numbers of the rings were calculated using the algorithm of Franzblau[5].

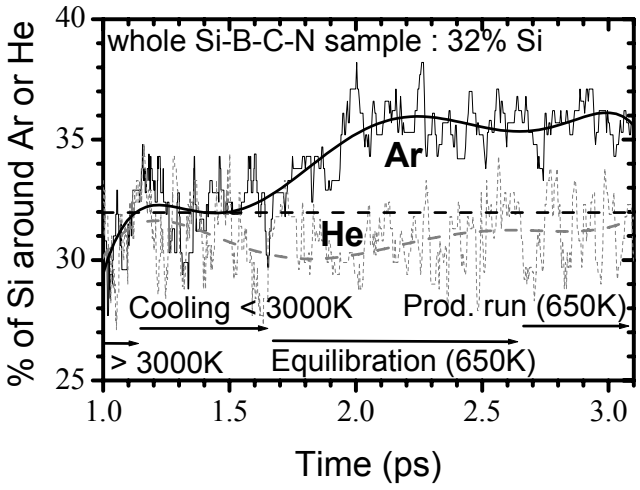

***Fig. 7.5**: The development of the segregation of Si around implanted Ar (larger microvoids) or He (smaller microvoids) atoms during the liquid-quench simulation of $Si_{32}B_{10}C_6N_{52}Ar_6$ and $Si_{32}B_{10}C_6N_{52}He_6$ structures. The y-axis shows the Si content percentages in the sub-set of atoms in the vicinity of Ar or He. Atoms in the vicinity are defined as those which are closer than 3.6 Å to an Ar or 3.2 Å to a He atom, respectively. The x-axis shows the time from start of the liquid-quench simulation. The average stable percentage of Si around implanted Ar/He atoms is close to the Si content in the entire Si-B-C-N sample for He, while it is significantly higher for Ar.*

Figures 7.5 and 7.6 show the effect of temperature on the segregation of Si around Ar atoms. Segregation is not stable in the molten state and is expected to occur below some temperature limit. The development of the percentage of Si around (up to 3.6 Å) Ar atoms during the liquid-quench simulation of the $Si_{32}B_{10}C_6N_{52}Ar_6$ sample is shown in figure 7.5. The trendline shows that this quantity starts to increase in the equilibration phase at the end of the cooling and increases during the equilibration until a maximum has been reached. The maximum exists because diffusion is limited once the solid has formed.

Figure 7.5 also shows the same statistic (i.e. percentage of Si around implanted inert gas atoms) in which the argon was replaced with helium. The same atomic density and cooling time have been used for this simulation. First minima of the pair correlation functions in which one of the atoms is He are around 1.9 Å in comparison with 2.2 Å for the Ar case. It suggests that the envelopes around smaller cavities containing He can be formed from all bond types rather than only from the long Si-containing bonds as in the Ar-containing structure. Thus, there isn't any observable segregation of Si around implanted He atoms.

In order to examine the effect of equilibration temperature on segregation of Si around Ar more closely, we performed a series of constant temperature 1 ps MD runs at temperatures between 100 and 2000 K. These simulations used the (nearly homogeneous) starting structure of the previous equilibration at 650 K. The velocities were scaled in accordance with the new temperature. For all temperatures, the percentage of Si around Ar atoms increased during the first 0.5 ps of equilibration while the mean value was stable during the second 0.5 ps. Figure 7.6 shows averaged stable values of percentages of Si around Ar for all simulated

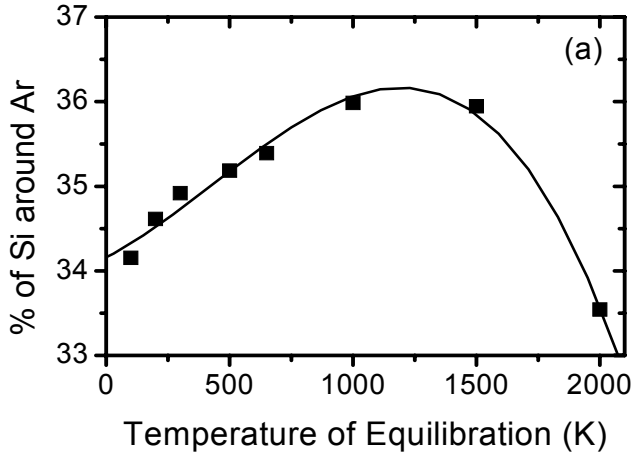

***Fig. 7.6**: Segregation of Si around implanted Ar atoms in samples of composition $Si_{32}B_{10}C_6N_{52}Ar_6$ equilibrated at various temperatures. The vertical axis refers to the percentage of Si atoms in the group of Si, B, C and N atoms that lie in the vicinity of an Ar atom. Atoms in the vicinity are defined as those which are closer than 3.6 Å to an Ar. The data are averaged over the stable period 0.5 – 1 ps from the start of equilibration. The percentage of Si around Ar reaches a maximum for equilibration temperatures in the range 1000 - 1500 K.*

equilibration temperatures. This figure also shows that for equilibration temperatures between 100 and 1000 K, the segregation of Si around Ar increases with increasing temperature. We attribute this to increasing temperature-dependent diffusion coefficients. At higher temperatures, the kinetic energies of atoms may be comparable or larger than the energy penalty associated with having the Ar cavities surrounded also by short and inflexible non-Si-containing bonds. This leads to a reduction in the degree of Si segregation around the Ar. These results lead us to predict that silicon should relax compressive stress generated in films deposited using argon sputtering more effectively at higher deposition temperatures provided that the temperature is below 1000 K.

7.3 Conclusions

We investigated using liquid quench simulations the origin of the ability of Si to reduce the stress generated in S-B-C-N films by argon. The simulations show that S-B-C-N has a preference for a completely homogeneous structure in the absence of argon. When Ar atoms were included in the simulation, we observed the segregation of a Si-rich phase around them. We propose that the driving force for the segregation is the energy advantage gained by surrounding Ar atoms with longer and more flexible Si-containing bonds. This explains the ability of Si to inhibit the extra stress, otherwise generated by implanted Ar in S-B-C-N materials with zero or low Si content.

The incorporation of argon in the simulations caused major changes in the bonding preferences of all the atoms in the network. For example, all atoms showed a preference for bonding to nitrogen in the absence of Ar, whereas they showed a general increase in bonding to silicon when argon is present.

Based on the simulations, we make the prediction that the effectiveness of silicon to relieve stress in S-B-C-N films sputtered in argon will increase with deposition temperature up to approximately 1000K.

7.4 References

1 J. Houška, O. Warschkow, M.M.M. Bilek, D.R. McKenzie, J. Vlček and Š. Potocký, J. Phys.: Condens. Matter **18**, 2337 (2006).

2 W.D. Sproul, J.E. Greene et al. (ed.), Physics and Chemistry of Protective Coatings (American Institute of Physics, New York, 1986) pp 56-58.

3 C.A. Davis, Thin Solid Films **226**, 30 (1993).

4 S. Ulrich, T. Theel, J. Schwan and H. Ehrhardt, Surf. Coat. Technol. **97**, 45 (1997).

5 D.S. Franzblau, Phys. Rev. B **44,** 4925 (1991).

8 Comparison of measured and calculated characteristics of Si-B-C-N materials and the role of individual elements in them

This chapter compares characteristics of the simulated networks with related experimental results. They are compared in order to explain the experimental results where possible, and to show the power and limits of the simulation method used. The chapter is divided into sections focusing on:

(1) bonding statistics and related information.
(2) characteristics related to hardness.
(3) thermal stability.
(4) optical conductivity and band gap.

8.1 Structural and bonding data

In this section, various structural and bonding data are shown and discussed. Simulations were performed for samples of compositions:

- $Si_{32}B_8C_6N_{54}$ and $Si_{11}B_{14}C_{39}N_{36}$: representing typical compositions deposited with various sputtered targets.
- $Si_{31}B_8C_9N_{46}Ar_6$ (U_b = -100 V) and $Si_{31}B_8C_{13}N_{46}Ar_2$ (U_b = -500 V): representing similar compositions deposited with same sputtered target and different substrate bias voltage, U_b.

8.1.1 Related theory - calculation of bulk modulus

In 1985 Cohen[1] published the following empirical formula which describes very well the dependence of bulk modulus B on averaged coordination number N_c, bond length a_0 and bond ionicity λ:

$$B = \frac{\langle N_C \rangle}{4}(1971 - 220\lambda)a_0^{-3.5} \qquad \text{(Eq. 8.1)}$$

Although the formula was primarily derived for crystalline materials, qualitative predictions based on differences in N_c, a_0 and λ can be made also for amorphous materials.

While N_c and a_0 can be directly calculated from the simulated network structures, λ is to be derived from positions of Wannier function centres, which define the bonds. We simulated networks of several known crystalline materials containing elements from the IVA group (cubic and wurzite SiC) and IIIA + VA group (cubic and wurzite BN, cubic AlP and wurzite AlN) and observed the quantity $\Lambda = d_1r_2/d_2r_1$. Here, $d_{1(2)}$ are distances of the first(second) atom from the Wannier centre defining the bond between them, and $r_{1(2)}$ are covalent radii of the atoms[2].

material	λ	Λ
c-SiC	0	1.32
w-SiC	0	1.28
c-BN	1	1.73
w-BN	1	1.69
c-AlP	1	1.69
w-AlN	1	1.97

Table 8.1: *Ionicities of bonds in materials according to Cohen's definition (λ) and to positions of calculated Wannier function centres ($\Lambda = d_1r_2/d_2r_1$).*

In order to calculate the bond ionicity λ, we use a simple linear relation between λ and Λ:

$$\lambda = (\Lambda - 1)/(\Lambda_0 - 1) \qquad \text{(Eq. 8.2)}$$

According to the averaged results summarized in table 8.1 we set $\Lambda_0 = 1.7$. This formula gives the following results, in agreement with Cohen's definition (1,2) or experimental experience (3):

(1) $\lambda = 0$ for purely covalent homonuclear bonds (i.e. with a Wannier centre exactly in the middle of the bond).

(2) $\lambda \cong 1$ for bonds between elements from IIIA and VA group.

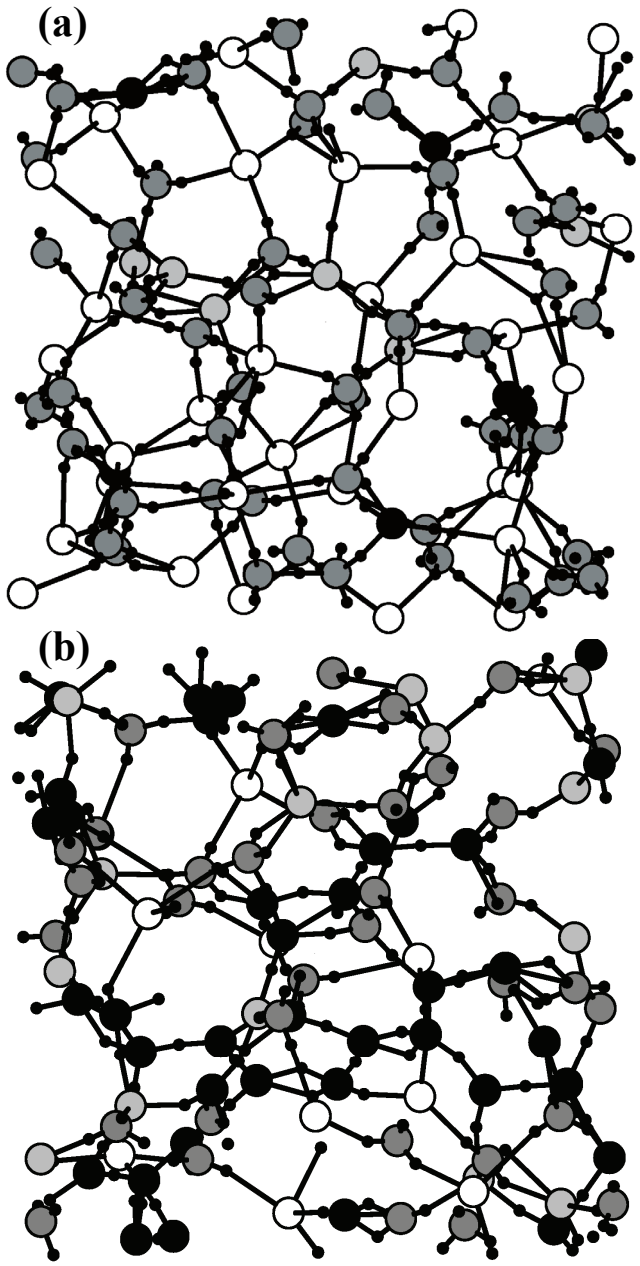

Fig. 8.1: *Snapshots from the liquid-quench simulation of a Si-B-C-N material of composition $Si_{32}B_8C_6N_{54}$ (panel a) and $Si_{11}B_{14}C_{39}N_{36}$ (panel b). Large black circles are C, dark grey are N, light grey are B, white circles correspond to Si, the small black dots represent Wannier function centres (WFCs).*

(3) $\lambda \cong 0.4$ for bonds in Si-C which is a group-IVA material, but partially ionic and often considered (c-SiC) to be part-way between a group-IV covalent and an III-V ionic semiconductor[1].

8.1.2 Bonding statistics as a function of elemental composition

Typical Si-B-C-N structures that are obtained at the end of the exponential cooling and subsequent equilibration runs are shown in Figs. 8.1(a) - composition $Si_{32}B_8C_6N_{54}$ and 8.1(b) - $Si_{11}B_{14}C_{39}N_{36}$. There is a prevalence of single bonds in the high-Si/C composition (Fig. 8.1(a)) structure compared to the low-Si/C composition (Fig. 8.1(b)) structure, where there are many more double bonds and also number of triple (C≡N) bonds.

Another phenomenon that can be observed in Fig. 8.1 is that the position of bonding Wannier function centres (WFCs) is often far from geometrical centre of the bond. In particular, positions of WFCs in Si-containing bonds (with atoms other than Si) are far from Si atoms (more than what would be expected due to the higher covalent radius of Si) and close to the other atoms. On the contrary, the WFCs are often close to N in the N-containing bonds. Both of these phenomena are illustrated in tables 8.2 and 8.3.

	bonds in $Si_{32}B_8C_6N_{54}$			bonds in $Si_{11}B_{14}C_{39}N_{36}$		
atom pair	single	double	triple	single	double	Triple
Si Si	1.7	0.0	0.0	1.0	0.0	0.0
Si B	1.0	0.0	0.0	0.0	0.0	0.0
Si C	3.0	0.0	0.0	11.2	0.0	0.0
Si N	110.6	7.4	0.2	30.1	0.6	0.0
B Si	1.0	0.0	0.0	0.0	0.0	0.0
B B	0.0	0.0	0.0	0.0	0.0	0.0
B C	0.0	0.0	0.0	16.3	0.0	0.0
B N	14.0	9.0	0.0	22.1	7.3	0.0
C Si	3.0	0.0	0.0	11.2	0.0	0.0
C B	0.0	0.0	0.0	16.3	0.0	0.0
C C	0.0	1.0	0.0	17.4	9.8	0.0
C N	4.0	6.2	0.8	22.4	8.4	4.4
N Si	110.6	7.4	0.2	30.1	0.6	0.0
N B	14.0	9.0	0.0	22.1	7.3	0.0
N C	4.0	6.2	0.8	22.4	8.4	4.4
N N	2.0	0.0	0.0	1.0	0.0	0.0

Table 8.2: *Bonding statistics of simulated Si-B-C-N samples of compositions $Si_{32}B_8C_6N_{54}$ and $Si_{11}B_{14}C_{39}N_{36}$. Data are averaged over 69 snapshots collected during a 0.5 ps production run.*

Table 8.2 includes complete bonding statistics for the Si-B-C-N samples of compositions $Si_{32}B_8C_6N_{54}$ and $Si_{11}B_{14}C_{39}N_{36}$ studied. The non-integer numbers result from averaging of the results over 69 snapshots collected during 0.5 ps production runs. Numbers of bonds of same kind and order change not only due to the bond-breaking processes (relatively rare at the low temperatures of production runs), but also due to the converting of a bond between permanently bonding atoms from double to single/triple state and vice versa.

The flipping process during which a bonding WFC alternates between two different atom pairs is discussed in detail in Ref. 3.

The table 8.2 shows that the most populated bonds in the high-Si/C composition are Si-N (mostly single), followed by B-N (single and double) and C-N (all bond orders). In the low-Si/C composition, other bond kinds have to be taken into account: C-Si (single), C-B (single) and C-C (single and double). The higher preference of carbon (in comparison with silicon) to form double and triple bonds leads to lower coordination numbers of sp^2- and sp-hybridised C atoms and therefore to lower bulk moduli (which indicates lower hardness) of the low-Si/C Si-B-C-N materials. The phenomena shown are in accordance with experimental observations (see measurements of hardness and bonding structure in chapter 3). Note that longer Si-containing bonds in the high-Si/C composition would on the contrary decrease the bulk modulus ($B \sim 1/d^{3.5}$ in the Cohen's formula for crystalline materials), but according to the experimental results the dependence of B on d is much weaker in amorphous materials.

8.1.3 Elemental bonding trends explained in terms of valence electrons and electronegativity

(a)

Sample	coord. Si	coord. B	coord. C	coord. N
$Si_{32}B_8C_6N_{54}$	3.9	3.0	2.7	2.9
$Si_{11}B_{14}C_{39}N_{36}$	4.0	3.3	3.0	2.7

(b)

Sample	charge Si	charge B	charge C	charge N
$Si_{32}B_8C_6N_{54}$	0.25±0.06	0.02±0.03	0.05±0.08	-0.16±0.07
$Si_{11}B_{14}C_{39}N_{36}$	0.26±0.06	0.00±0.04	-0.01±0.09	-0.07±0.07
	el.neg. Si	el.neg. B	el.neg. C	el.neg. N
	1.90	2.04	2.55	3.04

Table 8.3: *Structural characteristics of simulated Si-B-C-N samples of compositions $Si_{32}B_8C_6N_{54}$ and $Si_{11}B_{14}C_{39}N_{36}$. Data are averaged over 69 snapshots collected during a 0.5 ps production run. Part (a) shows averaged coordination numbers of the atoms of each element. Part (b) shows averaged atomic charges (in e) and their standard deviations for atoms of each element, together with their electronegativities.*

Table 8.3(a) shows the bonding behaviour of element in terms of their averaged coordination numbers. Table 8.3(b) shows averaged charges of atoms of the constituent elements, together with values of their Pauling electronegativity[2].

- The average coordination number of Si, which has 4 valence electrons and forms mainly single bonds, is close to 4. The average charge on Si atoms is positive at around 0.25e. This is in accordance with its relatively low electronegativity, confirmed also by the observed tendency of WFCs (negatively charged electron pairs) in Si-containing bonds to be far from the Si atoms (see Fig. 8.1).
- The average coordination number of B (with 3 valence electrons) is close to 3 despite the number of double B=N bonds, which increases the number of bonding electrons associated with B atoms to over 3. The boron atomic charge is nevertheless close to zero due to the strongly ionic character of B-N and especially B=N bonds (where both WFCs are close to the N atom).

- The average coordination number of C, with 4 valence electrons, is around 3 due to the number of double and triple C-containing bonds. The average charge on the C atoms is close to zero as it is for B, but the deviation is significantly higher (the highest of all atom types). This is due to two different "ionicity directions" of C-containing bonds (the WFCs are closer to C in bonds with Si and B and far from C in bonds with N). The wide range of hybridisations (number of associated WFCs) adopted by C is another reason for the large fluctuations in charge on the carbon atoms. An extreme example of this is a carbon atom associated with 6 WFCs which form 2 C≡N bonds (see top part of Fig. 8.1(b)), which has however one of the highest *positive* carbon charges of 0.129e because all 6 WFCs are far from the C atom and close to the respective N atoms.
- The average coordination number of N, with 5 valence electrons, is slightly less than 3. This is due to the fact that most of N atoms are associated with one non-bonding WFC (*lonepair*), which reduces averaged number of bonding WFCs associated with N atoms to 3. The average charges on N atoms are negative. The total negative charge on all N atoms is close to the total positive charge on all the Si atoms. This is in accordance with N having the highest relative electronegativity, illustrated also by the proximity of WFCs to N atoms in the N-containing bonds (with atoms other than N).

bond	our ionicity Λ	Cohen's ionicity λ
Si – Si	1.1	0.1
$Si^+ – C^-$	1.3	0.4
$Si^+ – N^-$	1.7	1.0
$Si^+ = N^-$	2.1	1.6
$B^+ – C^-$	1.4	0.6
$B^+ – N^-$	1.7	1.0
$B^+ = N^-$	2.4	2.0
C – C	1.05	0.1
C = C	1.2	0.3
$C^+ – N^-$	1.3	0.4
$C^+ = N^-$	1.7	1.0
$C^+ \equiv N^-$	1.7	1.0
N – N	1.05	0.1

Table 8.4: *Typical ionicity of bonds in simulated Si-B-C-N materials according to Cohen's definition (λ) and to positions of calculated Wannier function centres ($\Lambda = d_1r_2/d_2r_1$). Bonds with negligible or zero population in all samples simulated are not included. In heteronuclear bonds the WFC(s) is (are) closer to the atom with minus in superscript.*

Table 8.4 includes exact ionicities of all bonds with non-negligible population in at least one of all simulated Si-B-C-N samples. It was found that their averaged values do not depend significantly on sample composition. The most significant findings are:

- behaviour of the atoms is in agreement with their electronegativities (see table 8.3).
- the homonuclear bonds are not exactly covalent in amorphous materials: $\lambda = 0.1$-0.3.
- ionicities of heteronuclear single bonds are in the range $\lambda = 0.4$-1.0.
- ionicities of heteronuclear double bonds are in the range $\lambda = 1.0$-2.0.
- ionicities of all double bonds are higher than ionicities of equivalent single bonds.

- in accordance with the definition of λ, the single and double B–(=)N bonds (elements from IIIA and VA group) are the most ionic of all single (double) bonds, followed closely by the Si–(=)N bonds. The C-containing bonds have relatively low ionicities, but the effect which this should have of increasing bulk modulus will be offset by the high proportion of double and even triple C-containing bonds.

8.1.4 Bonding statistics as a function of U_b

(a) Sample	coord. Si	coord. B	coord. C	coord. N
$Si_{31}B_8C_{13}N_{46}Ar_2$ [-100 V]	3.90	3.24	3.03	2.82
$Si_{31}B_8C_9N_{46}Ar_6$ [-500 V]	3.85	3.10	3.03	2.79

(b) Sample	coord.	bond length (Å)	our ionicity Λ	Cohen's ionicity λ
$Si_{31}B_8C_{13}N_{46}Ar_2$ [-100 V]	3.22	1.7454	1.56	0.80
$Si_{31}B_8C_9N_{46}Ar_6$ [-500 V]	3.18	1.7311	1.64	0.91
effect on B (%)	1.1	-2.9	1.4	

Table 8.5: *Structural characteristics of simulated Si-B-C-N samples of compositions $Si_{31}B_8C_{13}N_{46}Ar_2$ (U_b = -100 V) and $Si_{31}B_8C_9N_{46}Ar_6$ (U_b = -500 V). Part (a) shows changes in averaged coordination numbers of individual atoms. Part (b) shows changes in averaged total coordination number (without Ar), bond length and bond ionicity, and effect of these changes on bulk modulus using Cohen's formula for crystalline materials.*

Table 8.5 quantifies the effect of observed structural characteristics on bulk moduli of $Si_{31}B_8C_{13}N_{46}Ar_2$ (deposited with U_b = -100 V which led to relatively low content of implanted Ar; simulated with cooling time of 100 fs) and $Si_{31}B_8C_9N_{46}Ar_6$ (deposited with U_b = -500 V which led to relatively high content of implanted Ar and to decreased C content due to the stronger sputtering of loosely bounded C-N compounds[4,5]; simulated with cooling time of 500 fs).

Table 8.5(a) shows that the averaged coordination numbers of all atoms except carbon increase at shorter cooling time (lower $|U_b|$ and consequently lower Ar content). The coordination number of carbon is unaffected. The increase is most significant for boron, which correlates with experimentally predicted existence of an energy window for preferential formation of B(sp^3)-N bonds at low $|U_b|$ in BN[6] and Si-B-C-N (see chapter 4) materials.

Table 8.5(b) shows the effect of substrate bias (and consequent Ar content) on total averaged coordination number, bond length and bond ionicity. It can be seen that:

- the material prepared with lower $|U_b|$ possesses higher total averaged coordination number and lower averaged bond ionicity (see generally lower ionicities of single bonds in table 8.4). This would be expected to have a positive effect on its bulk modulus.
- because single bonds are always longer than equivalent double bonds, it can be seen that in the low $|U_b|$ material the averaged bond length is higher. This would be expected to have a negative effect on its bulk modulus.
- the last row of table 8.5 shows that according to the Cohen's formula, individual effects of all discussed structural differences on bulk modulus are up to 3%, and collectively their effect is close to zero. Note that the formula used was developed for

a particular class of crystalline material and can therefore provide only a rough guide for amorphous materials. However, it is clear that calculated structural differences (despite significant differences in cooling times used and numbers of implanted Ar atoms considered) cannot fully explain the experimentally observed differences in mechanical properties of these materials of similar Si-B-C-N compositions deposited under different conditions.

8.1.5 Conclusions

The most populated bonds in the high-Si/C composition structures were found to be Si-N (mostly single), B-N (single and double) and C-N (all bond orders). In the low-Si/C composition structures, other bond types: C-Si (single), C-B (single) and C-C (single and double) also become significant.

A method to calculate bond ionicities, λ, using WFCs was developed. Typical values were 0.1-0.3 for homonuclear bonds, 0.4-1.0 for heteronuclear single bonds and 1.0-2.0 for heteronuclear double bonds. According to the experimental results, the coordination numbers (higher for Si than for C) have a more significant effect on the hardness of materials of different Si-B-C-N composition than do the bond lengths and ionicities.

A simulated sample deposited with low $|U_b|$ possessed higher averaged total coordination number at lower bond ionicity and higher bond lengths than the equivalent high $|U_b|$ simulated structure. Quantitatively, differences in these quantities alone cannot explain the experimentally observed differences in mechanical properties of these samples of similar Si-B-C-N composition.

8.2 Hardness

Section 8.1 showed that differences in quantities such as coordination number or bond ionicity cannot fully explain differences in hardness of materials of similar elemental compositions deposited in various N_2-Ar gas mixtures or with different values of substrate bias. In this section we show that variations in the amount of implanted Ar could be responsible for the differences in hardness. The amount of implanted Ar depends both on the N_2-Ar gas mixture and the bias U_b, while, for example, the densification of material due to an ion bombardment takes place at any gas mixture composition. Simulations were performed for samples of compositions:

- $Si_{32}B_{10}C_6N_{52}Ar_6$ (U_b = -500 V, result is repeated with new comments from the previous chapter 7).
- $Si_{31}B_8C_{13}N_{46}Ar_2$ (U_b = -100 V) and $Si_{31}B_8C_9N_{46}Ar_6$ (U_b = -500 V).

8.2.1 An explanation for enhanced hardness based on simulations

Although there is no method available for the direct calculation of hardness, structural phenomena potentially affecting the hardness can be examined. In particular, Fig. 8.2 compares segregation of Si around implanted Ar atoms in a sample of composition $Si_{32}B_{10}C_6N_{52}Ar_6$ (panel (a) - see the discussion in the previous chapter 7) with the hardness of three Si-B-C-N samples of similar compositions after their annealing and cooling down to the room temperature. All three samples shown in Fig. 8.2(b) were deposited at high Ar content in a N_2-Ar gas mixture (1:3), which led to relatively high contents of implanted Ar. The other deposition conditions were $C_{20}Si_{60}B_{20}$ sputtered target, U_b = -100 V and T_s = 350°C (squares), $C_5Si_{75}B_{20}$ sputtered target, U_b = -100 V and T_s = 350°C (circles) and $C_5Si_{75}B_{20}$ sputtered target, $U_b = U_f$ and $T_s \leq 190$°C (triangles).

Segregation of Si around implanted Ar atoms leads to the formation of a sort of two-phase material, consisting of amorphous Si-rich and Si-poor regions. We believe that this can lead to an increase in the extrinsic hardness, in the same way as described previously for mixtures of two nanocrystalline or nanocrystalline and amorphous materials (see, for example, Ref. 7). It can be seen in Fig. 8.2 for all three samples shown that the "extra hardness" which the material obtains (or loses) due to the annealing has entirely the same temperature dependence as the segregation of Si around Ar, which takes place due to its activation at high temperatures. These results collectively suggest that annealing of Si-B-C-N materials containing implanted Ar can lead to changes in their hardness due to the segregation of Si around the Ar-containing cavities. This increases with temperature up to 1000 K, and then starts to decrease above 1500 K where high kinetic energies start to inhibit a stable segregation (see the discussion in previous chapter 7).

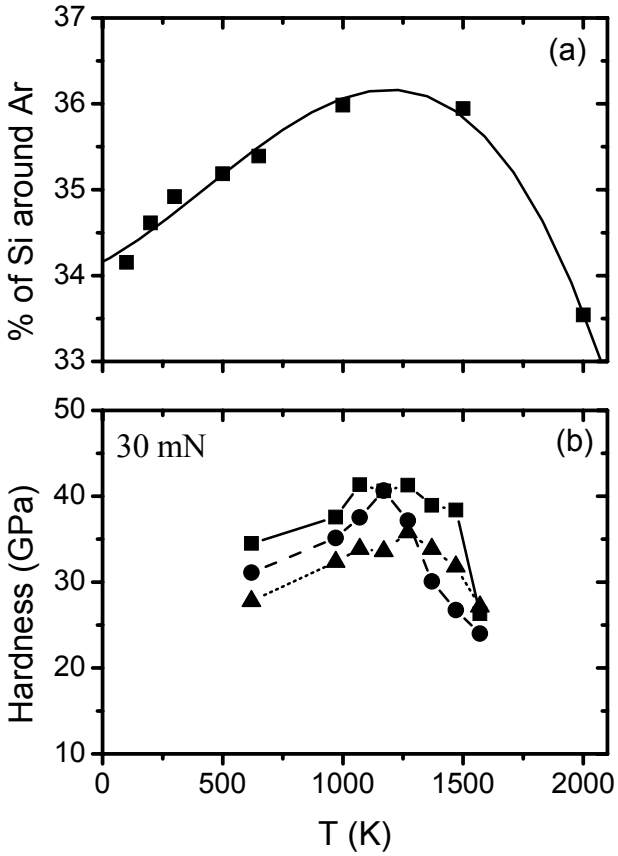

Fig. 8.2: *Panel (a) (repeated from the previous chapter 7 for reader's convenience) shows segregation of Si around implanted Ar atoms in samples of composition $Si_{32}B_{10}C_6N_{52}Ar_6$ equilibrated at various temperatures. The vertical axis refers to the percentage of Si atoms in the group of Si, B, C and N atoms that lie in the vicinity of an Ar atom. Panel (b) shows dependence of hardness of three Si-B-C-N films (of similar compositions as the simulated one), measured after annealing and cooling back to the room temperature, as a function of the annealing temperature.*

Figure 8.3 shows the segregation phenomenon in detail for two samples with different Ar contents of 2 and 6% (this is the same pair of samples which was used for examining of the effect of U_b in the previous section 8.1). The samples are $Si_{31}B_8C_{13}N_{46}Ar_2$ (deposited with U_b = -100 V) and $Si_{31}B_8C_9N_{46}Ar_6$ (deposited with U_b = -500 V). In the sample containing 6% Ar, shown on the right side of Fig. 8.3, most of the network atoms have at least one implanted Ar atom at a distance of ≤ 4 Å (upper bound of first peaks of the dependences - the limit is slightly higher than 3.6 Å in the previous chapter probably due to a different atomic density). In contrast, in the sample containing 2% Ar, shown on the left side of the figure, the distances to the nearest Ar atom span a wide range with most distributions showing several comparable peaks up to the maximum possible distance imposed by the periodic simulation cell.

We define the Si-rich regions (in close proximity to Ar atoms) as those which consist of atoms in the first peaks in Fig. 8.3, they fill space between two concentric spheres of radii 2.5 and 4 Å around each implanted Ar (space around each Ar atom up to approximately 2.5 Å is empty according to Fig. 8.3). The spheres can of course intersect especially at high Ar

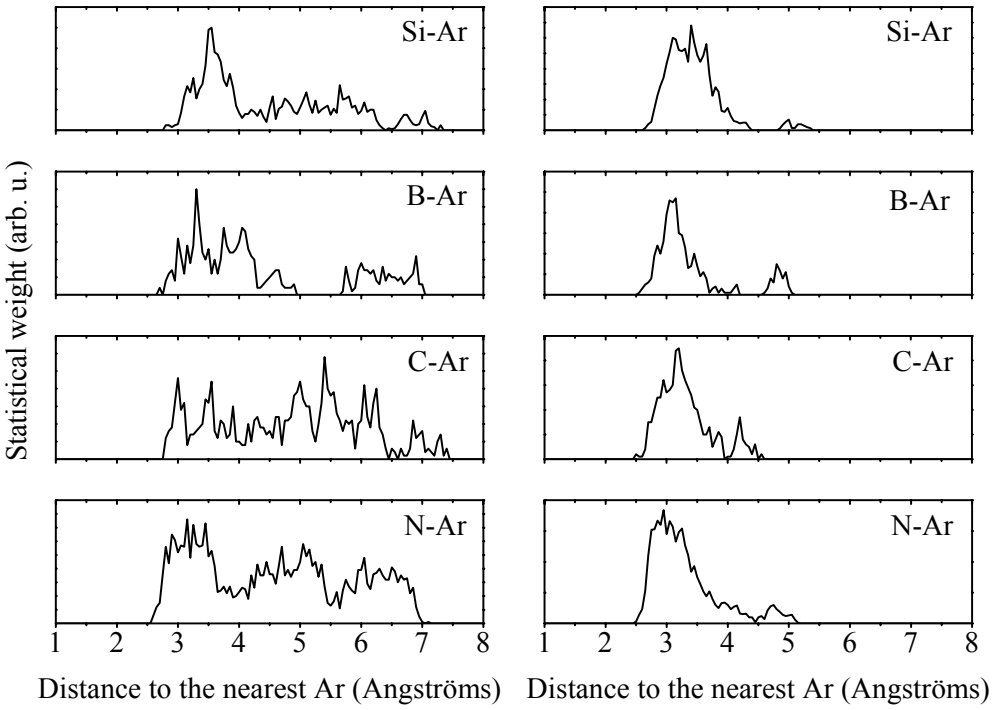

***Fig. 8.3**: Distributions of distances of Si,B,C and N atoms to the nearest Ar atom in samples $Si_{31}B_8C_{13}N_{46}Ar_2$ (left) and $Si_{31}B_8C_9N_{46}Ar_6$ (right). Data are summed over all atoms of the respective element and over the 69 snapshots made during the 0.5 ps production run at the end of the liquid-quench simulation. In the latter sample, most of atoms are close to at least one Ar. In the Si-Ar distributions, relatively more of the distances are in the lower part of the range.*

content. The rest of the sample constitutes the Si-poor matrix (away from the Ar atoms). In the 6% Ar sample, because of the high density of Ar, most of the constituent atoms are included in "high-Si" regions in close proximity to Ar (where therefore the Si content can not be increased very much). This results in an almost homogenous material. In the 2% Ar sample, the Ar density is low enough to allow segregation into close-to-Ar Si-rich regions and far-from-Ar Si-poor regions. The proportions of these two different composition zones are fairly balanced, suggesting the formation of a true heterogenous material.

sample composition	composition of regions	ratio of regions
$Si_{31}B_8C_{13}N_{46}Ar_2$ (low |Ub|)	around Ar: $Si_{37}B_{10}C_9N_{44}$	41.7 %
	rest : $Si_{28}B_7C_{16}N_{49}$	58.3 %
$Si_{31}B_8C_9N_{46}Ar_6$ (high |Ub|)	around Ar: $Si_{34}B_8C_{10}N_{48}$	90.1 %
	rest : $Si_{22}B_{12}C_{10}N_{56}$	9.9 %

***Table 8.6**: Column 2 shows compositions of regions, which result from segregation of Si in vicinity of implanted Ar in $Si_{31}B_8C_{13}N_{46}Ar_2$ and $Si_{31}B_8C_9N_{46}Ar_6$ structures. Column 3 shows the relative sizes of the regions (in proportion of atoms included). Atoms in the vicinity of an Ar atom are defined to be those which are closer than 4 Å to an Ar atom.*

The ideas presented above are quantified in table 8.6. The table confirms that:

- in the 2%-Ar sample, comparable numbers of all network atoms are included in the close-to-Ar and far-from-Ar zones (42 and 58 %, respectively). The Si enrichment around Ar atoms is consequently relatively high in comparison with the other sample.
- in the 6% Ar sample, 90 % of all network atoms are included in the close-to-Ar zones. The Si-enrichment is therefore relatively low there, despite significant reduction of Si-content in the far-from-Ar rest of the sample.

Figure 8.4 contains schematic diagrams of the structures with 2% Ar and 6% Ar to illustrate the segregation concepts discussed above. The dark grey tone represents regions with higher Si. The left side of Fig. 8.4 shows the situation in the sample with 2% of implanted Ar. The dark-grey halos represent spheres containing atoms in close proximity to Ar with a silicon content of 37%, while the light-grey matrix depicts the atoms in the far-from-Ar zone which has a silicon content of 28%. On the right side of Fig. 8.4, the middle-grey halos represent spheres around implanted Ar atoms, with 34% silicon content, in the far-from-Ar white matrix with only 22% silicon content. The figure is simplified by the assumption that all Ar atoms considered lie in a plane parallel to the plane of the figure, which leads to unified halo radii. Ratios of dark and light areas in both figures refer to calculated ratios of close-to-Ar and far-from-Ar zones in both samples (42:58 and 90:10, respectively), in order to demonstrate difference between the two structures (heterogenous 2%-Ar materials on the left, almost homogenous 6%-Ar material on the right).

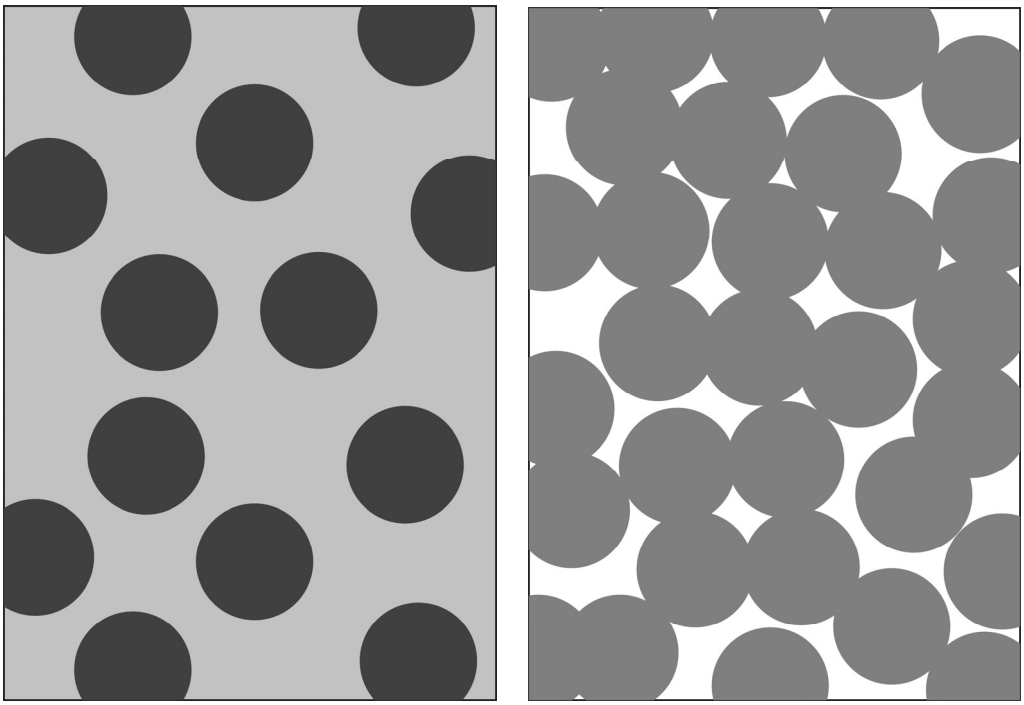

Fig. 8.4*: A schematic diagram based on the simulations of structures of the samples* $Si_{31}B_8C_{13}N_{46}Ar_2$ *(left) and* $Si_{31}B_8C_9N_{46}Ar_6$ *(right). Darker gray tones represent higher Si content in the respective zone of a material. The halos refer to spheres with an Ar atom in the middle (*$r \cong 4$ *Å) with enhanced Si content. Ratios of dark and light areas in both figures approximately correlate to calculated ratios of the sizes of close-to-Ar and far-from-Ar zones in both samples (42:58 and 90:10, respectively)*

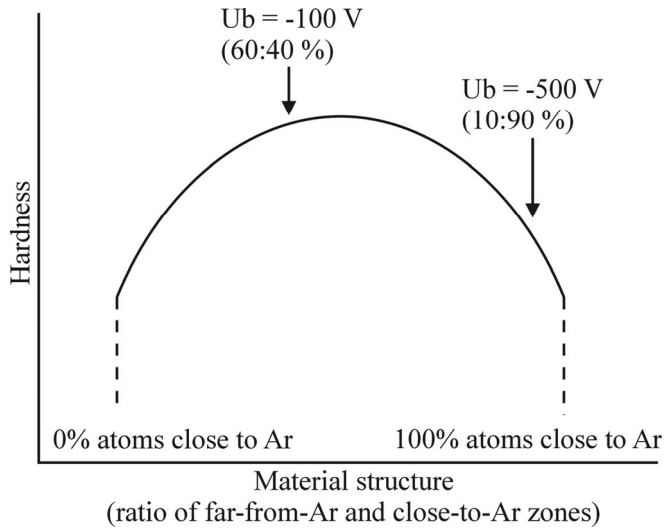

Fig. 8.5: *Qualitative dependence of hardness of a two-phase material on relative volumes of the phases, and positions of samples $Si_{31}B_8C_{13}N_{46}Ar_2$ and $Si_{31}B_8C_9N_{46}Ar_6$ in this dependence. Ratios of far-from-Ar to close-to-Ar zones of different compositions are taken from table 6.*

Figure 8.5 demonstrates the effect of the phenomenon described above on the relative hardnesses of the samples with 2% Ar and 6% Ar. For simplicity, we assume in the figure that the Si-rich and Si-poor zones have the same values of hardness in both samples. The curve depicted in figure 8.5 is based on the finding that the hardness of a mixture of nanograins of two materials is at their proper ratio higher than the hardnesses of both constituents even when they are significantly different[7]. Furthermore, it is considered in Fig. 8.5 that the dependence of hardness of the mixture of the Si-rich and Si-poor regions on their volume ratio is roughly symmetrical, having a maximum value at a ratio of 50%:50%. The 42%:58 % ratio calculated for the 2% Ar material (see table 8.6) leads to significantly higher extrinsic hardness than the 90%:10% ratio calculated for the 6% Ar material.

8.2.2 Supporting experimental results

In this subsection, our conclusion concerning the effect of the implanted Ar concentration and the segregation of Si around Ar on hardness is examined in the light of two additional experimental results. These results show that both the silicon content (Fig. 8.6) and the argon content (Fig. 8.7) are important for the hardening of the in Si-B-C-N materials.

Figure 8.6 shows the effect of deposition temperature on hardness at various sputtered target compositions. Two series of (Si)-B-C-N samples were deposited using the B_4C-Si target at substrate temperatures T_s = 700 °C and T_s < 190 °C (no ohmic heating). The other deposition conditions were 25% N_2 + 75% Ar gas mixture and U_b = -100 V. Absolute values of the hardness of the samples are shown in figure 8.6(a), hardness differences caused by increases in T_s from less than 190 to 700 °C are shown in figure 8.6(b). It can be seen that while this difference is negative (that is, samples deposited with lower T_s are harder) at zero or low Si fraction in erosion target area, it increases almost linearly with increasing Si fraction in erosion target area over the whole range observed, becoming positive when the Si fraction is above ~30%. Them slope of the increase caused by T_s is approximately (11 GPa) / (75% Si in erosion target area)(500°C) ≅ 0.3 MPa per 1°C and 1% Si in erosion target area.

The figure 8.6 can be understood taking into account that the physical processes determining hardness are different for films with low Si content compared to those with high Si content. In the first case, when Si content is low, the compressive stress caused by implanted Ar atoms cannot be relaxed by segregation of Si around them and films deposited at low temperatures show high intrinsic stress and this compressive stress leads to high values of hardness. The intrinsic stress can be relieved by atomic rearrangement if deposition is carried out at elevated temperature (T_s = 700 °C). With increasing Si content, the thermally activated stress relaxation becomes less important because the compressive stress caused by implanted Ar is relieved by segregation of Si around Ar. The main process increasing material hardness at high Si content is therefore the segregation of the material into nanoscale regions of two phases. This thermally activated segregation process is naturally more significant at higher T_s (up to ~1000K, as shown previously), and at higher Si content in materials and it leads to an increase in hardness with deposition temperature at high Si content.

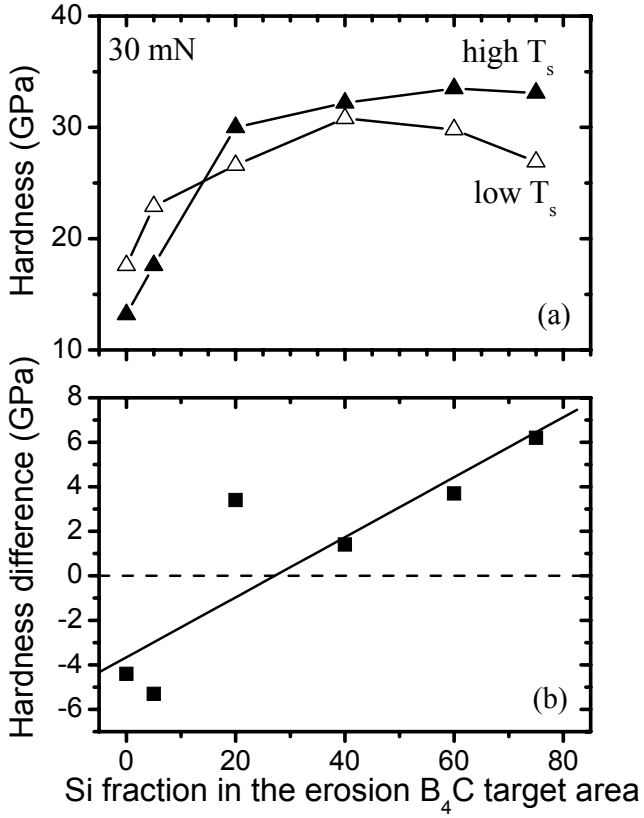

Fig. 8.6: *Panel (a) shows hardness of Si-B-C-N samples deposited using a B_4C-Si sputtered target at high substrate temperature T_s = 700 °C (full symbols) and low T_s < 190 °C (no ohmic heating - empty symbols). The other deposition conditions were 25% N_2 + 75% Ar gas mixture and U_b = -100 V. Panel (b) shows differences of values shown in panel (a): hardness at T_s = 700 °C - hardness at T_s < 190 °C. The line is a fit from linear regression.*

Figure 8.7 shows the hardness as a function of Ar content in the gas mixture for two series of Si-B-C-N sample, deposited at U_b = -100 and -500 V with sputtered target composition $(B_4C)_{25}Si_{75}$ and substrate temperature T_s = 350°C. Absolute values of the hardness are shown in figure 8.7(a), while hardness differences caused by change of U_b from -500 V to -100 V are shown in figure 8.7(b). It can be seen that while this difference is negative (that is, samples deposited with U_b = -500 V are harder) at zero or very minor Ar fraction in the gas mixture, it increases almost linearly with increasing Ar fraction in the gas mixture over the whole range observed, becoming positive at the 25% N_2 + 75% Ar gas mixture composition. The slope of the increase caused by U_b is thus approximately (15 GPa) / (75% Ar in gas mixture)(400 V) ≅ 0.5 MPa per 1 V and 1% Ar in gas mixture. Although this phenomenon was not so pronounced for samples deposited with the C-Si-B target (see chapter 3), it has been observed for all other $(B_4C)_xSi_{(100-x)}$ targets used at x > 0. On the contrary, the difference between hardness values at U_b = -100 and -500 V was almost constant at x = 0 (B-C-N samples).

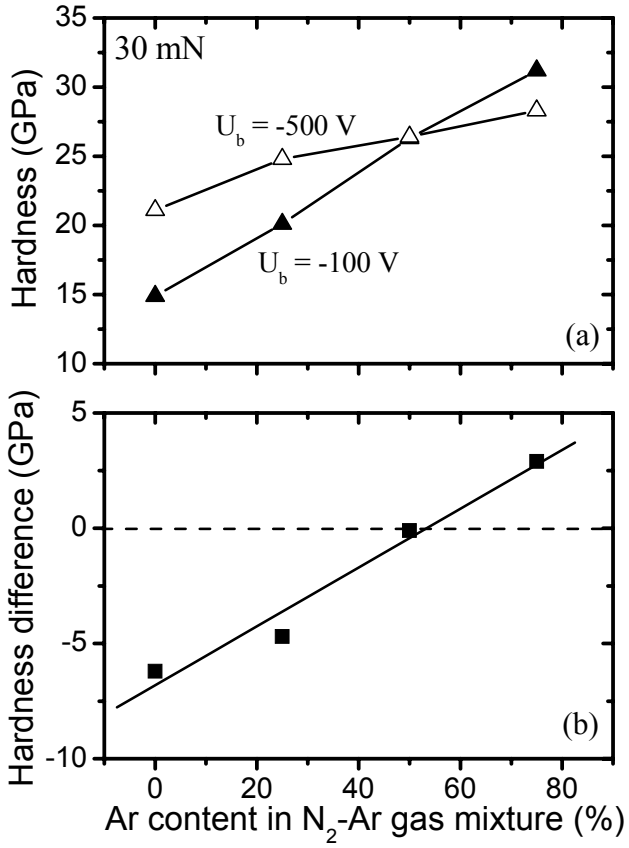

Fig. 8.7: *Panel (a) shows hardness of Si-B-C-N samples deposited using a B_4C-Si sputtered target at substrate bias U_b = -100 V (full symbols) and U_b = -500 V (empty symbols). The other deposition conditions were $(B_4C)_{25}Si_{75}$ sputter target and substrate temperature T_s = 350°C. Panel (b) shows differences of values shown in panel (a): hardness at U_b = -100 V - hardness at U_b = -500 V. The line is a fit from linear regression.*

The figure 8.7 can be understood taking into account that physical processes affecting material hardness are different at zero and at high Ar content in gas mixture (and therefore in deposited materials). In the first case, the hardness is higher for materials deposited at U_b = -500 V, possibly due to stronger bombardment by nitrogen ions which leads to ion-induced knock-on subplantation of other film-forming particles, resulting in densification of the deposited materials. The same behaviour was observed also for other amorphous materials such as CN_x[8] prepared in pure N_2. As can be seen in Fig. 8.7, the successive increase of material hardness with increasing Ar fraction in gas mixture (shown also in chapter 3) is much more pronounced at U_b = -100 V than at U_b = -500 V. Thus films deposited with high Ar fraction in gas mixture have higher hardness at U_b = -100 V than at U_b = -500 V (see also results in chapter 4). Our simulations indicate that the level of Ar incorporation in the films at high bias is too high to allow substantial Si segregation. Optimum segregation is facilitated for a few percent Ar incorporation as found in films deposited with -100V bias. The fact that this phenomenon was not observed for B-C-N materials with 0% Si content, supports the idea that the segregation of Si around Ar is responsible for the hardness enhancement in this case.

As formulated in the previous subsection 8.2.1., in the 6% Ar sample most of the atoms are included in the high-Si regions which leads to the formation of almost homogenous material, while in the 2% Ar sample, percentages of close-to-Ar Si-rich regions and far-from-Ar Si-poor regions are more balanced, suggesting formation of a true heterogenous material. Moreover, multiple thermal spikes melting the material (see in chapter 4 ~5 times higher [bombarding ions]/[film-forming particles] flux ratio at U_b = -500 V) can interrupt the segregation processes which take place during material equilibration (see chapter 7) and thus make any stable segregation more difficult.

8.2.3 Conclusions

Structures of samples deposited in an Ar-containing gas mixture at various U_b were examined by simulations. Analysis of the simulation results was focused on the formation of Si-rich regions around implanted Ar atoms. It was found that the 6% Ar sample (U_b = -500 V) is not far from homogenous (most of the network atoms are close to at least one Ar), while the 2% Ar sample (U_b = -100 V) is heterogenous, with similar amounts of the close-to-Ar Si-rich regions and far-from-Ar Si-poor regions. This may lead to higher extrinsic hardness of the material deposited at lower $|U_b|$. The prediction was successfully tested against several experimental results.

8.3 Temperature stability

This section is based on results included in Ref. 9. Temperature stability of Si-(B)-C-N materials is examined by calculations of rate of N_2 formation and by calculations of bond lifetimes. Simulations were performed for samples of compositions:

- $Si_{11}B_{14}C_{39}N_{36}$ and $Si_{32}B_8C_6N_{54}$ (to examine the effect of Si/C ratio on bond lifetimes).
- $Si_{11}C_{53}N_{36}$ and $Si_{32}C_{14}N_{54}$ (to examine the effect of B on bonding and structural data, compared with the previous pair).
- $Si_{11}B_{14}C_{39}N_{44}$ and $Si_{11}C_{53}N_{44}$ (to examine the effect of B on rate of N_2 formation - same compositions were used for liquid quench simulations of samples $Si_{11}B_{14}C_{39}N_{36}$ and $Si_{11}C_{53}N_{36}$).
- $Si_{39}B_{14}C_{11}N_{44}$ and $Si_{53}C_{11}N_{44}$ (to examine the effect of Si/C ratio on rate of N_2 formation - fictitious pair of structures, obtained from the previous pair by replacing C by Si and vice versa).

8.3.1 Bond lifetimes

bond type	lifetimes at 1000 K (snapshots)	(%)	lifetimes at 2400 K (snapshots)	(%)
		Low Si/C		
Si-N	42	46	28	33
B-N	50	53	42	45
C-N	44	48	36	40
Si-C	40	47	31	37
B-C	38	42	33	40
C-C	51	52	40	42
		High Si/C		
Si-N	94	82	58	59
B-N	113	89	76	70
C-N	130	96	71	68

Table 8.7: *Lifetimes of bonds during 500 fs MD runs in low-Si/C sample of composition $Si_{11}B_{14}C_{39}N_{36}$, and in high-Si/C sample of composition $Si_{32}B_8C_6N_{54}$. Lifetimes are given in snapshots between forming and breaking of the bond (max. 138 snapshots with 3.6 fs interval between them), and as a percentage of the simulation time remaining after formation of the bond until end of the MD run. Only the most populated bonds are included.*

Table 8.7 shows lifetimes of bonds during 500 fs MD runs in a low-Si/C sample of composition $Si_{11}B_{14}C_{39}N_{36}$, and in a high-Si/C sample of composition $Si_{32}B_8C_6N_{54}$. Only the most populated bonds were considered in order to obtain statistically significant results: these being Si/B/C-N bonds in both samples, and Si/B/C-C bonds in the low-Si/C sample only. Lifetimes were examined at a relatively low temperature of 1000 K, and at a high temperature of 2400 K which is close to the highest reported thermal stability of Si-B-C-N materials (see chapter 1 and references therein). Conversion of a double or triple bond to a bond of lower order was not considered as breaking of that bond. Because the lifetimes of all bonds are artificially limited by the finite duration of the MD run, the results will generally be too low when given in fs, and too high when given as percentages of the simulation time remaining until the end of the MD run (especially for bonds formed short time before the end of the MD run). Nevertheless, both of these results, included in table 8.7, show the same trends.

The following can be deduced from the data in table 8.7:

- Bond lifetimes at same temperature are significantly higher for the high-Si/C material than for the low-Si/C material. This not only correlates with the previously observed higher thermal stability of the high-Si/C Si-B-C-N materials[5], but the significance of the difference indicates that it may be possible to use this method for making reliable predictions about the relative thermal stability of other amorphous materials.
- The significantly higher thermal stability of the high-Si/C material is further shown by the fact that the bond lifetimes in this material at 2400 K are not only higher then the bond lifetimes in the low-Si/C material at 2400 K, but also higher than the bond lifetimes in the low-Si/C material at 1000 K.
- On the average, lifetimes are slightly higher for C-N, C-C and B-N bonds than for Si-N, Si-C and B-C bonds. This is probably due to the fact the atom pairs from the latter group form mainly single bonds, while atom pairs from the first group often form also double or even triple bonds which are generally stronger than the equivalent single bonds.
- The fact that lifetimes of the Si-containing bonds are not longer (even slightly shorter) than lifetimes of the C-containing bonds in the same material indicates that the higher thermal stability of high-Si/C materials is based on deeper structural phenomena than simply a difference in types of atoms bonded. In particular, it shows that the bond lifetime is not constant for a particular atom pair but depends also on the local environment of the atoms bonded.

8.3.2 Rates of N_2 formation

It is known[10] that a main mass-loss process which limits temperature stability of Si-(B)-C-N materials is the outflow of nitrogen due to the decomposition reactions $Si_3N_4 + 3C \rightarrow 3SiC + 2N_2$ and $Si_3N_4 \rightarrow 3Si + 2N_2$. Figure 8.8 shows rates of N_2 formation in the low-Si/C samples $Si_{11}B_{14}C_{39}N_{44}$ and $Si_{11}C_{53}N_{44}$ and in the high-Si/C samples $Si_{39}B_{14}C_{11}N_{44}$ and $Si_{53}C_{11}N_{44}$. MD runs were performed after initial mixing of the low-Si/C pair of samples, while input structures of the latter pair of samples were obtained by replacing of all Si atoms by C atoms and vice versa (followed by optimising of a new wavefunction). Using the same N contents and atomic densities for all these samples ensure that the rate of N_2 formation depends only on the Si/C/B compositions. Note than although the atomic densities used for the fictitious high-Si/C compositions are therefore probably slightly overestimated and it was shown in chapter 5 that rate of N_2 formation can decrease as a result of higher coordination number at higher material density, the high-Si/C compositions simulated at experimental atomic densities (see e.g. section 8.1) have so high coordination numbers that they can hardly increase more as a result of higher atomic density.

As for the calculations described in chapter 5, a number of the N atoms start out statistically in close proximity and are therefore prone to form N_2 molecules immediately. This leads to up to 4 N_2 molecules at 1000 K where diffusion does not play a significant role in the N_2 formation - see Fig. 8.8(a). These N_2 molecules are not of relevance to the rate of N_2 formation due to diffusion and bond-breaking processes. Figure 8.8(b) therefore shows only the numbers of N_2 molecules formed by atoms which start far from each other in the initial (input) structure.

It can be seen from Fig. 8.8 that the numbers of N_2 molecules formed are significantly higher in the low-Si/C Si-(B)-C-N materials than in the equivalent (that is, with the same B and N contents and atomic densities) high-Si/C materials at all temperatures. This effect is stronger for Si-C-N than for Si-B-C-N materials, probably due to the difference in Si contents in the high-Si/C compositions $Si_{39}B_{14}C_{11}N_{44}$ and $Si_{53}C_{11}N_{44}$ (all B replaced by Si).

Figure 8.8(b) further shows that rate of N_2 formation due to the diffusion and bond-breaking processes is significantly lower for Si-B-C-N materials than for the equivalent Si-C-N materials. This correlates with the prediction[10] that the addition of B protects Si-C-N ceramics from decomposition via the reactions described above.

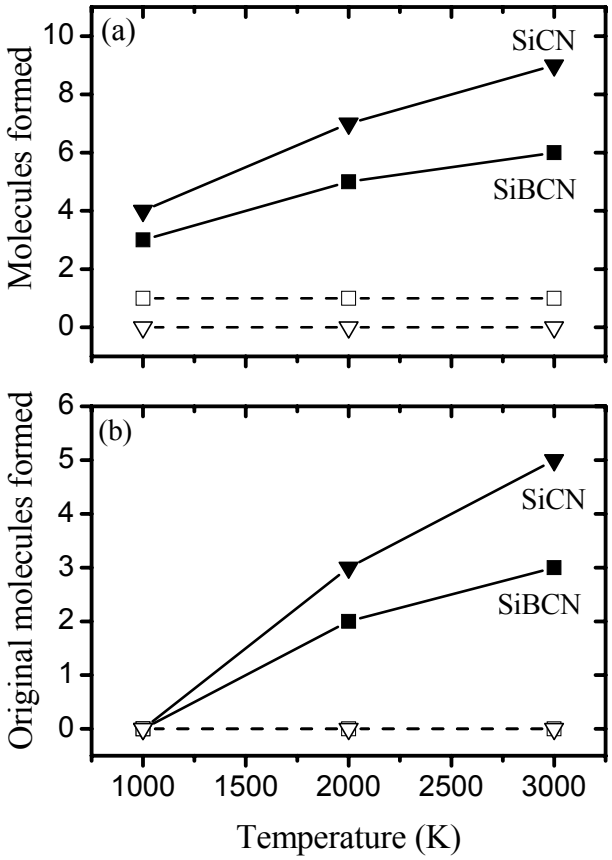

Fig 8.8: *Number of N_2 molecules formed in Si(B)CN samples during 500fs MD runs at various temperatures in low-Si/C samples ($Si_{11}B_{14}C_{39}N_{44}$ and $Si_{11}C_{53}N_{44}$ - full symbols) and in high-Si/C samples $Si_{39}B_{14}C_{11}N_{44}$ and $Si_{53}C_{11}N_{44}$ ($Si_{39}B_{14}C_{11}N_{44}$ and $Si_{53}C_{11}N_{44}$ - empty symbols). Panel (a) includes all N_2 molecules formed. Panel (b) includes only N_2 molecules which arise from N atoms that don't start out in close proximity to one another.*

8.3.3 Role of boron in the networks

	1000 K	2000 K	3000 K
surroundings of B	2C, 3N, 9CN	1C, 5N, 8CN	3C, 4N, 7CN
% of B sur. by C or N only	36	43	50
surroundings of Si	1N, 10CN	1C, 1N, 9CN	1N, 10CN
% of Si sur. by C or N only	9	18	9

Table 8.8: *The local environments of B and Si atoms in Si-B-C-N material of composition $Si_{11}B_{14}C_{39}N_{44}$ at the end of MD runs at 1000, 2000 and 3000 K. C, N and CN denote numbers of B/Si atoms bonded to C only, to N only and to both C and N, respectively. Results are shown in numbers of atoms (C, N and CN - upper rows) and in percentages of the total ([CN]/[C+N+CN] - lower rows).*

Table 8.8 shows the role of B in stabilizing the Si-B-C-N sample of composition $Si_{11}B_{14}C_{39}N_{44}$. The sample consists mainly of C and N, and at high temperatures it would therefore tend to form graphitic zones while simultaneously releasing N_2 molecules. Table 8.8 compares the behaviour of B during these processes with Si (the other minor element in this composition) by observing the local environment of each of these atoms. When there are no Si-Si, B-B and Si-B bonds in this composition, each Si and B atom can be bonded to N only, C only or to both C and N. It can be seen that most of the Si atoms are bonded to both C and N, which suggests that they typically form bridges between segregated zones of C (stable graphite) and N (unstable source of N_2 molecules). On the contrary, boron atoms are several times more often bonded only to N or also only to C - in other words, they inhibit formation of pure C and especially pure N zones. This can inhibit formation of N_2 molecules and therefore increasing the thermal stability of the material as shown in figure 8.8(b).

sample		Si-N bonds	surroundings of Si	coord. (N)	coord. (total)	lonepairs/ N at. (%)	like bonds (%)
Si-C-N	- low Si/C	26	1N, 9CN	2.42	2.88	81	34
Si-B-C-N	- low Si/C	31	3N, 6CN	2.69	3.04	60	19
Si-C-N	- high Si/C	109	17N, 9CN	2.70	3.11	78	7
Si-B-C-N	- high Si/C	118	25N, 3CN	2.89	3.22	65	3

Table 8.9: *Selected structural data for Si-C-N and Si-B-C-N samples of composition $Si_{11}C_{53}N_{36}$ and $Si_{11}B_{14}C_{39}N_{36}$ (denoted as low Si/C) and $Si_{32}C_{14}N_{54}$ and $Si_{32}B_8C_6N_{54}$ (high Si/C). The columns show (1) number of Si-N bonds (all bond orders), (2) how many Si atoms are bonded only to N, and how many of them are bonded only to C and N atoms, (3) averaged nitrogen coordination number, (4) averaged total coordination number, (5) the percentage of N atoms with which a lonepair is associated, and (6) percentage of like bonds in a network.*

Table 8.9 shows structural differences resulting from replacing a proportion of the C atoms by B in Si-C-N samples whilst keeping constant the atomic density, cooling rate and using the same set of bonding distance cutoffs to identify bonds. As has been shown previously (in chapters 3 and 4 experimentally, in table 8.2 by simulations), the (newly added) boron forms a high number of bonds with nitrogen. However, the occupation of a fraction of the nitrogen bonding states by boron does not generally lead to a decrease of the

numbers of other N-containing bonds. Si-N, the most populated bond, is increased (see column 1 of table 8.9) due to a decrease in the number of Si-C bonds, resulting from the fact that a proportion of C was replaced by B which has very low affinity to Si. The result is a higher number of Si atoms bonded only to N (at practically constant Si coordination) - see column 2. The most important result in table 8.9 is an increase in average N coordination number due to the new B-N bonds (see column 3) and the consequent increase in total coordination number (at approximately constant coordinations of Si and C) - see column 4. This is possible because a proportion of the lonepairs associated with N atoms (see the networks in Fig. 8.1) are converted to bonding electrons (column 5) when B is added. Column 6 shows a decrease in the percentage of like (mainly C-C) bonds in the networks when some of the C atoms are replaced by B

The demonstrated ability of boron to convert nitrogen lonepairs present in Si-C-N networks to bonding electrons has two important consequences:

(1) a higher coordination number for the B-containing networks, leading to a higher bulk modulus and hardness (this prediction agrees well with experiment in that the Si-B-C-N materials[5,11] have significantly higher hardness than do the Si-C-N materials prepared under equivalent conditions[12,13]).

(2) the higher coordination number is also likely to improve the thermal stability of the Si-B-C-N materials in comparison with Si-C-N materials because more bonds need to be broken before an atom can diffuse from one site to another. .

8.3.4 Conclusions

Temperature stability was examined for Si-(B)-C-N materials of various Si/C ratios. It was shown that lifetimes of all major bonds are significantly longer in Si-B-C-N materials with higher Si/C ratios, despite the fact that at a given composition lifetimes of C-containing bonds are similar or even longer than lifetimes of Si-containing bonds. Calculations capturing the formation of N_2 molecules in materials show that both the addition of 14% of B into a Si-C-N material and increasing of the Si/C ratio in Si-(B)-C-N materials leads to inhibiting of N_2 formation. All of these results correlate with experimental observations showing exceptional thermal stability of high-Si/C Si-B-C-N materials. Higher network coordination number at higher B content (as well as at higher Si/C ratio) appears to be a reason for the impressive thermal stability. The differences in calculated results are significant, suggesting that ab-initio liquid quench simulations are suitable for reliable predictions of relative thermal stabilities of amorphous materials.

8.4 Optical properties and band gap

In this section, calculations of optical conductivities and band gaps are shown for samples of compositions:

- $Si_{14}B_{23}C_6N_{55}$ (effect of number of unoccupied states considered).
- $Si_{11}B_{14}C_{39}N_{36}$ and $Si_{32}B_8C_6N_{54}$ (optical properties).
- $Si_{10}B_{12}C_{40}N_{38}$, $Si_{10}B_{12}C_{40}N_{38}H_6$ and $Si_{32}B_8C_6N_{54}$ (band gaps). Here, the high-Si composition is the same as used for calculations of optical properties; the low-Si composition is slightly different because it resulted from averaging over samples deposited with various values of substrate bias

The composition with non-negligible H content refers to a sample deposited with U_b = -100 V, the other compositions refer to samples prepared with U_b = -500 V where the experimental H content was significantly reduced.

8.4.1 Related experimental results

Ref. 14 shows measured values of the extinction coefficient and the refractive index for various Si-C-B-N compositions in the range λ = 300 - 1700 nm. Films with high Si content exhibited low values of the extinction coefficient (significantly decreasing with λ) and refractive index 1.8 - 2.1 (decreasing with λ). Films with high C content exhibited high values of the extinction coefficient (slowly decreasing with λ) and refractive index 1.9 - 2.2 (increasing with λ). The observed dependence of the extinction coefficient (and thus the photoconductivity) on the Si/C ratio in the films indicates that the band gap in the Si-B-C-N materials studied increases significantly with increasing Si/C ratio. This is also indicated by the measurements of electrical conductivity of Si-B-C-N materials (see the discussion in chapter 4). In summary experimental work has shown that:

- Si-C-B-N materials are insulators at high Si/C ratio while they have conductivity of the same order as semiconductors at low Si/C ratio.
- For samples with low content of implanted Ar, the electrical conductivity increases with increasing value of the negative substrate bias $|U_b|$, which is probably related to decreasing hydrogen content with increasing $|U_b|$.

These results are consistent with an increase of the band gap with increasing Si/C ratio and with increasing H content in materials.

8.4.2 Related theory - the Kubo-Greenwood formula

The relations between (real part of) the photoconductivity σ, the absorption coefficient α, the extinction coefficient k, the refractive index n, the wavelength λ, the angular frequency ω, the speed of light c and the permittivity ε_0 are:

- $\alpha = \sigma/\varepsilon_0 nc$

(often used is for some reason also $\alpha = 4\pi\sigma/nc$ which is in Gaussian - not SI - system of units)

- $k = \alpha\lambda/4\pi = \sigma\lambda/4\pi\varepsilon_0 nc = \sigma/2\varepsilon_0 n\omega$

Once we know the electronic structure of a material, the real part of the conductivity can be calculated for given ω using the Kubo-Greenwood formula[15,16]:

$$\sigma(\omega) = \frac{2\pi e^2}{3m^2\omega\Omega}\sum_{n,m}\sum_{\alpha=x,y,z}(f_m - f_n)\left|<\psi_m|p_\alpha|\psi_n>\right|^2\delta(E_n - E_m - \hbar\omega) \qquad \text{(Eq. 8.3)}$$

where ψ, E and f are eigenfunctions, their eigenvalues and the occupation numbers, respectively, and Ω is the volume of the supercell. It is well known in density-functional theory that the calculated Kohn-Sham eigenvalues and related transition energies do not represent the true electronic transitions. In particular, the Kohn-Sham gaps tend to be too small. Despite this limitation, this formalism has been reported to give correct trends or even a semiquantitative agreement with an experiment.

The electronic structure of an amorphous semiconductor also allows us to calculate the optical gap ("Tauc gap") E_{opt} of such material from the formula

$$\hbar\omega\sqrt{\varepsilon} = B(\hbar\omega - E_{opt}) \qquad \text{(Eq. 8.4)}$$

where B is a constant. The dielectric permittivity ε can be calculated from the convolution integral

$$\varepsilon = \frac{1}{\omega^2}\int g_0(E)g_u(E+\hbar\omega)dE \qquad \text{(Eq. 8.5)}$$

where g_0 and g_u are densities of occupied and unoccupied states below and above the Fermi energy, respectively.

8.4.3 Interpretation of calculated photoconductivity

Figure 8.9 shows the effect of the number of unoccupied states included in the calculation on the calculated photoconductivity of the simulated sample $Si_{14}B_{23}C_6N_{55}$. In addition to 212 occupied two-electron Kohn-Sham states, which resulted from the paired-spin approach used in the simulation, another 10-100 unoccupied states were used for the calculation. It can be seen that to obtain a value of the calculated photoconductivity which is independent of the number of unoccupied states considered, the number of unoccupied states needed increases with increasing photon energy. Although the exact (unoccupied states needed)/(occupied states) ratio may differ for various compositions, results shown Figs. 8.10-8.12 were obtained with 100 unoccupied states in addition to 211 - 223 occupied states, which is more than enough for completely reliable results in the range where the optical properties were investigated experimentally (λ ≥ 300 nm - that is, energy ≤ 4 eV).

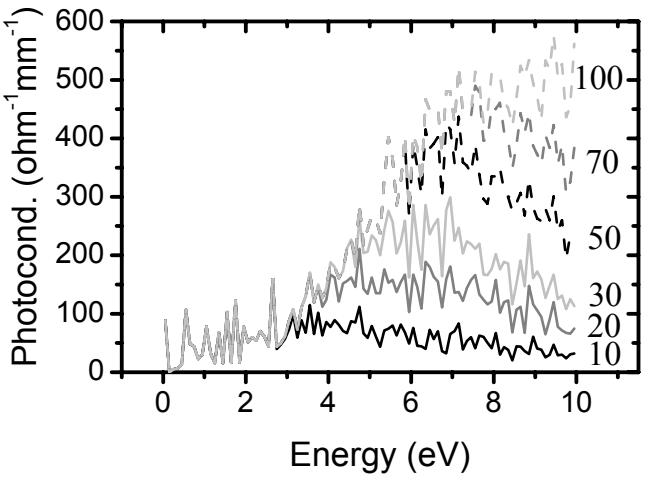

Fig. 8.9: *Calculated photoconductivity of the material of composition $Si_{14}B_{23}C_6N_{55}$. Numbers 10 - 100 indicate numbers of empty Kohn-Sham states included in the calculation performed using a 98-atom cell.*

Figure 8.10(a) shows a typical dependence of the photoconductivity σ on λ. What can be seen is the characteristic decrease of σ to zero (i.e. increasing material transparency) with λ increasing up to ~1000 nm, due to decreasing photon energy to values lower that the band gap. The considerable noise below 1000 nm is caused by the limited number of atoms (~100) in the simulation cell, while for example there are $\sim 10^{17}/mm^2$ atoms in deposited samples used for experimental measurements of σ. For the same reason, there are calculated zero values of σ interrupted by several non-zero responses (instead of a smooth close-to-zero dependence) at high values of λ where the material is transparent.

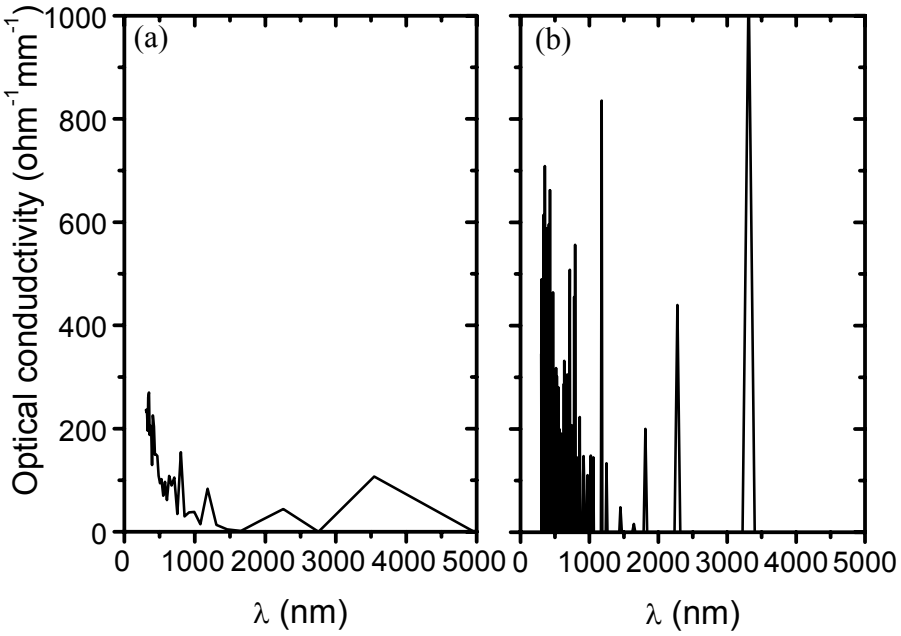

Fig. 8.10: *Calculated photoconductivity of material of composition $Si_{11}B_{14}C_{39}N_{36}$. Panel (a) shows results calculated with energy (i.e. frequency) steps of 0.1 eV. Panel (b) shows results calculated with energy steps of 0.01 eV.*

Figure 8.10(b) shows the effect of the steps used for sampling the energy (i.e. frequency) on the results. Below the limit where σ has non-zero values only, the 10 times more frequent sampling caused much higher deviation of calculated σ values but did not affect averaged values or trendlines. Averaged calculated value of σ between 2 - 4 eV (300 - 600 nm) is in this case 173.7 $\Omega^{-1}mm^{-1}$ for energy steps of 0.1 eV and 174.9 $\Omega^{-1}mm^{-1}$ for energy steps of 0.01 eV which constitutes a difference of less than 1 %. However, in the range where σ has mostly zero values, the intensity of the few responses observed is proportional to 1/(energy step). It can be concluded that while numbers and amplitudes of these freestanding responses can be probably used for qualitative comparing of various samples and their levels of transparency, their amplitudes cannot be compared with those in the range where σ has non-zero values only.

8.4.4 Calculated photoconductivity

Figures 8.11 and 8.12 compare calculated and experimental (measured between λ = 300 and 1700 nm) photoconductivity of two Si-B-C-N samples of composition $Si_{11}B_{14}C_{39}N_{36}$ (semiconductor, opaque in visible spectra) and $Si_{32}B_8C_6N_{54}$ (insulator, transparent - slightly yellow - in visible spectra). Because of the noise, exponential-decay trendlines are provided together with the calculated values.

Due to the smaller Kohn-Sham gaps, underestimated for fundamental reasons by the DFT, photons are more likely to be absorbed in the electronic transitions, which increases the calculated photoconductivity. This phenomenon is more significant for materials with large band gaps, while it is less important for materials with small or even zero band gaps. In accordance with this expectation, the calculated σ values for the semiconductive material $Si_{11}B_{14}C_{39}N_{36}$ were in the same order as the experimental ones (on the average 2.75 times higher in the range shown), while the calculated σ values for the insulating material $Si_{32}B_8C_6N_{54}$ were almost two orders of magnitude higher than the experimental ones (on the average 80 times higher in the range shown). Presented calculated data are divided by these factors in order to allow comparing of shapes of the dependencies.

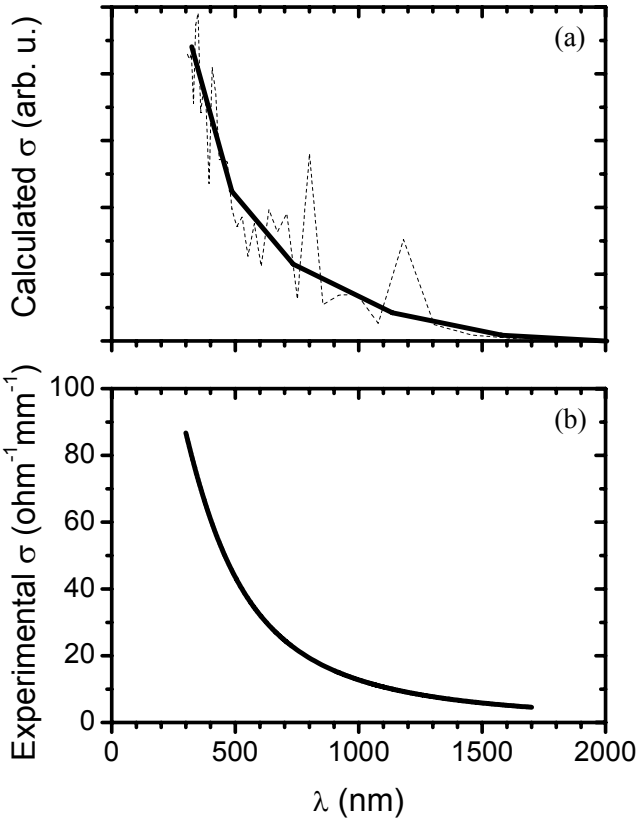

Fig. 8.11: *Photoconductivity of material of composition $Si_{11}B_{14}C_{39}N_{36}$. Panel (a) shows calculated values divided by a factor of 2.75 and a exponential-decay trendline. Panel (b) shows experimental values measured between λ = 300 and 1700 nm.*

A phenomenon complementary to the previous one can be seen from comparison of shapes of the dependencies σ(λ). For the material $Si_{11}B_{14}C_{39}N_{36}$ where both the experimental and DFT band gaps are narrow and thus close to each other (Fig. 8.11), the shapes of the experimental and calculated dependencies of σ(λ) are very similar. In particular, both of them indicate that σ(λ) starts to increase significantly with decreasing λ for λ < ~1100 nm. This is in accordance with opacity of this material in visible spectra (λ < 800 nm).

On the other hand, the calculated and experimental dependencies differ for the material $Si_{32}B_8C_6N_{54}$ where the experimental band gap is much larger than the DFT band gap. In particular, the calculated dependence σ(λ) starts to increase with decreasing λ sooner (at λ < 700 - 800 nm: Fig. 8.12(a)) than the experimental dependence (λ < 500 nm: Fig. 8.12(b)). This is again due to the easier electronic transitions activated by phonons with λ = 500 - 800 nm over the narrow DFT band gap, while in the experiment such transitions are possible below 500 nm only. Absorption of blue light (λ < 500 nm) in the material and its transparency in the other parts of the visible spectrum (i.e. green and red) result in the yellow (corresponding to green + red) colour observed.

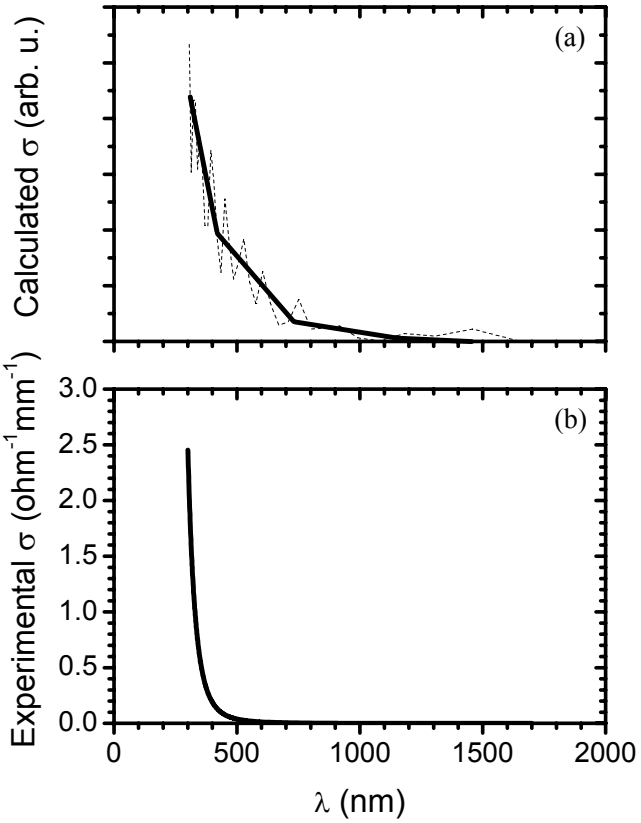

Fig. 8.12: *Photoconductivity of material of composition $Si_{32}B_8C_6N_{54}$. Panel (a) shows calculated values divided by a factor of 80 and a exponential-decay trendline. Panel (b) shows experimental values measured between λ = 300 and 1700 nm.*

8.4.5 Calculated electronic density of states

Figure 8.13 shows calculated electronic density of states (EDOS) for Si-B-C-N materials with low Si/C ratio with ($Si_{10}B_{12}C_{40}N_{38}H_6$) and without ($Si_{10}B_{12}C_{40}N_{38}$) hydrogen, and with high Si/C ratio ($S_{i32}B_8C_6N_{54}$). Figure 8.13(a) shows complete band structures of the materials, while Fig. 8.13(b) shows only EDOS around averaged the Fermi energies calculated. Around the Fermi energy it can be seen that the EDOS is slightly lower for the hydrogenated low-Si sample than for the non-hydrogenated one, and especially that the EDOS is much lower for the high-Si sample than for the low-Si ones. We quantify the results by calculating of two quantities, which can be used as a measure of the band gap:

- the Tauc gap introduced above.
- the "10-states interval": averaged width of the energy interval, which includes 5 highest occupied and 5 lowest unoccupied states. These intervals are comparable due to the similar numbers of occupied states in the simulation cells for all samples shown.

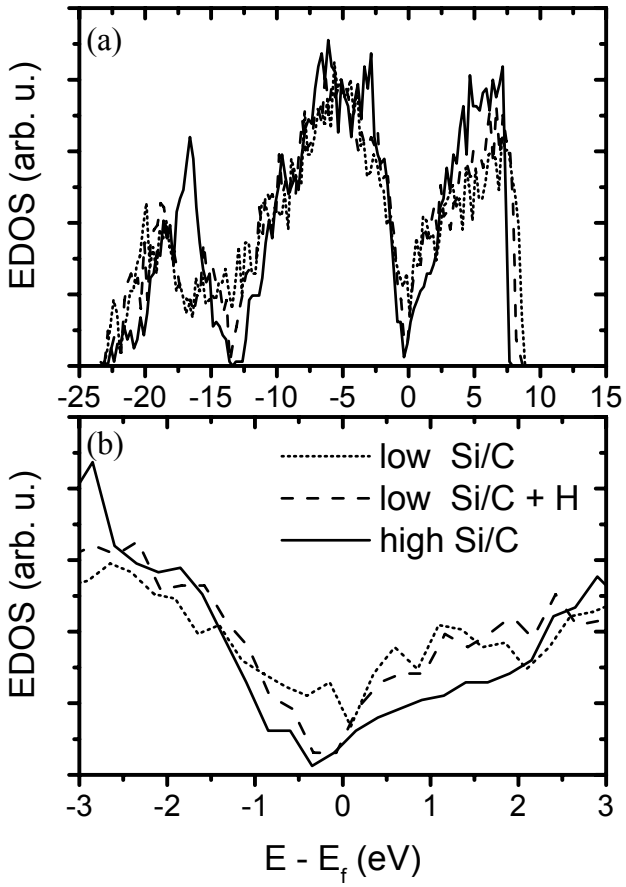

Fig. 8.13: *The electronic density of states (EDOS) for Si-B-C-N materials with low Si/C ratio with ($Si_{10}B_{12}C_{40}N_{38}H_6$ - low $|U_b|$) and without ($Si_{10}B_{12}C_{40}N_{38}$ - high $|U_b|$) hydrogen, and with high Si/C ratio ($S_{i32}B_8C_6N_{54}$). Results are averaged over 13 snapshots obtained during the 500 fs production run. Panel (a) includes all occupied and part of the unoccupied states. Panel (b) shows EDOS around averaged Fermi energy only.*

sample	Tauc gap (eV)	10-states interval (eV)
low Si/C	-1.0	1.55
low Si/C + H	-0.5	1.85
high Si/C	+0.8	2.35

Table 8.9: *Tauc gap and averaged width of the energy interval, which includes 5 highest occupied and 5 lowest unoccupied states (the 10-states interval) for low Si/C ratio Si-B-C-N materials with ($Si_{10}B_{12}C_{40}N_{38}H_6$) and without ($Si_{10}B_{12}C_{40}N_{38}$) hydrogen, and with high Si/C ratio ($S_{i32}B_8C_6N_{54}$).*

The main reason for introducing the second quantity is the relatively large error associated with calculated Tauc gaps. These errors can be up to 100% in cases when the line fitted to the linear part of the Equation 8.4 plot crosses the vertical axis very close to zero.

The results are summarized in table 8.9. It can be seen that:

- as expected for the reasons discussed above, the Tauc gaps are underestimated by the DFT simulations, having small or even negative values. They can therefore only be used for comparative purposes.
- despite the relatively large error bars of the Tauc gaps, both quantities calculated give the same trends.
- the trends given are in agreement with the expectations (increase of the band gap with increasing Si/C ratio, and also slight increase of the band gap after addition of H into the material). These results can be therefore regarded as complementary to the calculations of photoconductivity.

8.4.6 Conclusions

It has been confirmed that the calculations of EDOS and related quantities give the correct trends when comparing materials of different compositions and thus are able to give reliable predictions concerning the influence of individual elements on optical and electrical characteristics of amorphous materials. The predictions are semiquantitatively correct (including correct determination of the λ limit between absorbed and transmitted wavelengths) for narrow band gap materials only. Underestimation of the band gap can affect the quantitative results significantly for large band gap materials.

8.5 References

[1] M. L. Cohen, Phys. Rev. B **32**, 7988 (1985).

[2] www.webelements.com

[3] P. Fitzhenry, M.M.M. Bilek, N.A. Marks, N.C. Cooper and D.R. McKenzie, J.Phys.: Condens. Matter. **15**, 165 (2003).

[4] J. Vlček, K. Rusňák, V. Hájek and L. Martinů, J. Appl. Phys. **86**, 3646 (1999).

[5] J. Vlček, S. Potocký, J. Čížek, J. Houška, M. Kormunda, P. Zeman, V. Peřina, J. Zemek, Y. Setsuhara and S. Konuma, J. Vac. Sci. Technol. A **23**, 1513 (2005).

[6] Y. Panayiotatos, S. Logothetidis, M. Handrea and W. Kautek, Diamond Relat. Mater. **12**, 1151 (2003).

[7] J. Musil, Surf. Coat. Technol. **125**, 322 (2000).

[8] V. Hájek, K. Rusňák, J. Vlček, L. Martinů and S.C. Gujrathi, J. Vac. Sci. Technol. A **19**, 899 (1999).

[9] J. Houška, J. Vlček, S. Hřeben, M.M.M. Bilek and D.R. McKenzie, Appl. Phys. Lett. **76**, 512 (2006).

[10] A. Müller, P. Gerstel, M. Weinman, J. Bill and F. Aldinger, J. Eur. Ceram. Soc. **20**, 2655 (2000).

[11] J. Houška, J. Vlček, Š. Potocký and V. Peřina, accepted for publication in Diamond Relat. Mater. (2006).

[12] J. Vlček, M. Kormunda, J. Čížek, V. Peřina, J. Zemek, Surf. Coat. Technol. **160**, 74 (2002).

[13] J. Vlček, M. Kormunda, J. Čížek, V. Peřina, J. Zemek, Diamond Relat. Mater. **12**, 1287 (2003).

[14] J. Čížek, J. Vlček, L. Martinů, A. Amassian, Š. Potocký, J. Houška and Z. Soukup, prepared for publication in Thin Solid Films

[15] R. Kubo, J. Phys. Soc. Jpn. **12**, 570 (1957).

[16] D.A. Greenwood, Proc. Phys. Soc. Lond. **71**, 585 (1958).

9 Conclusions

The thesis reports on results obtained in years 2002-2006 in the laboratories of the Department of Physics at the University of West Bohemia (Czech Republic) and of the Department of Applied and Plasma Physics at the School of Physics, University of Sydney (Australia). The results presented in chapters 3-8 fulfil the thesis aims as documented in chapter 1.

New hard and highly thermally stable amorphous Si-B-C-N materials have been synthesized and computer simulations of their structures performed. The materials have been shown to have a unique combination of properties making them ideal candidates for applications in areas such as protective coating technologies, microelectronics or the production of thermally stable fibers for composites. The effects of plasma parameters during the film formation process have been investigated and optimized with respect to film properties such as hardness and thermal stability. Atomistic simulations have been used to explain the dependencies observed.

9.1 Main experimental conclusions

The first part of the thesis deals with the experimental preparation and characterization of the new quaternary Si-B-C-N materials, deposited in the form of thin films by reactive magnetron sputtering. The main conclusions of this part of the research can be summarized as follows.

(1) A series of novel quaternary Si-B-C-N materials in the form of thin films were prepared by reactive magnetron sputtering of composite C-Si-B or B_4C-Si targets in N_2–Ar gas mixtures. The technique used proved to be suitable for reproducible synthesis of these materials. A number of B-C-N and Si-B-C films were also prepared for comparison. The Si-B-C-N films were generally found to be amorphous with low compressive stress and good adhesion to silicon or glass substrates. The process and film characteristics were controlled by varying the sputter target composition (0-75 % Si in a target erosion area at a fixed 20 % B fraction in the C-Si-B target erosion area). The Ar fraction of the N_2–Ar gas mixture was varied between 0 and 100 %. The effect of negative rf-induced substrate bias, U_b, was investigated in the range between floating potential and -700 V, and the effects of substrate temperatures up to 350 °C (occasionally up to 700 °C) were studied.

(2) Deposition carried out using a target with a high Si fraction (60-75 %) in the sputtered target erosion area, leading to high Si/C ratios in the films, were found to be optimum for producing dense covalently bonded insulating materials with high hardness (up to 47 GPa), high elastic recovery (up to 88 %) and low compressive stress. It was shown that silicon relieves compressive stress generated by implanted Ar atoms in these materials. On the other hand, films created with a high C fraction (75 %) in the sputtered target erosion area, which have low Si/C ratios, were found to be semiconductive materials with conductivity controllable over a wide range.

(3) The discharge gas mixture composition was found to be an important process parameter for the deposition of Si-B-C-N materials due to the (a) different sputtering yields of target materials by argon and nitrogen, which affect the elemental composition and deposition rate, (b) stronger bombardment of growing films at higher Ar content in N_2-Ar gas mixture as shown by measurements of powers absorbed in the

discharge, affects the hardness and deposition rate of the materials, and (c) processes implicated by implanted argon atoms. In particular, high Ar content in N_2-Ar gas mixture was found to increase the hardness of the high-Si/C materials, and to increase compressive stress and decrease electrical conductivity (especially at high $|U_b|$) of the low-Si/C materials

(4) Negative substrate bias voltage, U_b, has been shown to be useful in controlling the characteristics of films of very similar Si-B-C-N compositions. In particular, the low $|U_b|$ value, U_b = -100 V, with the corresponding low values of the ion-to-film-forming particles flux ratio $\Gamma_i/\Gamma_p \leq 0.2$ and low ion energy per deposited atom $E_{ia} \leq 20$ eV are optimum for the formation of high-Si/C films with maximum hardness and elastic recovery when a gas mixture with high Ar content is used. On the contrary, increasing $|U_b|$ values were observed to improve the electrical conductivity of the low-Si/C films with low content of implanted Ar.

(5) Furthermore it was shown that increasing substrate temperature improves the mechanical properties of the high-Si/C materials, while at decreasing Si/C ratio this effect becomes weaker or even inverse.

9.2 Main simulation conclusions

The second part of the thesis presents the results of ab-initio computer simulations of structures approximating the experimentally prepared (Si)-(B)-C-N materials. The simulations were performed using a liquid quench algorithm implemented in Car-Parrinello molecular dynamics. The main conclusions of this research can be summarized as follows.

(1) The formation of free N_2 molecules was observed in the liquid quench simulations of (Si)-(B)-C-N amorphous materials and a temperature window (with a peak at 5000 K) in which stable N_2 molecules are formed was identified. The results predict that the final content of nitrogen incorporated in networks of given Si/B/C ratios increases with the cooling rate (due to the shorter time spent in the active temperature window for N_2 formation) and increases with the density of the material (due to higher coordination numbers inhibiting N diffusion and subsequent formation of N_2). The results further suggest that at constant temperature and atomic density the rate of N_2-formation in Si/B/C-containing materials decreases with increasing Si-content. This explains the ability of Si to enhance the final N-content in experimentally prepared materials. A modified liquid-quench algorithm, which begins with a sufficient N-excess and progressively removes N_2 molecules as they form in the simulation cell, has been developed to simulate the diffusion of N_2 from the structure during film synthesis.

(2) When implanted Ar atoms were included in the simulations of Si-B-C-N materials, we observed a segregation of a Si-rich phase around them. The energy advantage gained by surrounding Ar atoms with longer and more flexible Si-containing bonds was proposed to be a driving force for this segregation. The process was shown to be temperature-dependent with a maximal effectiveness at 1000-1500 K. Although it was found that the samples with higher Ar content (corresponding to films deposited with high $|U_b|$) are not far from homogenous (most of the network atoms were close to at least one Ar atom), the samples with low Ar levels (corresponding to films deposited with low $|U_b|$) were predicted to be heterogeneous. The heterogeneous low Ar materials had Si-rich regions close to the Ar atoms and Si-poor regions elsewhere.

This predicted segregation correlates with and can be used to explain several experimentally observed phenomena, including (a) hardening of annealed materials due to the identical temperature dependence of both the hardening and the segregation processes, (b) increased material hardness at U_b = -100 V compared with U_b = -500 V for films prepared with high (75%) Ar fraction in N_2-Ar gas mixture, (c) an increasingly positive effect of substrate temperature on hardness with increasing content of (segregating) Si in the films, and (d) the ability of Si to relieve stress generated by the implanted Ar atoms.

(3) In accordance with experimental (XPS and IR) results, the most highly populated bonds in the simulated Si-B-C-N materials with high-Si/C ratio were found to be Si-N (mostly single), B-N (single and double) and C-N (all bond orders). In the compositions with low-Si/C, the following bond types were also significant: C-Si (single), C-B (single) and C-C (single and double). A method to calculate bond ionicities, λ, using Wannier function centres (WFCs) was developed. Typical values calculated are 0.1-0.3 for homonuclear bonds, 0.4-1.0 for heteronuclear single bonds and 1.0-2.0 for heteronuclear double bonds. Calculated bond ionicities and atomic charges were shown to be in accordance with known electronegativities of atoms.

(4) An investigation of the effects of B and the Si/C ratio on the characteristics of Si-(B)-C-N materials was carried out. The inclusion of B, which bonds preferentially to N, results in the conversion of lonepairs of valence electrons associated with N atoms to bonding electrons, significantly increasing the averaged nitrogen coordination number. Carbon was found to form a significant number of multiple bonds whereas silicon tended to form single bonds. This resulted in higher network coordination numbers in networks with high Si/C ratio (despite same number of valence electrons of Si and C). Thus high Si/C ratio and non-zero B content (even when B replaces C which has more valence electrons) both lead to improved mechanical properties as well as thermal stability of the coatings, in agreement with experimental results.

(5) High-temperature stability of simulated materials was examined also by two direct methods. It was shown that lifetimes of all major bonds are significantly longer in higher-Si/C Si-B-C-N composition, despite the fact that at a given composition lifetimes of C-containing bonds are similar or even longer than lifetimes of Si-containing bonds. Calculations capturing formation of N_2 molecules in a material (indicating its decomposition) have shown that both the addition of B into a Si-C-N material and increasing of the Si/C ratio in Si-(B)-C-N materials lead to inhibiting of N_2 formation.

9.3 Applicability of the simulation method used

Experience obtained during liquid-quench MD simulations of amorphous materials and comparison of the results with experiment is summarised below for individual material characteristics. Both the successes and failures of the method used are included.

Material structure and roles of atoms

- The method used has been shown to be very successful in describing structures of materials and the processes taking place there, providing information not accessible experimentally. The phenomena examined include segregation into zones of different compositions, the formation of free molecules, bonding preferences of individual atom

types or preferences of valence electrons to form bonds or lonepairs. It has been shown that for obtaining exact results in this field, all the atoms present (including e.g. apparently negligible few percent of implanted inert argon) usually have to be included in the simulation.

- In contrast to monoatomic materials, such as a-C with structures. previously characterized by a few quantities (coordination numbers, numbers of network rings), the statistical information available here can provide a variety of interesting but complex results including bonding statistics, distributions of distances between atoms of various types, numbers of lonepairs associated with individual atom types or surroundings of (sets of atoms bonded to) individual atom types. Further information can be provided by visual inspection of the structures.
- On the other hand, the simulation algorithm used cannot capture processes that take place at long (≥ 10ps) time scales (such as crystallization or diffusion of free gas molecules formed to the surface).

Bonding statistics and bond characteristics

- The calculated bonding statistics correlate very well with the experimental results, including in cases when they are very far from a "random network" (see for example the very low or zero number of Si-Si bonds even at a high Si content).
- Bond length and bond ionicities as indicated by Wannier function centers (WFCs) correlate with predictions given by reported covalent radii and electronegativities of individual atom types for the pseudopotentials and energy cutoff used. The method presented for the calculation of a covalent bond iconicity however needs to be tested also for some more ionic amorphous materials.
- Occasional problems in the quantification of the bonding were encountered due to the difficulty associated with selecting bond distance cutoffs when the first and second peak of an atom-WFC partial distribution function are not well distinguished (most likely for Si). Moreover, finding of a bond order may be difficult when all WFCs are close to a particular atom and some of them could therefore be a lonepair (most likely for the short and relatively ionic C≡N bond).

Stress and mechanical properties

- It has been already shown previously that correct values of stress can be calculated by the simulation method used. However, our results suggest that a very exact knowledge not only of elemental composition, but also of materials density is necessary for this to be achieved. Sufficiently accurate material densities are often not available for disordered amorphous materials, which makes the direct stress calculations probably more useful for crystalline materials. A similar statement can be made for bulk modulus (for which roughly correct data were nevertheless successfully obtained, but without any additional information not accessible experimentally).
- The high credibility of calculated structural and bonding data makes them very useful for many qualitative predictions based on characteristics which are known to affect mechanical properties (coordination numbers, bond lengths or bond ionicities).

Electronic structure and photoconductivity

- It is well known that due to the smaller Kohn-Sham gaps, underestimated for fundamental reasons by DFT, photons are more likely to be absorbed in the electronic transitions, which increases the calculated photoconductivity. Typically the calculated characteristics related to the material electronic structure (photoconductivity, Tauc gap

or the interval containing 5 highest occupied and 5 lowest unoccupied states) are therefore in mutual agreement, but they do not agree with experimental values.

- The results suggest that this phenomenon is more significant for materials with a large band gap, while it is less important for materials with a small or even zero band gap. For the latter narrow band gap materials, the predictions can be semiquantitatively correct (including, for example, the correct determination of the λ limit between absorbed and transmitted wavelengths when calculating the photoconductivity).
- Nevertheless, the method has been shown to give the correct trends, which allows reliable predictions to be made on the qualitative behaviour of the band gap and related characteristics.

Temperature-dependent characteristics

- The method used has been shown to be very successful for finding of temperature dependence of various phenomena. Characteristics successfully directly examined at various temperatures include segregation in the materials around implanted Ar atoms and the evolution of N_2 molecules.
- Observation of lifetimes of bonds (which, contrary to simulated crystalline materials, break and form again at sufficiently short time scales even at low temperatures) was shown to be suitable for examining the temperature stability of materials or of N_2 molecules formed in them. Due to the large differences in quantities of interest, the results obtained can be relatively easily and reliably interpreted.

Publications of the candidate

Refereed Journal Papers

[I] **J. Houska**, J. Vlcek, S. Potocky and V. Perina, "Influence of substrate bias voltage on structure and properties of hard Si-B-C-N films prepared by reactive magnetron sputtering", accepted for publication in Diamond Relat. Mater. (2006).

[II] **J. Houska**, J. Vlcek, S. Hreben, M.M.M. Bilek and D.R. McKenzie, "Effect of B and the Si/C ratio on high-temperature stability of Si-B-C-N materials", Europhys. Lett. **76**, 512 (2006).

[III] J. Vlcek, S. Potocky, **J. Houska**, P. Zeman, V. Perina and Y. Setsuhara, "New quaternary Si-B-C-N films prepared by reactive magnetron sputtering", Trans. Mater. Res. Soc. Jpn **31**, 447 (2006).

[IV] **J. Houska**, O. Warschkow, M.M.M. Bilek, D.R. McKenzie, J. Vlcek and S. Potocky, "The effect of argon on the structure of amorphous SiBCN materials: an experimental and ab initio study", J. Phys.: Condens. Matter **18**, 2337 (2006).

[V] J. Vlcek, S. Potocky, J. Cizek, **J. Houska**, M. Kormunda, P. Zeman, V. Perina, J. Zemek, Y. Setsuhara and S. Konuma, "Reactive magnetron sputtering of hard Si-B-C-N films with a high-temperature oxidation resistance", J. Vac. Sci. Technol. A **23**, 1513 (2005).

[VI] M.J. Jung, Y.M. Chung, **J. Houska**, P. Baroch, J. Vlcek, J. Musil, K.H. Nam and J.G. Han, "A study on the energy distribution for grid-assisting magnetron sputtering", Surf. Coat. Technol. **200**, 421 (2005).

[VII] **J. Houska**, M.M.M. Bilek, O. Warschkow, D.R. McKenzie and J. Vlcek, "Ab initio simulations of nitrogen evolution in quenched CN_x and SiBCN amorphous materials", Phys. Rev. B **72**, Art. No. 054204 (2005).

Conference Papers and Proceedings (personal participation)

[VIII] **J. Houska**, J. Vlcek, J. Kalas, S. Hreben, M.M.M. Bilek and D.R. McKenzie, "New Si-B-C-N coatings: Ab-initio calculations and experimental verification", Presented at 10th International Conference on Plasma Surface Engineering, September 10-15, 2006, Garmisch-Partenkirchen (Germany).

[IX] **J. Houska**, J. Vlcek, J. Kalas, S. Hreben, M.M.M. Bilek and D.R. McKenzie, "New Si-B-C-N coatings: Ab-initio calculations and experimental verification", Presented at 22nd Symposium on Plasma Physics and Technology, June 26-29, 2006, Prague (Czech Republic).

[X] **J. Houska**, M.M.M. Bilek, O. Warschkow, D.R. McKenzie, J. Vlcek and S. Potocky, "New amorphous Si-B-C-N materials: An ab-initio study", Presented at The International Conference on Metallurgical Coatings and Thin Films, May 1-5, 2006, San Diego (USA).

[XI] **J. Houska**, J. Vlcek, S. Potocky, J. Cizek, Z. Soukup and V. Perina, "Influence of substrate bias voltage on the mechanical properties of Si-B-C-N films prepared by reactive magnetron sputtering", Proceedings of the Juniormat'03, September 22-24, 2003, Brno (Czech Republic), pp. 20-24.

Conference Papers and Proceedings (work-fellow participation)

[XII] D.R. McKenzie, O. Warschkow, M.M.M. Bilek, N.A. Marks, H.F. Wilson, **J. Houska** and D.G. McCulloch, "Advanced modelling for the design of new materials and devices", Plenary lecture, 10th International Conference on Plasma Surface Engineering, September 10-15, 2006, Garmisch-Partenkirchen (Germany).

[XIII] J. Kalas, J. Vlcek, S. Potocky, S. Hreben, **J. Houska**, K. Rusnak, P. Zeman and V. Perina, "Temperature behaviour of Si-B-C-N coatings up to 1300 °C substrate limit", Presented at 10th International Conference on Plasma Surface Engineering, September 10-15, 2006, Garmisch-Partenkirchen (Germany).

[XIV] J. Vlcek, S. Potocky, **J. Houska**, P. Zeman, V. Perina and Y. Setsuhara, "New quaternary Si-B-C-N films prepared by reactive magnetron sputtering", Plenary lecture, 16th Symposium of the Materials Research Society of Japan, December 9-11, 2005, Tokyo (Japan).

[XV] J. Vlcek, S. Potocky, **J. Houska**, P. Zeman, Z. Soukup, V. Perina and L. Martinu, "Reactive magnetron sputtering of new quaternary Si-B-C-N films and their properties", Invited lecture, Fifth Sian-European International Conference on Plasma surface Engineering, September 12-16, 2005, Qingdao City, China.

[XVI] P. Kudlacek, J. Vlcek, **J. Houska**, J.G. Han, M.J. Jung and Y.M. Kim, "Diagnostics of grid-assisted magnetron sputtering using energy-resolved mass spectroscopy", Presented at the 17th International Symposium on Plasma Chemistry, August 7-12, 2005, Toronto (Canada).

[XVII] J. Vlcek, S. Potocky, J. Cizek, **J. Houska**, P. Zeman and Z. Soukup, "Reactive magnetron sputtering of hard Si-B-C-N films and their properties", Presented at The International Conference on Metallurgical Coatings and Thin Films, May 2-6, 2005, San Diego (USA).

[XVIII] P. Kudlacek, J. Vlcek, **J. Houska**, J.G. Han, M.J. Jung and Y.M. Kim, "Characterization of grid -assisted magnetron sputtering using energy-resolved mass spectroscopy", Presented at the 15th Symposium on Applications of Plasma Processes, January 15-20, 2005, Podbanské (Slovak Republic).

[XIX] M.J. Jung, **J. Houska**, P. Baroch, J. Vlček, J. Musil, K.H. Nam and J.G. Han, "A study on the energy distribution for grid-assisting magnetron sputtering", Presented at the 9th International Conference on Plasma Surface Engineering, September 13-17, 2004, Garmisch-Partenkirchen (Germany).

[XX] S. Potocky, J. Vlcek, **J. Houska**, J. Cizek, M. Kormunda and V. Perina, "Reactive magnetron sputtering of hard Si-B-C-N films with a controlled composition", Proceedings of the 21st Symposium on Plasma Physics and Technology, June 14-17, 2004, Praha (Czech Republic), p. 128.

[XXI] J. Vlcek, J. Cizek, S. Potocky, M. Kormunda, **J. Houska**, P. Zeman and Z. Soukup, "Reactive magnetron sputtering of hard Si-C-N and Si-B-C-N films and their properties", Invited lecture, American Vacuum Society 50th International Symposium and Exhibition, November 2-7, 2003, Baltimore (USA).

[XXII] S. Potocky, J. Cizek, J. Vlcek, M. Kormunda, **J. Houska**, V. Perina and J. Zemek, "Reactive magnetron sputtering of hard Si-B-C-N films with a controlled composition", Presented at the European Materials Research Society Spring Meeting, June 10-13, 2003, Strasbourg (France).

New quaternary amorphous materials Si-B-C-N: reactive magnetron sputtering and an ab-initio study

First part of the thesis is focused on experimental preparation of new hard quaternary amorphous materials Si-B-C-N with high thermal stability. Materials were prepared in the form of thin films using reactive magnetron sputtering. The technique used proved to be suitable for reproducible synthesis of these materials. The Si-B-C-N films were generally found to be amorphous with low compressive stress and good adhesion to silicon or glass substrates. The process and film characteristics were controlled by varying the sputter target composition, the Ar fraction in the N_2–Ar gas mixture, the negative rf-induced substrate bias, and the substrate temperature. Main conclusions describe the relationships between process parameters, discharge and deposition characteristics and film properties (elemental composition, chemical bonding structure, material hardness, compressive stress or electrical conductivity of materials prepared).

Second part of the thesis is focused on ab-initio simulations of structures of experimentally prepared Si-B-C-N materials. In the performed liquid-quench simulations, the Kohn-Sham equations for the valence electrons are expanded in a basis of plane wave functions, while core electrons were represented using Goedecker-type pseudopotentials. We simplified the ion bombardment process by assuming that the primary impact creates a localized molten region of high temperature and sufficiently short cooling time, commonly referred to as a thermal spike. Main conclusions deal with N_2 formation in studied materials, effect of implanted Ar on structure and properties of prepared materials, ability of Si to relieve that part of compressive stress which is caused by implanted Ar, and ability of B to improve thermal stability of Si-B-C-N materials. The calculated results are compared with experiment.

Nové kvaternární amorfní materiály Si-B-C-N: reaktivní magnetronové naprašování a ab-initio studie

První část disertace se zabývá experimentálním vytvářením nových tvrdých kvaternárních amorfních materiálů Si-B-C-N s vysokou teplotní stabilitou. Materiály byly připravovány ve formě tenkých vrstev pomocí reaktivního magnetronového naprašování. Použitá metoda se ukázala jako velmi vhodná pro reprodukovatelnou přípravu těchto materiálů. Vytvořené materiály Si-B-C-N byly obecně amorfní s nízkým kompresním pnutím a dobrou adhezí ke křemíkovým i skleněným substrátům. Depoziční proces a vlastnosti vytvořených materiálů byly řízeny složením rozprašovaného terče, složením výbojové směsi N_2-Ar, negativním rf předpětím na substrátech a teplotou substrátů. Hlavní závěry popisují vztahy mezi procesními parametry, charakteristikami depozičního procesu a vlastnostmi vytvořených materiálů (prvkové složení, vazebná struktura, kompresní pnutí a elektrická vodivost).

Druhá část disertace se zabývá ab-initio výpočty struktur experimentálně připravených materiálů Si-B-C-N, pomocí tzv. liquid-quench simulačního algoritmu. Kohn-Shamovy rovnice pro valenční elektrony byly řešeny s využitím rozložení vlnové funkce valenčních elektronů na rovinné vlny, zatímco jádra atomů a vnitřní elektronové orbitaly byly popsány pomocí Goedeckerových pseudopotenciálů. Iontový bombard byl zjednodušeně popsán na základě předpokladu, že dopad iontu vede k lokálnímu roztavení a následnému dostatečně rychlému zchlazení malého objemu materiálu – tzv. thermal spike. Hlavní závěry popisují vytváření molekul N_2 ve studovaných materiálech, vliv implantovaných atomů Ar na jejich strukturu a vlastnosti, schopnost Si snížit kompresní pnutí indukované atomy Ar, a schopnost B zvýšit teplotní stabilitu materiálů Si-B-C-N. Vypočítané výsledky jsou porovnávány s experimentálními.